Morphology and Dynamics of Solar Prominences

A THESIS

submitted for the award of Ph.D. degree of

MOHAN LAL SUKHADIA UNIVERSITY

in the

Faculty of Science

by

Anand D. Joshi

Under the Supervision of

Dr. Nandita Srivastava

Associate Professor

UDAIPUR SOLAR OBSERVATORY

PHYSICAL RESEARCH LABORATORY, UDAIPUR

Department of Physics

Faculty of Science

MOHAN LAL SUKHADIA UNIVERSITY

UDAIPUR

2011

DECLARATION

I hereby declare that the work incorporated in the present thesis entitled ***"Morphology and Dynamics of Solar Prominences"*** *is my own work and is original. This work, in part or in full, has not been submitted to any University for the award of a Degree or a Diploma.*

Date:

Anand D. Joshi
(Author)
Udaipur Solar Observatory
Physical Research Laboratory
P. B. No. 198, Badi Road
Udaipur - 313 001
Rajasthan, India

CERTIFICATE

I feel great pleasure in certifying that the thesis entitled ***"Morphology and Dynamics of Solar Prominences"*** *embodies a record of the results of investigation carried out by* ***Mr. Anand D. Joshi*** *under my guidance. I am satisfied with the analysis of data, interpretation of results and conclusions drawn.*

He has completed the residential requirement as per the rules.

I recommend the submission of this thesis.

Date:

Dr. Nandita Srivastava
(Thesis Supervisor)
Associate Professor
Udaipur Solar Observatory
Physical Research Laboratory
P. B. No. 198, Badi Road
Udaipur - 313 001
Rajasthan, India.

Countersigned by
Head of the Department

To my parents

Contents

List of Figures

List of Tables

Acknowledgments

I would like to start by expressing my gratitude towards my supervisor Dr. Nandita Srivastava. I have enjoyed working with her, and always found her open to discussions. She is somebody I can always argue without any hesitation, which I believe is very necessary for research. Apart from the science, I learned a lot about the ethics of science from her. I thank her for the patience and confidence that she showed in me. I also admire her ability to maintain composure, and not let her reasoning ability falter. I can proudly say that at times she has acted as a confidante for me.

I would next like to thank Dr. Shibu K. Mathew. I was fortunate to be able to work closely with him during my thesis, and have learnt a great deal of optics as well as programming from him. His dedication towards work is very contagious, although in a very effortless manner. He never let his position come in between any sort of interaction among us.

I am very grateful to Ms. Sara F. Martin for her suggestions and comments on my work from time to time. She is a passionate scientist, and I learned many things through the various interactions I had with her. It was also through the project headed (National Science Foundation, Rapid Award Grant 1024793) by her that I got the opportunity to visit the Dutch Open Telescope. I must also thank the personnel at the Dutch Open Telescope, namely Dr. Rob Hammerschlag, Dr. Felix Bettonvil, and Dr. Guus Sliepen, for all the support that they extended during my observations period at the telescope.

Prof. P. Venkatakrishnan, Head of USO, showed a great enthusiasm in new ideas. I have enjoyed talking to him about work and other matters on several occasions. I must add that although I rubbed him up the wrong way on an occasion or two, he never held it against me. I also thank Prof. Ashok Ambastha for his regular advice on my work. I have very much enjoyed participating in the various activities conducted under his guidance. I sincerely express my gratitude towards both of them.

I am also grateful to the PRL Director, Prof. J. N. Goswami, and all faculty and staff of PRL, for giving me the opportunity to carry out my research. During my stay at Ahmedabad I interacted very freely with Prof. N. M. Ashok and Dr. P. Janardhan, for which I am grateful to them. I very much enjoyed attending the classes taken by Prof.R. Ramesh, Dr. Raghavan Rangarajan, Dr. Dileep Angom. In addition, I would also like to thank the library and computer centre staff for efficiently maintaining the facilities.

I would like to thank Dr. Sanjay Gosain, Dr. Brajesh Kumar, Mr. Raja Bayanna, Dr. Bhuwan Joshi, and Dr. Ramit Bhattacharyya. With these people around, I have felt myself to be in the company of colleagues, and not faculty members. I have enjoyed discussing solar physics informally with them, and have also enjoyed many a light evening together.

Any research institute is nothing if without students, and I am very glad to see this number steadily increasing at USO. I have enjoyed the company of my seniors Ram A. Maurya, Sanjiv Tiwari and Rohan Louis, as also my juniors Vema Reddy, Suruchi Goel, and lately Dinesh Kumar, Upendra Kushwaha, and Wageesh Mishra. We have had a good time together whether it be watching movies, over the meals, or having a party. I believe it is small things like these that enable you to bounce back to the rigours of research. I am especially grateful to Ram from whom I have learnt a lot about IDL. His single-minded dedication towards work is very admirable indeed.

I must also thank Mr. Sudhir K. Gupta and Mr. Mukesh Saradava. Although indirect, their contribution in my thesis is immense in terms of developing the electrical and mechanical systems respectively. I used to find the lathe very attractive, and would occasionally spend some time with Mukesh in the workshop. Mr. Naresh Jain too has been very helpful, be it in providing archival data or ensuring the smooth running of computers and UPS.

The staff, Mr. Raju Koshy, Mr. Shankarlal Paliwal, Mr. Rakesh Jaroli, and Mr. Pinakin Shikari, have provided the full support in administrative matters. With a relatively small set-up at USO, I could approach any of them directly, which made things look easy and lot less official. I have also enjoyed observing at the Spar telescope with Mr. Dalchand Purohit and Mr. Lakshmilal Suthar, shorn

of the scientific jargon. Mr. Ramchandra Carpenter and Mr. Jagdish Chauhan have lent support in several issues from time to time, for which I am thankful to them.

I have enjoyed the warmth and hospitality of all the family members at USO colony, especially, Mrs. Usha Venkatakrishnan, Mrs. Mahima Kanthalia, and Mrs. Sheela Maurya. Presence of the children Vanshita, Muskaan, and Revant indeed made it feel like a family. So much so, that, in Muskaan and Revant I could almost see my own nephew growing up.

My list of gratitude towards USO would remain incomplete if I say nothing of the game of badminton that we used to have every single evening of a weekday. This helped build a bonding between the students, faculty and staff members, like nothing else could. I admit that my hands – and everyone else's too I assume – used to itch to hold the racquet as it neared 6 pm every day.

I cannot forget to mention all my wonderful friends at PRL, and the short but amazing time I spent with them in Ahmedabad. My flat-mates at Tulip, namely, Vimal, Pankaj, and Rabiul will always be very very special for me. My relation with several other batch-mates was such that on arriving unannounced at Ahmedabad at 4 in the morning, I could knock on their doors and would still be welcomed with a smile. I am indeed very fortunate to have such friends as Bhaswar, Suman, Ashok, Arvind, Soumya, Sreekanth, Sandeep, Amzad, Vineet, Ashwini, and other too numerous to list.

At this point names of two people come to my mind with whom I may not be associated closely now, but who have helped me develop myself. One is Prof. M. A. Gadgil, my mathematics tutor back in junior college, whose simplicity I greatly admire. And the other is Prof. V. Balakrishnan, faculty at IIT Madras, from whom I learnt that one should never be afraid of making mistakes. Although there is little chance that any of the two would see this thesis, I would like to thank both of them for the impact they have had on me.

Lastly, I would like to express gratitude towards my parents. Aai and Baba have always been with me through thick and thin. At times it was not easy to do without them, but their encouraging words made me carry on with my work. They

provided me the freedom necessary to concentrate on my research. I also cannot forget to mention the love my sisters, Renuka and Ahilya, and their families, have showered upon me. My nephew, Paritosh, is indeed a bundle of joy, and it is extremely pleasurable to see him grow an inch or two every time I meet him. I must say, that being away from home, I have missed innumerable opportunities to be with my family members. But, they have always been by my side all the while.

Anand D. Joshi

Abstract

Prominences appear as bright arcs hanging above the solar limb, or as dark thread-like structures when seen against the solar disc, where they are known as filaments. The two terms, prominences and filaments, therefore, are often used interchangeably. They have a lower temperature and higher density, in comparison with the surrounding plasma. The long axis of prominence, known as the spine, is always found to lie along a magnetic neutral line, *i.e.* between regions of oppositely directed photospheric magnetic field. The prominence plasma is supported by means of the magnetic field that threads its structure. Overlying the prominence is a set of coronal arcades that connects the regions of opposite magnetic field that lie on either side of the prominence.

Prominences are typically long-lived structures, with their lifespan ranging from about a day to several weeks. There are mainly two theoretical models, which explain this stable phase of a prominence, viz, Kuperus-Raadu (KR) and Kippenhahn-Schlüter (KS). The two models mainly differ in the manner in which the magnetic field supporting the prominence threads through the plasma. Observational conditions that lead to the formation of a prominence are also fairly well-accepted.

It is observed that prominences end their life on the Sun in the form of eruptions, which may be manifested in several ways. Often, it is found that the eruptive prominences are associated with an expulsion of a large amount of mass from the corona, which is known as a coronal mass ejection (CME). Together with the flares, CME and prominence eruptions form the process of a solar eruption. While earlier researchers argued to prove which phenomenon drives the other one, it is now agreed upon that all the three are manifestations of an overall change in the magnetic field configuration of the corona. It has to be pointed out that even then, the theoretical advances in the field of prominence eruption have not been at par with those of flares and CMEs. Models of CMEs are in place to discuss the various triggering mechanisms, however, such models for prominences are largely absent.

For over 50 years prominences are observed in the chromospheric Hα line at 6563 Å, a spectral line in the Balmer series of neutral hydrogen atom. Apart from Hα, filaments are also observed in the He I infrared line at 10830 Å. For more than past 15 years though, filaments are also observed in several extreme ultraviolet wavelengths, like 195 Å and 304 Å. This has allowed the researchers to explore hitherto unseen aspects of prominence evolution, especially their eruptions.

In my thesis, I have studied different aspects of prominence eruptions. It is through such studies that the understanding of prominence evolution can be furthered, and reliable models can be built based on the inputs provided. Such studies were earlier carried out using observations from a single spacecraft, which can only observe the various phenomena projected on to the plane of sky. However, I have used observations from the two-spacecraft Solar TErrestrial RElations Observatory (STEREO), on which stereoscopic reconstruction technique has been applied. Thus, the conclusions presented in this thesis are based on the true dynamic changes occurring in three dimensions. In addition, I have also used the STEREO observations to study the dynamics of CMEs and the erupting prominences that were associated with them.

The CMEs have gained additional significance in recent years because of their ability to create geo-effective storms on interacting with the Earth's magnetosphere. As most of the CMEs are associated with eruptive prominences, it is possible to have some kind of warning mechanism that would predict an imminent CME. Thus, to monitor the initial stages of prominence eruptions, we have developed an instrument at Udaipur Solar Observatory, named the Hα Doppler Imager, that would observe the full solar disc in Hα line. The Doppler observations in Hα line would allow us to measure the line-of-sight velocities of activated and erupting filaments. In order to facilitate real-time monitoring of filaments, I have also developed an automated algorithm that would not only detect but also track the size and shape of filaments on the solar disc. This algorithm can be used to predict a filament eruption based on a threshold criterion determined from its application to several observations of eruptive filaments.

In addition, I have also utilised Doppler observations from the high-resolution

Dutch Open Telescope (DOT), having a small field-of-view. Analysing Doppler observations would help in building similar tools for the Hα Doppler Imager at USO. I have analysed a filament, observed from the DOT. It shows a barb, which is an appendage running from the spine down to the photosphere, displaying rapid changes in its structure in a short span of about 2 hours. The Doppler observations combined with line-of-sight magnetograms allowed us to study this event in detail.

Thus, in my thesis, I have observed several prominence eruptions, and the associated CMEs, using moderate as well as high resolution observations. While doing so, I have developed techniques to achieve three-dimensional reconstruction and automated detection of filaments. These have helped me to study different aspects of prominences in their activated and eruptive stages, and the conditions determining their propagation.

Chapter 1

Introduction

1.1 What are Prominences?

1.1.1 Observations

Solar prominences were first observed in the form of *mountains* above the solar limb during total solar eclipses. Indeed, the nomenclature comes from the French word *protuberance*, which literally means a protrusion or mountain. We now know the prominences to be features suspended in the Sun's atmosphere. When seen against the Sun's surface, they appear as dark, thin threads, where they are known as filaments. Filaments and prominences, thus, are two different perspectives of looking at the same solar feature. Prominences and filaments have been a subject of study under modern solar physics for more than 50 years.

Traditionally, prominences are observed in the first line of the Balmer series of the hydrogen, famously known as the Hα line, with wavelength 6562.8 Å. When seen against the solar disc, filaments absorb all of the light in the Hα line, and re-emit it. However, the amount of light the filament re-emits in the direction of the observer is very small compared to light in the same wavelength band coming from the rest of the solar disc. As a result, the filament appears dark on the disc (Zirin, 1988). However, when seen against the dark sky, the light emitted by prominences towards the observer is more than that scattered by the tenuous corona, due to which they appear bright.

Apart from the Hα line, other lines in the visible and invisible part of the solar spectrum are also used to observe filaments. Schmahl *et al.* (1974), using the spectrometer aboard Skylab spacecraft, have demonstrated successfully that the extreme ultraviolet region can be used to study filaments. Vial, Salm-Platzer, and Martres (1981) utilised the Stellar and Planetary Physics Laboratory (LPSP) instrument on board the *OSO-8* spacecraft to observe the filaments. They determined the widths and shifts of absorption lines Ca II H (3968 Å) and K (3933 Å) among others, and found line-of-sight velocities of the filaments to be of the order of 10 $\mathrm{km\,s^{-1}}$. Observations of filaments are also carried out in the He I line (10830 Å).

Since the launch of *Solar and Heliospheric Observatory* (SoHO) in 1995 (Domingo, Fleck, and Poland, 1995), the *Extreme-Ultraviolet Imaging Telescope* (EIT) (Delaboudinière *et al.*, 1995) has been extensively used to observe filaments as well as prominences in He II 304 Å. In 2006, the *Solar TErrestrial RElations Observatory* (STEREO) spacecraft was launched (Kaiser *et al.*, 2008). STEREO is a two-spacecraft system carrying identical instruments. One of the two spacecraft leads the Earth in its orbit (Ahead), and the other lags behind the Earth's orbit around the Sun (Behind). *Sun Earth Connection Coronal and Heliospheric Investigation* (SECCHI) is a suite of instruments on board the two spacecraft containing coronagraphs, *COR1* and *COR2*, *Extreme UltraViolet Imager* (EUVI), and Heliospheric Imagers, *HI1* and *HI2* (Howard *et al.*, 2008). Of these, the coronagraphs and EUVI instruments can together observe the solar prominences right from the solar surface up to a few solar radii above it. While the coronagraphs on board STEREO, and the two HI instruments image the corona and the interplanetary space in white-light, the EUVI images in four wavelengths, 171 Å (Fe IX), 195 Å (Fe XII), 284 Å (Fe XV), and 304 Å (He II). The EIT instrument on board SoHO also imaged the solar atmosphere in the same four wavelengths.

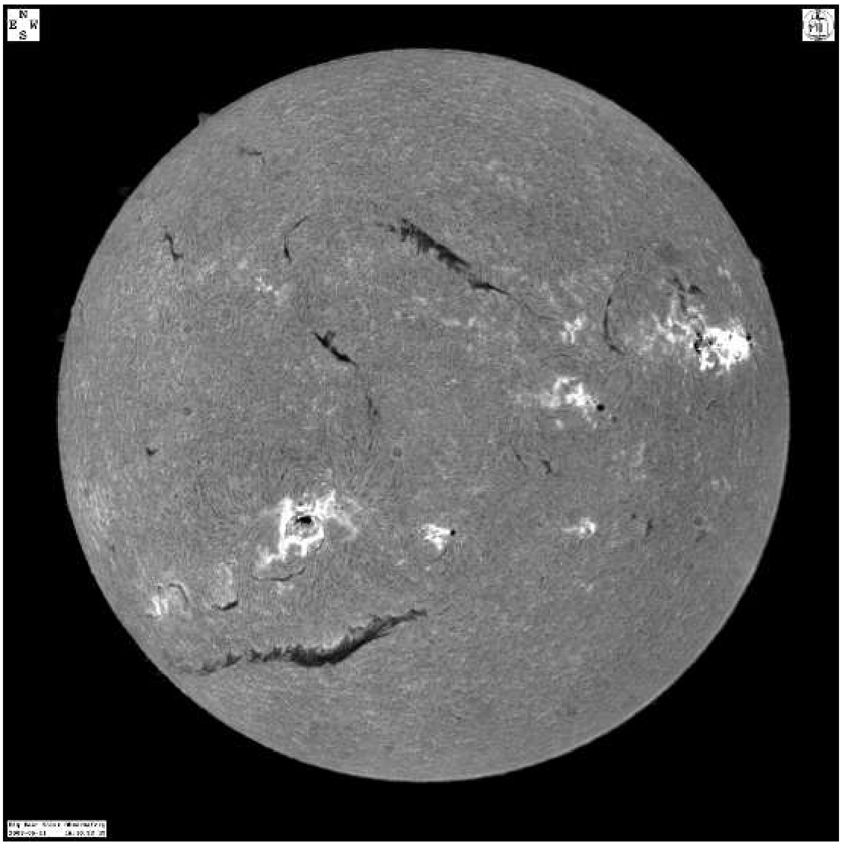

Figure 1.1 A full disc image of the Sun in Hα from Big Bear Solar Observatory (BBSO), taken on 2003 June 11. Two quiescent filaments, one in each hemisphere, can be seen in the image, in addition to several smaller ones, and a few active region filaments.

1.1.2 Physical Characteristics

Prominences are found in the layer of solar atmosphere, known as the chromosphere, or the lower corona. Chromosphere, which literally means coloured sphere, was named so by 19$^{\text{th}}$ century solar astronomers because of the distinct red or pink arcs seen in this layer during a total solar eclipse. The chromosphere is a relatively thin layer, about 2000 km in width above the solar surface, *i.e.* the photosphere. Temperature of this layer is around $8000 - 10000\ K$, while its density is 10^{15} m^{-3}. Thus, chromosphere has a higher temperature, and lower density than the underlying photosphere, with the values $6000\,K$ and 10^{17} m^{-3}. The temperature further rises, and density drops very rapidly through the transition region and into the

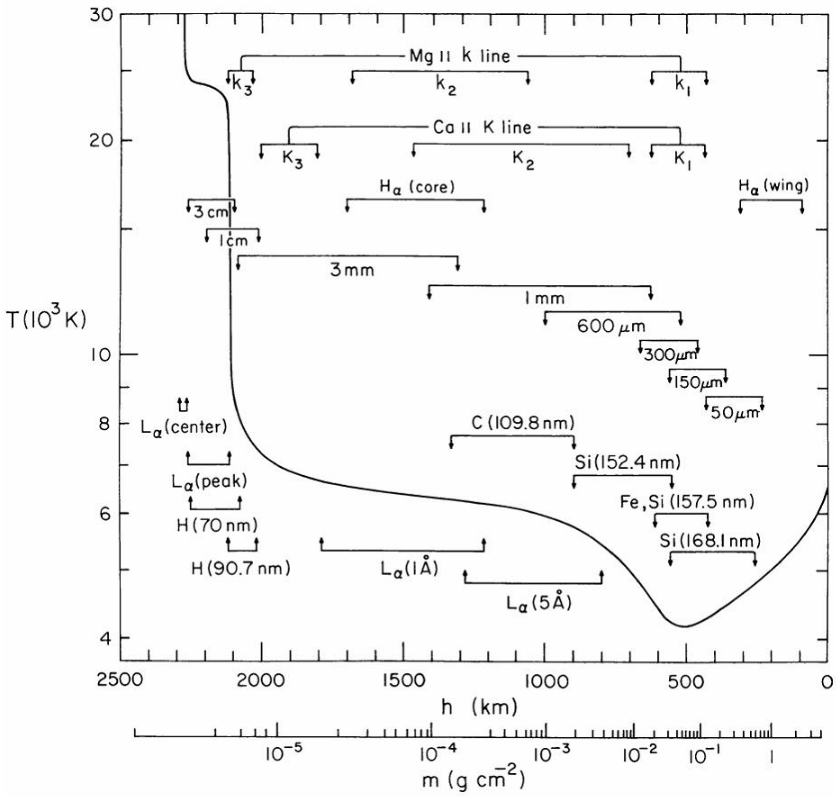

Figure 1.2 Variation of temperature with height and density in a quiet Sun region, adopted from Vernazza, Avrett, and Loeser (1981). Various spectral lines are also shown with respect to their physical parameters of origin.

solar corona. The change in temperature with height in the solar atmosphere is shown in Figure 1.2. The figure also shows the heights and temperatures over which many of the solar spectral lines are formed.

Prominences or filaments are thin long thread-like structures. Based on their physical properties, they are classified as *active region* and *quiescent*, as shown in Figure 1.3. The active region prominences are found in and around the active regions (ARs), *i.e.*, areas with high magnetic fields. On the other hand, the quiescent prominences are found away from the active regions, in what is known as the *quiet Sun* region or areas with low magnetic fields. Another class, the intermediate prominence, is also used sometimes to denote prominences that straddle both the quiet region and the AR, or share properties of both the types (Engvold, 1998).

Earlier, additional categories for prominences were in place, like, sunspot-type, tornado, eruptive, surges, sprays, hedgerow, etc. We now understand that these are mere manifestations of prominences in various stages of their periods of stay on the Sun. The different manifestations, however, also underline the complex nature of the solar prominences.

Prominences are cool and dense plasma suspended in the solar chromosphere, or the lower corona. Their temperature ranges from $5000 - 8000$ K, while the number density ranges from $10^{16} - 10^{17}$ m^{-3}. Temperature and density of the surrounding solar atmosphere are roughly 10^{6} K and 10^{15} m^{-3}, respectively. Prominences are typically long-lived structures on the Sun. The active region prominences have a lifetime of a few days, while quiescent prominences can stay on the solar disc for several weeks together. The reason the cool and dense prominences are suspended above the photosphere in a hot and tenuous environment for such long periods is the magnetic field threading through them.

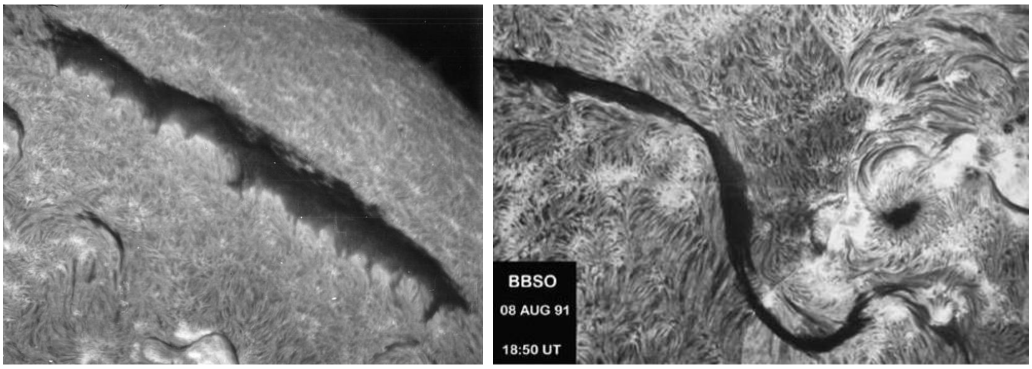

Figure 1.3 A quiescent filament observed from Udaipur Solar Observatory (USO) on 1990 April 11 (*left panel*), and an active region filament observed from BBSO (*right panel*).

It was first reported by Babcock and Babcock (1955) that prominences lie between regions of oppositely directed photospheric magnetic fields. Now we know this to be true without any exceptions (Zirker, 1989). The long axis of the prominence, often seen as a well-defined sharp edge is known as the *spine*. The spine therefore lies along the line along which magnetic field changes its polarity. This line is known as the polarity inversion line (PIL), or simply neutral line. Length of the spine varies from $50 - 200 \times 10^3$ km, while the width is in the range of $4 - 15 \times 10^3$ km, giving the prominence its long thread-like shape. Using high resolution observations in Hα from the Swedish Solar Telescope (SST), Lin *et al.* (2005) could resolve an individual filament thread, and have found their sizes to be less than $0.3''$, *i.e.* $\lesssim 2100$ km. Prominences are not restricted to the chromosphere alone, and can be found up to a height of $0.1\,R_\odot$ above the photosphere. Effectively, their heights range from $10 - 100 \times 10^3$ km. Active region prominences are generally smaller than the quiescent ones.

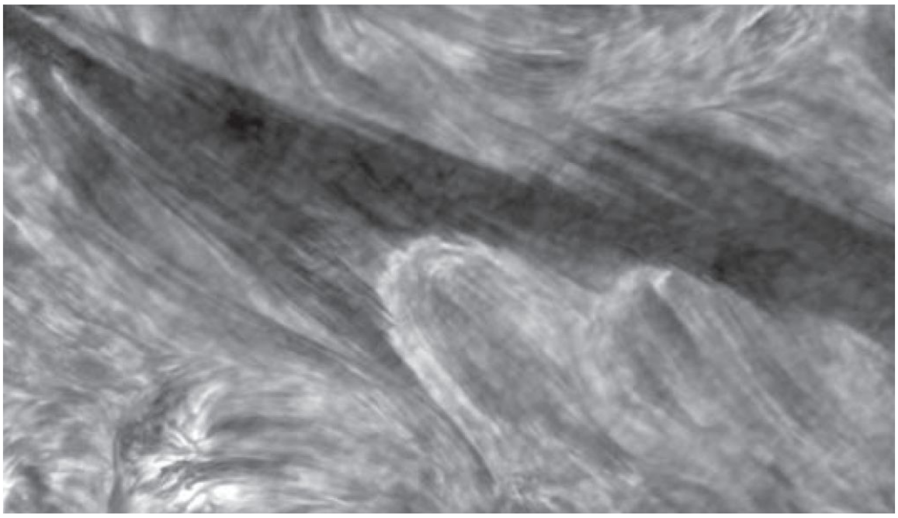

Figure 1.4 High resolution observations of filament threads seen in Hα on 2003 August 26 from the 1-metre Swedish Solar Telescope. The field-of-view shown here is around 48" $\times$ 27". (Adopted from Lin *et al.* (2005))

1.2 Fine Structure and Magnetic Configuration

Engvold (1976) reviewed the prominence fine structure using Hα observations. He found that prominences are composed of both fine threads and knots. The threads are aligned more or less parallel to the prominence spine. Later, Engvold (1998) found the individual threads to be 5000–15000 km in length, and thickness in the range of 200–1500 km. In the same paper, he observed motion in the bright knots, and determined their velocities to be $5 - 50\,\mathrm{km\,s^{-1}}$.

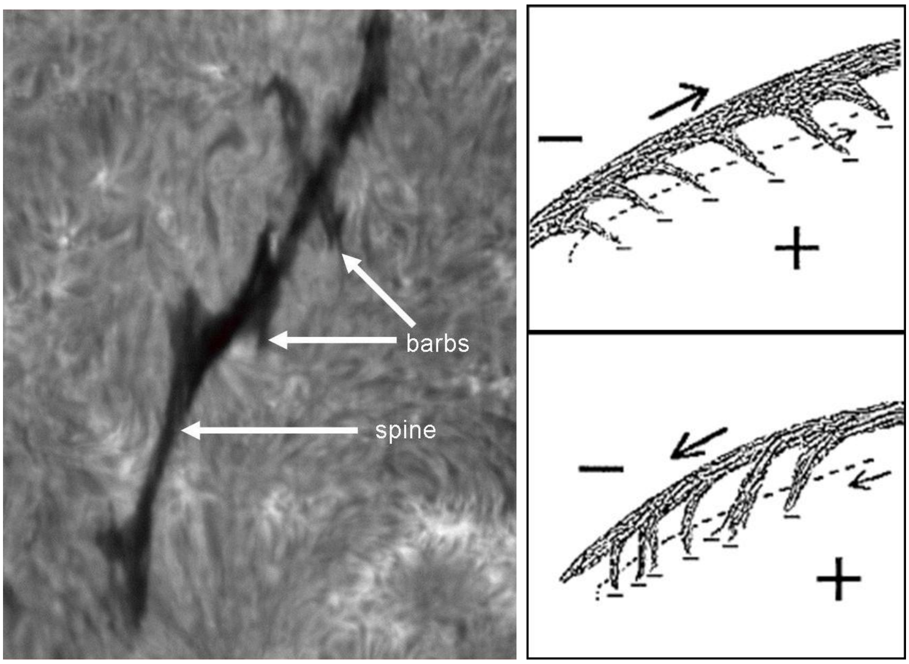

Figure 1.5 *Left panel:* An image of a filament with its spine and barbs marked and identified by arrows. *Right panel:* The two possible orientations of filaments are shown using a cartoon sketch. Filaments with barbs pointing to the right are known as dextral (*top right*), while those with their barbs pointing to the left are known as sinistral (*bottom right*). (Adopted from Martin (1998a)).

Even under moderate resolution, filaments reveal a very conspicuous structure in the form of appendages that extend outwards on either side of the spine. If the filament is located close to the solar limb, the appendages are seen to extend downwards, all the way to the photosphere. These appendages are known as *barbs*, and are believed to lend stability to the filament structure (Engvold, 1998). A very interesting aspect of the barbs, is that they do not extend in a direction perpendicular to the filament spine; instead they are seen to veer either to the left or to the right. Thus, based on the direction in which the barbs are pointing, filaments are classified as *dextral*, the ones which have right-bearing barbs, and *sinistral*, having left-bearing barbs (Martin, Bilimoria, and Tracadas, 1994). This property of the barbs, and consequently that of the filament is known as *chirality*. The direction towards which the barbs turn away from the spine before reaching the photosphere is independent of the direction from which one is looking at the filaments, *i.e.* the barbs point in the same direction as seen from either side of the filament. Further, it is observed that the barbs are rooted in minority or parasitic polarity on either side of the filament spine (Martin, 2003). Figure 1.5 shows spine and barbs of a filament, and also shows schematic diagrams of dextral and sinistral filaments.

1.2.1 Formation and Stability

Martin and her colleagues have extensively worked on the formation, stability and morphology of prominences (Martin, 1973; Martin, Bilimoria, and Tracadas, 1994; Martin and Panasenco, 2010). Martin, Livi, and Wang (1985) have suggested that a region where positive and negative magnetic elements cancel is a potential site for filament formation. Gaizauskas (1998) first reported that a filament always forms in or above what is known as a *filament channel*. The filament channel can be identified by several closely spaced chromospheric fibrils near the neutral line, which precedes the actual filament formation (Martin, 1998a). While the channel is seen to appear a few days prior to the filament formation, it is said to be fully developed and ready to host a filament when there are no fibrils crossing the neutral line (Martin, 2003).

Waldmeier (1970) in his study of a filament using the two coronal emission lines, 5303 Å and 6374 Å, found that there is a *arcade* of magnetic loops overlying the filament, and that between the filament and the arcade is a low-density *cavity*. It was later extablished by Martin (1998a) that the coronal arcade is a prerequisite for existence of a filament. The arcade is nothing but magnetic field lines above the filament spine, that connect the regions of magnetic field on the two sides of a filament. However, it also has to be stated that there can be a neutral line without a filament (Tandberg-Hanssen, 1995) or a coronal arcade that does not host a filament (McIntosh *et al.*, 1976). Thus, we find that neither the neutral line nor the coronal arcade are sufficient conditions for the formation of filaments.

We have briefly covered the prominence environment conducive or necessary for its formation, but it is another question as to how the prominence actually forms. The scenario that is most accepted for filament formation is *condensation*. Normally, the heating and cooling processes are in equilibrium in the solar corona. However, in response to a loss of the thermal equilibrium, a condensation of coronal plasma around a magnetic field may take place leading to the formation of a filament (Hildner, 1974; Tandberg-Hanssen, 1995). Priest and Smith (1979) have reproduced the observed values of filament temperature and density using linear force-free field model in a thermally unstable plasma. Malherbe and Priest (1983) have proposed current sheet models for filaments suspended in a potential magnetic field. Malherbe *et al.* (1983) have further extended the same model to account for mass flows in the prominence.

1.2.2 Prominence Models

At this juncture, it is necessary to explain the magnetic configuration of filaments. It is known that a filament or prominence has opposite magnetic fields in the photosphere on either side. In the model, the prominence is visualised as a vertically standing plasma sheet above the PIL. Supporting the filament plasma within this overlying magnetic arcade is the filament magnetic field. This field originates in the positive polarity, enters the prominence from one end, and exits from the other end to be anchored in the negative polarity (Tandberg-Hanssen, 1995). The coronal arcade forms a helmet streamer within which lies the prominence, and is seen as a set of narrow field lines extending to a great distance into the corona.

Magnetic field measurements form a basis for building up any filament model. Zirin and Severny (1961) were the first ones to measure longitudinal magnetic field in a prominence using the Zeeman effect. They used measurements in the Hβ line (4861 Å) to determine magnetic field of about 200 G (1 Gauss = 10^{-4} Tesla) for the active region prominences, and 25–50 G for the quiescent ones. Using polarimetric measurements, and subsequent inversion, the vector components of the field were also determined (Leroy, 1979). The Hanle effect was also successfully used by Bommier, Sahal-Brechot, and Leroy (1981) to determine the vector field of prominences. They found the magnetic field strength to be of the order of tens of Gauss for the prominences analysed.

Babcock and Babcock (1955) established that a prominence is found between regions of opposite polarity, *i.e.* along a PIL. Shortly afterward, without an explicit knowledge of the magnetic fields involved, researchers began to propose theoretical models for prominences. Based on this very important input from Babcocks, one can have two basic configurations of prominences. The prominence can lie between the positive and negative magnetic polarities of the same bipolar region, or between the positive and negative polarities of two adjacent bipolar regions. The first of the two configurations was proposed by Kippenhahn and Schlüter (1957), and the prominences are also known as normal polarity or of the Kippenhahn-Schlüter type. The second scenario was proposed by Kuperus and Raadu (1974), wherein, the prominences involved are known as inverse polarity or of the Kuperus-Raadu type, named after the authors. The two types are shown in Figure 1.6.

Furthermore, the manner in which the plasma is embedded in the prominence field is also a matter of debate. Antiochos and Klimchuk (1991); Antiochos, Dahlburg, and Klimchuk (1994) proposed that in the normal polarity prominences, a concave-upward *dip* in the magnetic field supports the prominence plasma. This dip is assumed to be very shallow, *i.e.* its vertical spread is very small compared to its horizontal spread. Another model for the prominence field is the flux rope model, which assumes that the prominence magnetic field forms a helical flux rope at the bottom of which lies the prominence plasma (Rust and Kumar, 1994). An important distinction between these two models is that while the dip model can support only the normal polarity prominences, the flux rope model can support both the normal and inverse polarity prominences. Both these models in com-

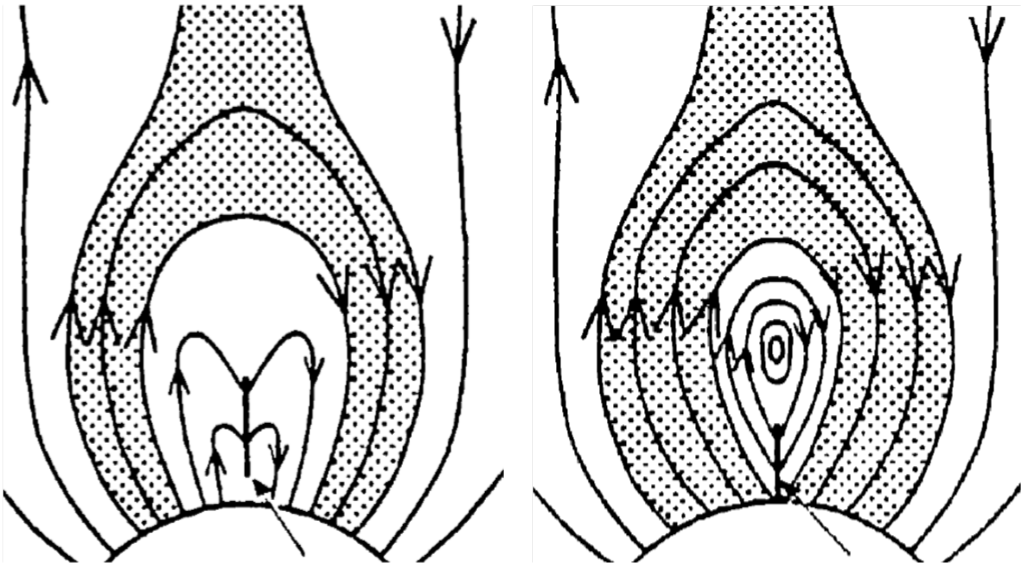

Figure 1.6 The normal polarity *(left)* and the inverse polarity *(right)* prominence models. The vertical line marked by an arrow is the prominence sheet. The shaded region denotes the helmet streamer enclosing the cavity embedding the prominence (Low, 1996).

bination with the normal and inverse polarity types of prominences is shown in Figure 1.7. To explain the chiral patterns of filaments, and their relation with other sunspot features, the flux rope model enjoys an upper hand (Rust and Martin, 1994).

However, over the past decade several observations have challenged the idea of a prominence being a static structure. Mass flows are known to exist for a long time especially in prominences (van Ballegooijen and Martens, 1989, and references therein). Litvinenko (1999, 2000) have proposed that these flows are caused by magnetic reconnection at the photosphere, and that reconnection also leads to photosphere flux cancellation, which is responsible for the formation of the filament in the first place. Thus, the current understanding of filaments is that they are dynamic entities showing a continuous exchange of mass with the underlying photosphere, and it is this mass flow that supports the filament mass against gravity (Karpen *et al.*, 2001; Sara Martin, *private communication*).

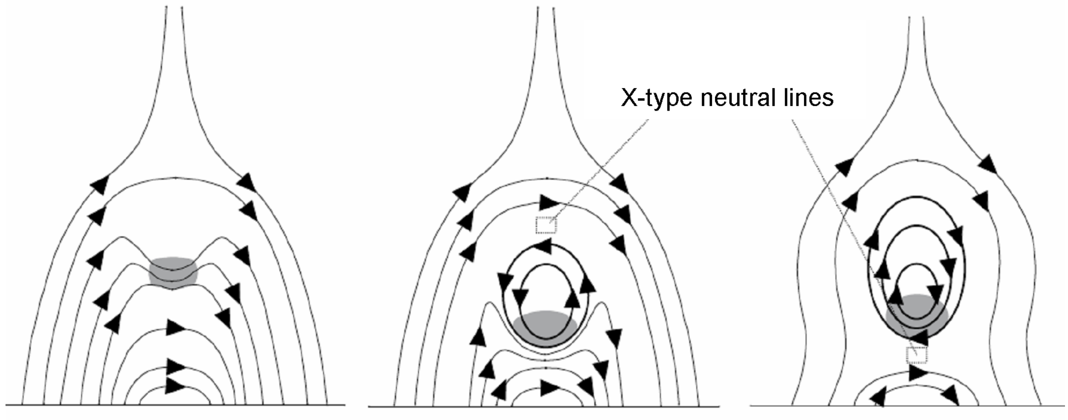

Figure 1.7 The normal polarity dip model *(left)*, normal polarity flux rope model *(middle)*, and the inverse polarity flux rope model *(right)* of prominence magnetic field. The prominence plasma is shown with the help of shaded area in the figures (Gilbert *et al.*, 2001).

1.3 Eruptive Prominence (EP)

Although prominences are long-lived structures, their fine structures undergo a lot of changes even in short time scales. Zirker, Engvold, and Martin (1998) have used Doppler observations in the Hα line, that revealed mass motions occurring in fine threads all along the filament spine simultaneously in both wings of the spectral line, as well as in the plane perpendicular to the line of sight, *i.e.* the plane of sky. They have termed this motion as *counter-streaming*.

Most of the prominences end their lifetimes on the Sun in the form of eruptions (Filippov and Den, 2001). A prominence is said to erupt when it becomes unstable and rises. Parts of it become fainter and eventually disappear, and the rest of its mass may fall back and join the formation of a new prominence. It is widely accepted that the stored magnetic energy is suddenly released that leads to its eruption (Low, 1981; Forbes, 2000). However, the reason for such a sudden destabilisation is still not precisely known. Prior to the actual prominence eruption though, changes in the prominences environment have been observed by various researchers. Feynman and Martin (1995) have observed that an emerging emerging

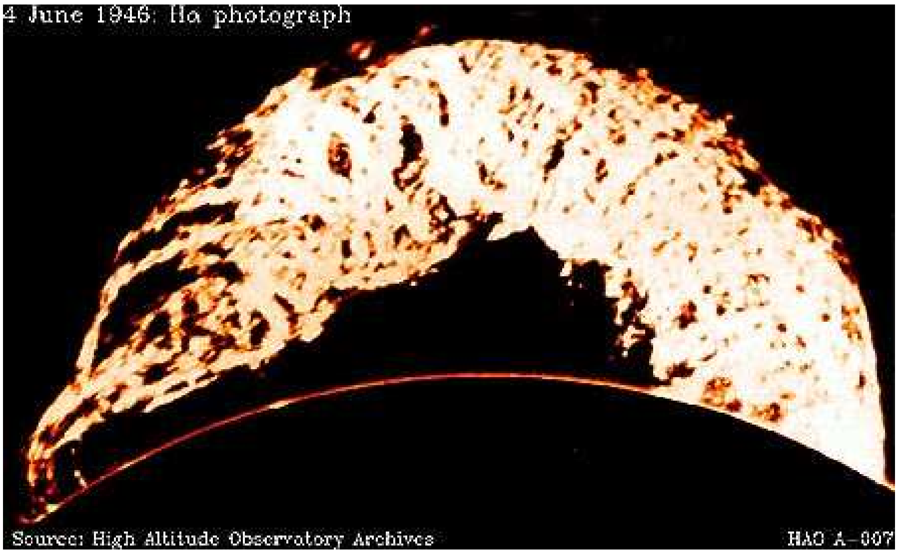

Figure 1.8 A very famous gigantic prominence, nicknamed as the *granddaddy*, observed in Hα on 1946 June 4 from the High Altitude Observatory (HAO).

flux close to a filament can lead to its eruption and a coronal mass ejection (CME), described in detail in the next section. When it comes to triggering the CMEs, Moore (1988) have regarded the flares or filaments responsible. A contrary view has been proposed by Low (1996), who regards the various eruptive phenomena as different manifestations of the solar corona in response to the changes in magnetic fields.

It is not just the triggering mechanisms that are numerous, a prominence is also known to erupt in a variety of ways. Raadu *et al.* (1987) have termed prominences that rise slowly over a long period of time as *disparition brusques* (DBs). Prominences during their eruption have been reported to exhibit a helical nature by several workers (Vršnak *et al.*, 1988; Vršnak, Ruzdjak, and Rompolt, 1991; Srivastava, Ambastha, and Bhatnagar, 1991). CMEs associated with eruptive prominences (EPs) too are known to show a helical structure (Dere *et al.*, 1999).

A filament eruption can be either confined or eruptive (Török and Kliem, 2005). A confined eruption is one in which the filament is seen to rise, but a CME does not occur with it, reforming the filament in such a process. On the other hand, in an eruptive case, a CME is observed along with the filament eruption. Filaments are also known to erupt such that one of its footpoints remains anchored to the photosphere (Tripathi, Isobe, and Mason, 2006). Tripathi *et al.* (2009) have studied such prominences which erupt only partially, and have tried to predict the observable parameters using flux rope model.

A phenomenon displayed by prominences during their eruptions that has been relatively recently uncovered by Martin (2003) is the *roll effect*. The observations suggest that in such cases the prominence can be treated as a ribbon. During eruption, this ribbon-like prominence starts to roll at the top, and the roll then propagates down the prominence legs, giving rise to twists in mutually opposite directions in the two legs. Because of the two directions in which a prominence can roll, Bangert, Martin, and Berger (2003) and Panasenco and Martin (2008) regard the roll effect as a dynamic form of chirality.

1.3.1 Coronal Mass Ejections

Coronal Mass Ejections (CMEs) are solar phenomena that are very closely associated with prominences. Most of the CME models too take into account the filaments involved in the process. CMEs were first observed as *coronal depletions* by Hansen *et al.* (1974) from the ground based K-coronameter. A flare or a prominence eruption always seemed to accompany these depletions. Later, as spacecraft-based coronagraphs were launched, study of the solar corona gained momentum. Gosling *et al.* (1974) analysed 30 CMEs, which they named as *coronal transients*, from the coronagraph on board the Skylab spacecraft and arrived at an estimate of the mass and energy carried by these structures.

The CMEs usually display a 3-part classical structure (Illing and Hundhausen, 1985). The outermost bright loop is known as the CME front or the leading edge (LE), followed by a dark cavity. The cavity in turn is followed by a bright knot,

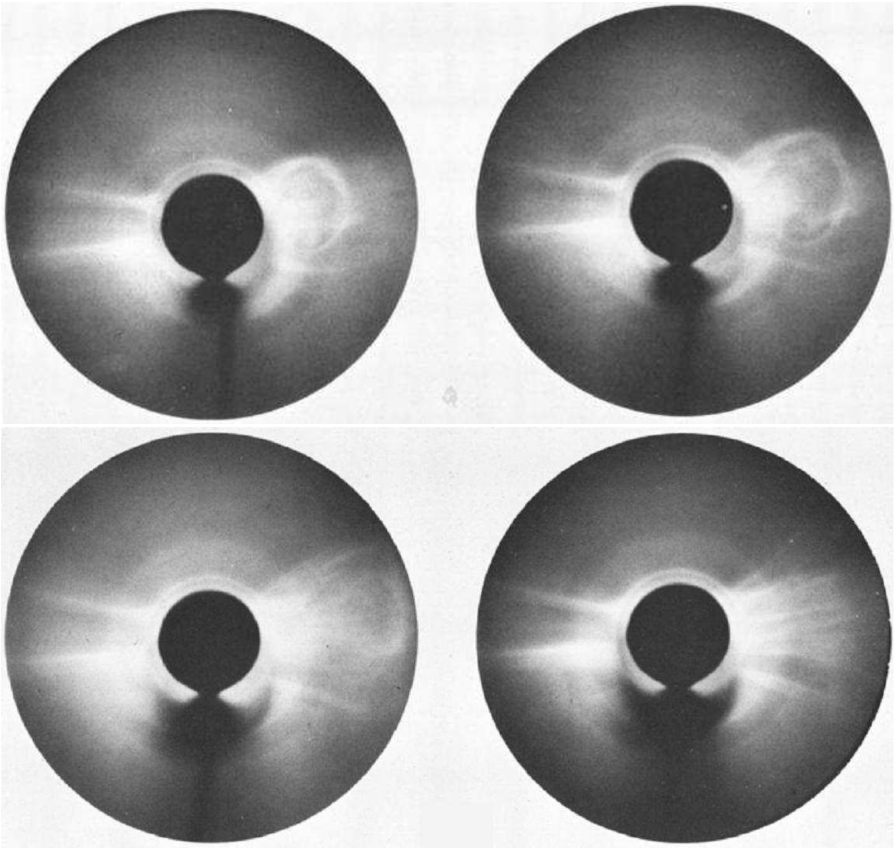

Figure 1.9 Images of a CME, then known as a coronal transient, from the Skylab taken on 1973 August 10. Times of the images in UT are 14:24, 14:48, 15:12 and 16:37 (Gosling *et al.*, 1974).

which is believed to be the material of the prominence associated with the CME. It is observed that the overlying coronal arcade swells gradually before the onset of a CME (Hundhausen, 1993). However not all the CMEs show this kind of structure, as is evident from the right panel of Figure 1.10. Since the launch of SoHO spacecraft which carries the *Large Angle Spectrometric COronagraph* (LASCO) (Brueckner *et al.*, 1995), more than 10000 CMEs are detected. Their typical speeds have been measured, and known to vary from as low as $100\,\mathrm{km\,s^{-1}}$ to more than $3000\,\mathrm{km\,s^{-1}}$ in some cases (Yashiro *et al.*, 2004; Gopalswamy *et al.*, 2005). Yashiro *et al.* (2004) have catalogued the white-light CMEs observed by SoHO/LASCO during the period from 1996 to 2002. The LASCO catalogue of CMEs can be found at http://cdaw.gsfc.nasa.gov/CME_list/index.html.

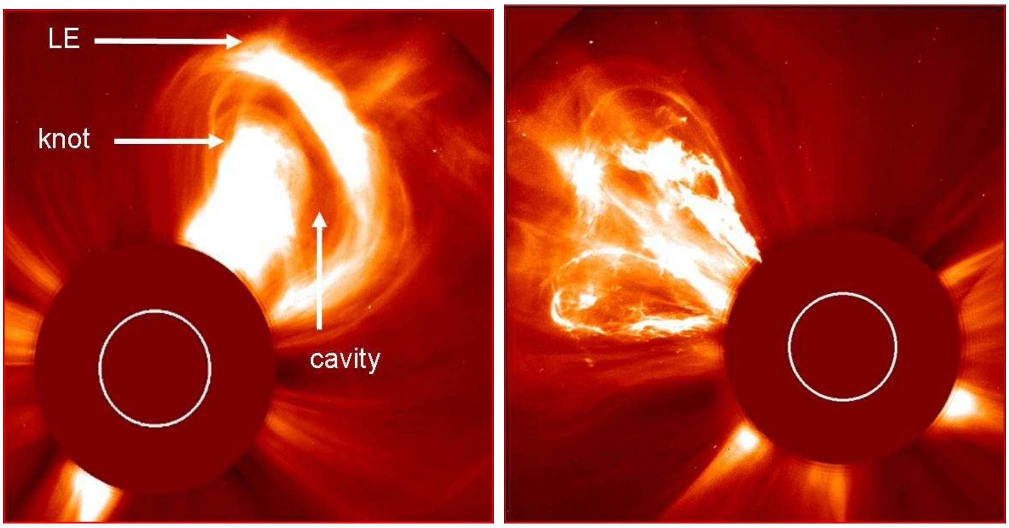

Figure 1.10 Two CMEs observed from the LASCO C2 coronagraph on board SoHO spacecraft. The white ring marks the solar limb, while the dark circle covering the part of the lower corona is the occulter. (Left panel:) A CME on 2002 December 2 showing a classic 3-part structure with leading edge, cavity, and bright knot. (Right panel) However, not all CMEs adhere to this classic structure, as is seen from the one on 2003 April 25.

1.3.2 Eruptive Prominence-CME Association

Webb, Krieger, and Rust (1976) were among the first ones to point out a relation between the two phenomena. They observed co-spatial enhancements in X-ray images following disappearances of quiescent filaments seen in Hα. Munro *et al.* (1979) have found that more than 70% of CMEs had associated eruptive prominences or filament disappearances. Gopalswamy *et al.* (2003) analysed all CMEs from January 1996 up to December 2001 observed by the Large Angle Spectrometric Coronagraph (LASCO) on board Solar and Heliospheric Observatory (SOHO), and compared them with prominence events observed from the Nobeyama Radioheliograph (NoRH, Nakajima *et al.*, 1994). Out of the 186 prominence events covered by both LASCO and NoRH, they found that 134 (72%) had near simultaneous ($\sim$30 minutes) CMEs associated with them. Srivastava and Venkatakrishnan

(2004) have found that low-latitude EPs, in particular, those lying close to the central meridian of the Sun, are important, as they are most likely to give rise to severe geomagnetic storms at Earth. Moreover, intensities of geomagnetic storms are also correlated with initial speeds of CMEs (Srivastava and Venkatakrishnan, 2002).

The reason that the study of EPs associated with CMEs assumes importance is because the CMEs are known to be the main drivers of geomagnetic activity. If the magnetic field of particles carried by the CMEs is favourably directed, it can reconnect with magnetic field in the Earth's atmosphere, inducing heavy currents. This is known as a geomagnetic storm. These currents can become powerful enough to disrupt power transmission and pose a threat to artificial satellites.

1.4 Motivation and Objective

Solar prominences have been a subject of rigorous study for more than 50 years. Conditions leading to the formation and stability of prominences is fairly well-understood. Also, much is known about the different types of magnetic configurations that a filament can have. Despite all the progress, there are quite a few unanswered questions, some of which I have addressed in this thesis.

Although filament models explain their existence, there is no model in place that tackles the eruption of a filament. At the most, they are treated as a current sheet, acting as a site of reconnection in models that discuss triggering of CMEs and flares. Part of the reason for this gap in understanding is the lack of knowledge of the different dynamical processes that a filament experiences during the eruption, and more importantly before it. For example, it is known that filaments undergo slow rise prior to their eruptions, however, this has never been taken into account in any of the models.

The association between CMEs and eruptive prominences is known for a long time now. It is widely accepted now that one is not a consequence of the other, rather both are part of a wider phenomenon, that can be explained by means of reconnection via different models. However, once initiated, it is not certain whether the driving forces acting on a CME and those acting on the associated EP are the same or different. We also do not know whether only physical parameters, as listed above, separate quiescent prominences from the active region ones, or the forces acting on the two types are fundamentally different, especially during their eruptive stages.

Prominences assume significance because of the geomagnetic effects caused by CMEs associated with them. It would be of great value to the field of space weather, if we are able to predict a filament eruption. A filament is known to undergo a slow rise for several hours prior to the actual eruption. However, it is not possible to measure slow rise of filaments on the disc from Hα images alone. One way to achieve this is to monitor filaments close to the disc centre continuously, and measure their line-of-sight velocities using Doppler measurements. High Doppler shifts can be used as a forewarning of activation in filaments and the blue shifts would be indicative of a rising filament. This will be a useful input for space weather studies.

1.4.1 Chapterwise Details

I have thus introduced solar prominences in a manner that is relevant to the work carried out for my thesis. I have also tried to bring out some of the unsolved questions still facing the solar physics community as far as the prominences are considered. With this in mind, I now present a brief description of each chapter in my thesis.

Kinematics of Eruptive Prominences As summarised above, a prominence during its eruption is known to exhibit varied phenomena. In particular, I would like to examine, by applying stereoscopic reconstruction technique, if filaments experience the two-phase rise as previously reported by various authors. I would also like to find out if different phenomena of the EPs are independent or linked together.

In this chapter results from the analysis of two EPs using images from the EUVI instrument on board STEREO spacecraft will be presented. The EPs are observed from a few hours prior to their eruption, allowing us to study the slow-rise phase. Acceleration of the EPs during this phase and the fast eruptive phase is determined, and conclusions from this study will be presented. A stereoscopic reconstruction technique to obtain true coordinates of a solar feature, developed for the twin STEREO spacecraft will also be presented.

Prominence-CME Association It is well known that very often CMEs are accompanied by EPs. However, the relation between acceleration of CMEs and EPs is not very clear. Whether the two phenomena experience the same driving forces always, is still a matter of debate.

In order to address this issue, six CMEs and the prominences associated with three of them are analysed in this chapter. One of the CMEs showed unusually high value of acceleration for a small flare, while two of the three prominences showed very high values of acceleration even at a height of 4 $R_\odot$ from the Sun centre.

Hα Doppler Imager Filaments are extensively studied using observations in Hα. However, from Hα images alone, we have no information about the activation of filaments. This is important from the point of view of space weather, since filaments close to disc centre can potentially lead to CMEs that affect the Earth (Srivastava and Venkatakrishnan, 2004).

The *Hα Doppler Imager* is a new instrument developed at the Udaipur Solar Observatory (USO) to monitor solar filaments and their activation and eruption, by measuring their line-of-sight velocities. The optical layout of the instrument is discussed in detail, and preliminary observations taken using this instrument from it are presented. An algorithm to automatically detect and track filaments on a full-disc Hα image will also be presented. This will be useful for forewarning of eruptive filaments, and thus will aid space weather prediction.

High Resolution Observations of Filaments Observations in high resolution over a small field of view taken from the Dutch Open Telescope at La Palma is presented. The speckle reconstruction that is routinely applied to DOT images is discussed in addition to the method for obtaining line-of-sight velocity maps. Observations of a filament showing an activated barb taken on 2010 August 20 is presented in detail. These are compared with simultaneous observations of magnetic field from the Solar Dynamics Observatory. The possible causes leading to the barb activation have been studied.

Conclusions and Future Work The contents of the thesis are summarised, and main conclusions are highlighted in this chapter. Further scope for research in this field has also been brought out.

Chapter 2

Method of Analysis

There are a host of phenomena taking place on the Sun, especially during the maximum of a solar cycle, like prominence eruptions, CMEs, flares, waves, etc. Of these, I am particularly interested in eruption of prominences, and the CMEs associated with them. There are varied means employed to study them. There can be a spectroscopic study, or a study carried out using an analytical or a numerical model. A major part of my thesis deals with the study of dynamics of solar eruptive phenomena, in particular using the stereoscopic observations from the STEREO spacecraft. This involves measuring the coordinates of solar features, seen on the disc or in the corona against the background of the sky, and determining their speed and acceleration values. In this chapter, a stereoscopic reconstruction technique that we have developed for use with images from the STEREO spacecraft is described in detail. The technique is also validated by comparing our results with those from another technique.

First the ways in which observations of the dynamical studies have been carried out in the past will be discussed. While doing so, some of the significant instruments, and important results derived using them will be described in brief. Later, the general method of stereoscopic reconstruction to obtain three-dimensional coordinates of solar features, and also some of the reconstruction techniques used by various researchers will be discussed. In the last part, the reconstruction technique developed by us will be presented and validated.

2.1 Projected Measurements

The solar eruptive phenomena have captured the interest of solar physicists for many decades now. Earlier researchers used to rely on ground-based observatories alone for observations. However, to observe the solar corona, space-borne coronagraphs proved to be better, as they could observe higher into the corona. Also, to study the solar atmosphere in the ultraviolet and lower wavelengths, one needs to go beyond the Earth's atmosphere. One of the ground-based coronagraphs was the *MK-III K-coronameter* at Mauna Loa Solar Observatory (MLSO), using which Fisher and Garcia (1984) had detected a 'coronal transient'.

There were a few coronagraphs on board satellites launched in the decades of 1970 and 1980, like Skylab (MacQueen *et al.*, 1974), OSO satellites (Koomen *et al.*, 1975), Solar Maximum Mission (SMM), etc. However the satellite that was a major improvement in terms of both sensitivity and field-of-view (FOV) was the *Solar and Heliospheric Observatory* (SoHO) (Domingo, Fleck, and Poland, 1995). SoHO carried the *Large Angle Spectrometric COronagraph* (LASCO) (Brueckner *et al.*, 1995), which is a suite of three coronagraphs, namely, C1, C2 and C3 with FOVs ranging from $1.1 - 3.0\,\mathrm{R}_\odot$, $2.0 - 6.0\,\mathrm{R}_\odot$, and $3.7 - 32.0\,\mathrm{R}_\odot$, respectively. Of these, the C1 coronagraph observed in two coronal emission lines: the Fe XIV green line at 5303 Å and the Fe X red line at 6374 Å. It however stopped working only 2.5 years after its launch in December, 1995. The C2 and C3 are white-light coronagraphs, which observe the Thompson-scattered light from electrons in the corona.

Apart from the coronagraphs, the Extreme Ultraviolet Imaging Telescope (EIT) (Delaboudinière *et al.*, 1995), is another very important instrument on board the SoHO satellite to study the dynamics of solar eruptions. EIT images the solar corona in the four emission lines in the extreme ultraviolet region with wavelengths

171 Å (Fe IX), 195 Å (Fe XII), 284 Å (Fe XV), and 304 Å (He II). The temperature of these lines range from around 80000 K to 3 MK. High temperature plasma from the coronal loops and arcades can be studied in these wavelengths. Also, the prominences can be seen very well up to a height of 0.5 $R_\odot$ above the solar surface in the He II 304 Å line. The 304 Å images from EIT were shown to provide a significantly different perspective from the Hα observations that were predominantly used to study filaments until then (Wang *et al.*, 1998).

Since the launch of SoHO, CMEs and their association with EPs has been extensively studied. In fact, SoHO has detected more than 10000 CMEs and has also turned out to be the most successful comet hunter in the human history. However, the studies of CMEs conducted using just one viewpoint suffer from an inherent limitation due to the fact that the measurements are carried out in the plane of the sky. In other words, we measure distance of a solar feature as projected on to the plane of the sky, and do not have information on the actual distance at which the feature lies from the Sun. To give an example, just by looking at a CME from the coronagraph alone, we would not be able to tell if the CME is coming towards the Earth or going away from the Earth, *i.e.* if it originated from the front side of the solar disc or from the far-side.

2.2 STEREO spacecraft

In order to facilitate the task of three-dimensional reconstruction of features on the Sun, the Solar TErrestrial RElations Observatory (STEREO) (Kaiser *et al.*, 2008) satellite was launched in 2006. It consists of two spacecraft, STEREO Ahead (A) and Behind (B) which orbit the Sun in approximately the same orbit as that of Earth. STEREO A however leads the Earth, and also lies closer to the Sun than Earth, hence it goes round the Sun faster. STEREO B, on the other hand, lags behind the Earth in its orbit, and is slightly farther from the Sun compared to the Earth. This makes STEREO B slower in its orbit. Thus, STEREO A moves faster than Earth, and B moves slower than Earth, resulting in an increase in the separation angle between the two spacecraft at the rate of about 45° per year.

The two spacecraft carry on them identical sets of instruments, taking coordinated simultaneous measurements of various solar phenomena. The Sun Earth Connection Coronal and Heliospheric Investigation (SECCHI) (Howard *et al.*, 2008) suite of instruments is the most important one for the study of such phenomena. It consists of two coronagraphs, COR1 and COR2, the Extreme UltraViolet Imager (EUVI) and two Heliospheric Imagers, HI1 ($15 - 84\,R_\odot$) and HI2 ($66 - 318\,R_\odot$). As I have used data from coronagraphs, COR1 and COR2, and EUVI for my study, a brief description of these two instruments from the SECCHI suite is given below.

2.2.1 Coronagraphs: COR1 and COR2

The inner coronagraph COR1 (Thompson *et al.*, 2003) has FOV from $1.4 - 4.0\,R_\odot$. COR1 is an internally occulted Lyot coronagraph that observes in a 225 Å passband centred on the Hα line. At this wavelength light, from the Sun is completely blocked up to $1.4\,R_\odot$ and partially vignetted up to $1.4\,R_\odot$. The COR1 provides polarisation brightness images taken at angles 0°, 120° and 240°. These are combined in IDL^{TM} using standard procedures available in SolarSoft library. The images are 1024×1024 pixel^2 in size with a resolution of $7.5''$ per pixel having a highest cadence of 5 minutes. The outer coronagraph on SECCHI, COR2 has FOV from $2.0 - 15.0\,R_\odot$. It is an externally occulted Lyot coronagraph recording polarisation brightness images just as COR1. The COR2 image size is 2048×2048 pixel^2 with a resolution of $14.7''$ per pixel. It has a best cadence of 20 minutes.

2.2.2 Extreme UltraViolet Imager (EUVI)

The EUVI (Wülser *et al.*, 2004) images the solar atmosphere in the same four wavelength bands as in SoHO/EIT, namely, 171 Å, 195 Å, 284 Å, and 304 Å, covering a range of temperatures from 80000 K to 20 MK. The FOV extends up to about 1.7 $R_\odot$. This is a single telescope consisting of a quadrant, where each of the four parts is coated with a narrow-band, multilayer reflective coating, optimized for one of the four EUV lines. The EUVI images are also 2048×2048 pixel^2 in size, and 1.6$''$ per pixel resolution.

2.3 Stereoscopic Reconstruction

To tackle the issue of incomplete information conveyed by projected measurements, the technique of stereoscopic reconstruction is employed in the field of solar physics for quite some time now. It is very much like the way we use our own eyes. The image created on the retina of our eyes is just a projection, but when such images from the two eyes are combined and processed by the human brain, we get a sense of the depth.

As such, any two views of the Sun, separated by some distance should be enough for three-dimensional reconstruction. However, one need to know accurately the position of the two viewpoints with respect to each other, and with respect to the Sun. Such a task was first carried out by (Jackson and Froehling, 1995). They used the two spacecraft, Helios and Solwind as the two viewpoints, and used the tomographic technique to determine electron density and the two-lobed structure of a CME. This task however poses challenges if the measurements are not simultaneous, or if the positions are not accurately known. Aschwanden *et al.* (1999, 2000) have used the method of dynamic stereoscopy to determine the three-dimensional coordinates, density and temperature of coronal loops in an active region. In this method, the angle of view is allowed to vary due to solar rotation to reconstruct solar features that can otherwise be considered to be static. They have used this technique on EIT images to determine the temperature and electron density of coronal loops. The single-spacecraft LASCO measurements were also used by Moran and Davila (2004) in a polarimetric study of CMEs to determine their true coordinates and speeds.

The identical instruments and coordinated measurements from the two STEREO spacecraft are extremely well-suited for stereoscopy. Like most solar observatories around the world, STEREO provides images in the Flexible Image Transport System (*FITS*) format (Wells, Greisen, and Harten, 1981; Hanisch *et al.*, 2001). Additionally, STEREO images also incorporate the World Coordinate System (Calabretta and Greisen, 2002; Greisen and Calabretta, 2002) keywords and those from the Spacecraft, Planet, Instrument, Camera-matrix, and Events kernels (Eichstedt, Thompson, and St. Cyr, 2008), abbreviated as SPICE kernels. These keywords allow users to precisely determine positions of the two spacecraft, which is essential to carry out stereoscopy successfully (Thompson, 2010).

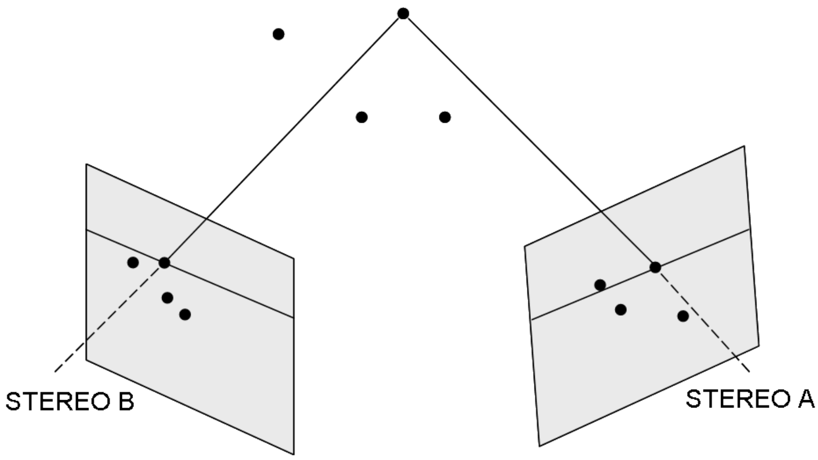

Figure 2.1 Schematic diagram of a few solar features along with their images as seen in STEREO A (right plane) and B (left plane) spacecraft. Lines of sight of one of the features on to both the spacecraft are shown. The horizontal line passing through the feature is the corresponding epipolar line in each image plane. Adopted from Inhester (2006).

The two main geometrical techniques for reconstruction are *tie-pointing* (Thompson, 2009) and *triangulation* (Aschwanden *et al.*, 2008a). Given a feature on the Sun, the lines of sight from each of the two STEREO spacecraft are extended backwards till they intersect each other in space. The point of intersection gives true coordinates of the feature. This technique is known as tie-pointing.

On the other hand, in triangulation, true position of the feature is determined by taking into consideration the angles it subtends to the two spacecraft, and position of the spacecraft.

Before going on to describe some of the commonly used stereoscopic techniques, I will describe in brief the geometrical technique of reconstruction, in general. A feature on the Sun is seen in the images from the two viewpoints. For the sake of argument, we will restrict ourselves to the two spacecraft STEREO A and B. Each of the two images provides two coordinates. However, we have to determine only three physical coordinates of the feature in a suitable coordinate reference frame, making the problem of stereoscopy inherently over-dependent. Here we introduce the *epipolar plane*, which is the plane passing through the two spacecraft, and containing the solar feature whose coordinates are to be determined (Inhester, 2006). By definition, the projection of the epipolar plane on to the image plane of the spacecraft will be a line, and is known as the epipolar line. Given the coordinates of the two spacecraft, and image coordinate of the selected feature from one spacecraft, it is possible to determine the epipolar plane uniquely. If a feature is seen on a certain epipolar line from one of the two spacecraft, the *epipolar constraint* requires that the feature lies on the same epipolar line in the image from the other spacecraft (Inhester, 2006). This way, the number of independent image coordinates is reduced from four to three, making the system solvable. Figure 2.1 shows the typical problem of geometrical reconstruction involving two viewpoints, a set of solar features. Images from the STEREO A and B spacecraft are shown on the planes on the right and left of the figure. The epipolar lines corresponding to the feature to be reconstructed are seen as straight lines on the image passing through the feature.

2.3.1 Triangulation

Feng *et al.* (2007) were the first to carry out three-dimensional reconstruction using images from the STEREO spacecraft. In their study, observed coronal loops were fitted with a linear force-free field model to determine the force-free field parameter, α, in addition to the loop length and height. Later, Aschwanden *et al.* (2008a) used a geometrical reconstruction technique to trace the coronal loops seen in EUVI 171 Å images, and obtain their geometrical parameters such as lengths, heights, shapes, etc. In order to run the reconstruction routine, the pair of images from STEREO A and B first have to be coaligned with respect to the spacecraft roll angles, rescaled so that the solar discs are of the same size, and rotated to the A-B plane. Once this is done, the physical coordinates (x,y,z), of a solar feature seen in both the images, are obtained by a geometric triangulation technique. This work has been further extended in Aschwanden *et al.* (2008b), where the electron density and temperature inside coronal loops were determined.

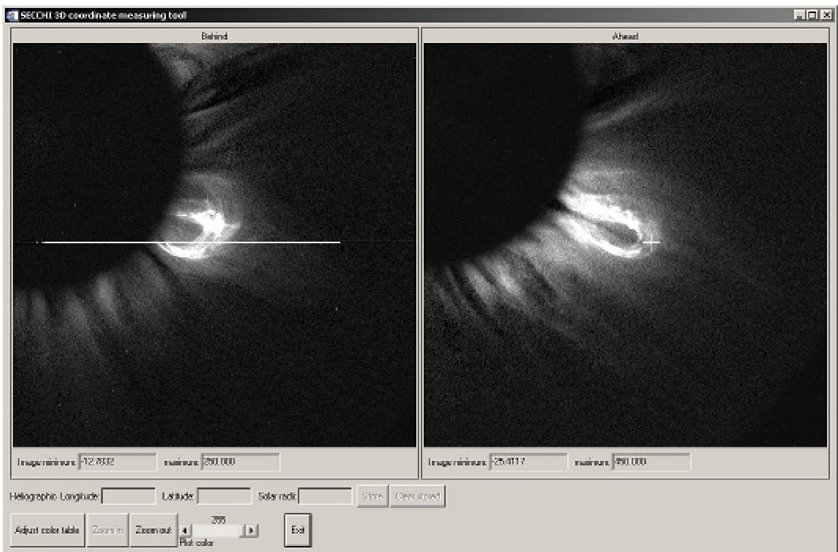

Figure 2.2 The graphical user interface for IDL$^{\mathrm{TM}}$ routine `scc_measure` showing simultaneous images from COR1 B (left pane) and A (right pane) taken on 2008 April 9. A feature in the CME leading edge is selected in the image from COR1 A, and an epipolar line passing through the same feature is shown in the image from COR1 B.

2.3.2 Tie-pointing (`scc_measure`)

This is a three-dimensional triangulation technique developed by (Thompson, 2009). In this paper the technique has been employed to determine the orbit of the bright comet *C/2007 L3 (SOHO)* around the Sun. The main advantage of this technique is that it has a graphical user interface (GUI) written in the Interactive Data Language (IDL$^{\mathrm{TM}}$), which can be used equally well on images obtained from coronagraphs and those from EUVI instrument. The GUI displays a pair of simultaneous images from the two spacecraft. On selecting a feature in one of the two images, an epipolar line is shown in the other image passing through the same feature, as shown in Figure 2.2. This routine has been used by several other researchers to obtain the true coordinates of solar features (Bemporad, 2009; Srivastava *et al.*, 2009; Gosain and Schmieder, 2010 among others).

2.3.3 Forward Modelling

Thernisien, Howard, and Vourlidas (2006) have proposed a *graduated cylindrical shell* (GCS) model for CMEs, in which the CME is treated as a flux-rope structure. A partial toroid is modelled as the CME front, and two cones at each end of the toroid form the "legs" of the CME. Several of the CMEs analysed by Cremades and Bothmer (2004) were fitted successfully using this model. Later, Thernisien, Vourlidas, and Howard (2009) have used the same GCS model in the form of a wireframe to fit the CMEs observed from the twin STEREO spacecraft to determine the true evolution of CMEs. Such a fit is more successful in determining the CME parameters, since there are two views to compare. Also, since the fitting is done interactively, the parameters could be refined by performing several iterations. A GUI has also been developed for this technique to facilitate other users (Thernisien, Vourlidas, and Howard, 2009).

2.3.4 Other Reconstruction Techniques

Even before the launch of STEREO spacecraft, Pizzo and Biesecker (2004) described a geometrical technique to localise the CMEs by making use of synthetic images from the two spacecraft. Mierla *et al.* (2008) have developed the 3D height-time (3D-HT) technique based on the triangulation method to determine true coordinates and the true propagation direction of a CME. Gissot *et al.* (2008) have applied an optical flow algorithm to EUVI images to estimate the depth of an erupting filament. Liewer *et al.* (2009) have developed a technique based on the tie-pointing method to determine the true evolution of an erupting filament. One can also make use of the local correlation tracking (LCT), where correlation along the epipolar lines in the two images is used to automate the feature selection process, followed by a suitable reconstruction method (Mierla *et al.*, 2009). The geometrical reconstruction methods have been reviewed by Mierla *et al.* (2010), and their results are compared against each other.

2.4 Methodology of a new Triangulation Technique

As discussed in § 2.3, although there exist several reconstruction techniques based on different stereoscopic methods, none of these have been used for reconstruction of solar features both on disc and coronagraph images except of scc_measure. We decided to develop a new technique which can be used for reconstructing features in coronagraph images, as well as those on the solar surface, such as in EUV. We have chosen the heliocentric Earth ecliptic (HEE) coordinate system, which we found to be very simple to work with. The technique involves rotating the HEE system separately for STEREO A and B, such that one of the axis of the coordinate system lies along the line-of-sight of each spacecraft. The plane perpendicular to this axis is then nothing but the image plane, *i.e.* the plane of sky for the two spacecraft. We then determine the physical coordinates of a feature in the HEE system by solving the corresponding rotation matrices. We have applied this technique to two events studied by previous workers to evaluate the performance of this technique.

We will determine true position of a point $P(x, y, z)$ in the HEE coordinate system using this technique. The HEE coordinate system is centred at the origin, wherein, its z-axis points towards the ecliptic north pole, x-axis is the Sun-Earth line, while y-axis completes the right-handed triad (Hapgood, 1992; Thompson, 2006). However, for the sake of convenience, which will be highlighted later, we have changed labels of the axes of the HEE coordinate system. The y-axis (Y_{HEE}) now points towards the ecliptic north pole, z-axis (Z_{HEE}) is the Sun-Earth line, and x-axis (X_{HEE}) completes the right-handed triad. To maintain a distinction between the real HEE system and the newly defined HEE system with its axes relabelled, we refer to the latter as rHEE.

We carry out the reconstruction by first rotating the rHEE coordinate system in such a manner that the x and y coordinates in the rotated system are the same as the x and y coordinates of the image as seen by the spacecraft STEREO A and B. Since we know coordinates of the two spacecraft in rHEE system, we can execute the rotations by making use of the rotation matrices. These transformation equations are then used to obtain the true coordinates (x, y, z) of point P in the HEE system. To convert the angular coordinates in the image to physical distances, we assume an affine geometry, *i.e.*, the spacecraft is at a large distance from the Sun compared to the distance between object and the Sun. This is valid, since the COR1 field of view goes up to $4\,\mathrm{R}_{\odot}$, while the STEREO spacecraft are at distances greater than $200\,\mathrm{R}_{\odot}$.

2.4.1 The Rotations

First consider STEREO A alone. Let θ_A and φ_A be its latitude and longitude in rHEE system, as shown Figure 2.3a. We need to perform 2 rotations on the rHEE system to orient it such that coordinates of P in the rotated system, x''_A and y''_A, are same as its x and y coordinates in the image in STEREO A. The two rotations are:

1. Longitude of A, φ_A, is always considered to be positive. Hence, to align the Z_{HEE} axis with the Y_{HEE}-Sun-STEREO A plane, we need to rotate about the Y_{HEE} axis through angle φ_A (Figure 2.3b), to give the modified axes X'_A, Y'_A and Z'_A (Equation 2.1).

2. Latitude of A, θ_A varies periodically between $\pm 0.13°$. Hence, to align the Z'_A axis with STEREO A line-of-sight, we need to rotate about the X'_A axis through angle $-\theta_A$ (Figure 2.3c), to give the modified axes X''_A, Y''_A and Z''_A (Equation 2.2).

We thus have STEREO A looking down the Z''_A axis. In other words, the $X''_A Y''_A$ plane becomes the plane of the sky as seen from STEREO A. The two rotations are illustrated with the help of Fig 2.3.

Now, let θ_B and φ_B be the latitude and longitude of STEREO B in the rHEE system (Figure 2.4a). We carry out two rotations such that the Z''_B axis now aligns with the Sun-STEREO B line, *i.e.* coordinates in the rotated system, x''_B and y''_B, are same as the x and y coordinates of the image in STEREO B.

1. Longitude of B, φ_B, is always considered to be negative. Hence, to align the Z_{HEE} axis with the Y_{HEE}-Sun-STEREO B plane, we need to rotate about the Y_{HEE} axis through angle φ_B (Figure 2.4b), to give the modified axes X'_B, Y'_B and Z'_B (Equation 2.4).

2. Latitude of B, θ_B, varies periodically between $\pm 0.30°$. Hence, to align the Z'_B axis with STEREO B line-of-sight, we need to rotate about the X'_B axis through angle $-\theta_B$ (Figure 2.4c), to give the modified axes X''_B, Y''_B and Z''_B (Equation 2.5).

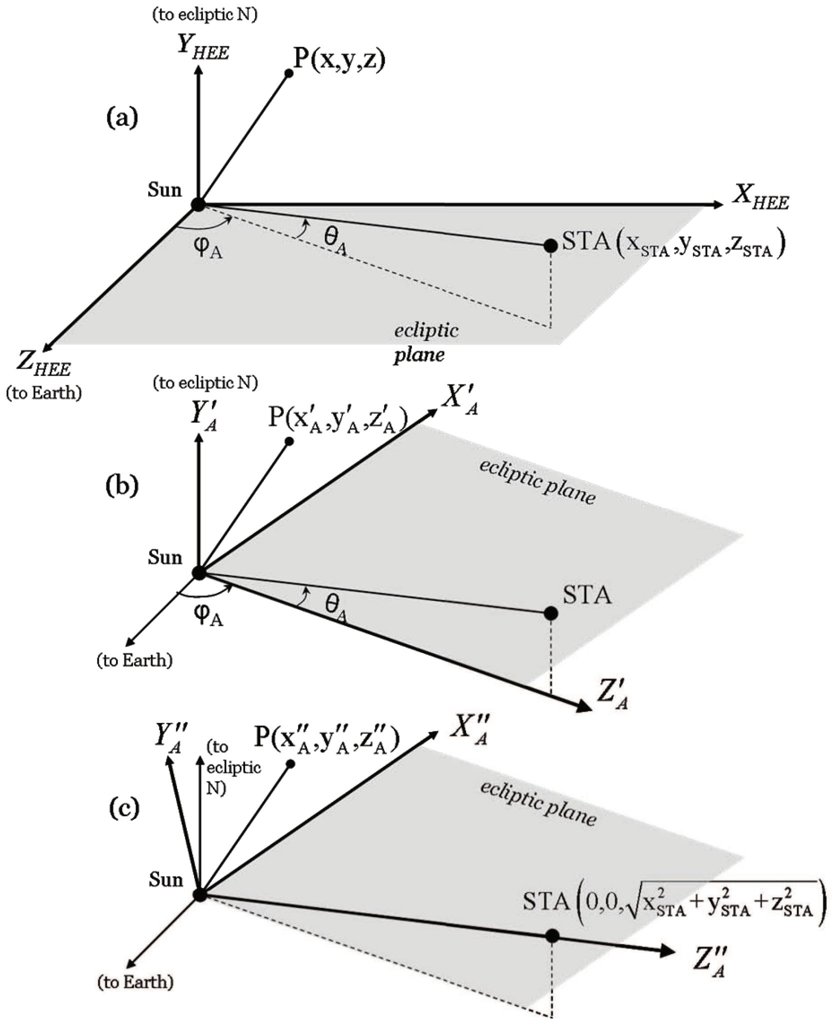

Figure 2.3 (a) Shows a point $P(x, y, z)$ in rHEE system. θ_A and φ_A are latitude and longitude of STEREO A. (b) rHEE system is rotated in anti-clockwise direction about Y_{HEE} through angle $|\varphi_A|$. (c) Rotation about the X'_A axis through angle $-\theta_A$, where the sign of θ_A takes care of the sense of rotation.

2.4.2 The Rotation Matrices

Let us consider the rotation for STEREO A. The first one is a rotation about the Y_{HEE} axis through angle φ_A ($\varphi_A > 0$). Its matrix is given by:

$$\begin{pmatrix} x'_A \\ y'_A \\ z'_A \end{pmatrix} = \begin{pmatrix} \cos\varphi_A & 0 & -\sin\varphi_A \\ 0 & 1 & 0 \\ \sin\varphi_A & 0 & \cos\varphi_A \end{pmatrix} \begin{pmatrix} x \\ y \\ z \end{pmatrix} \tag{2.1}$$

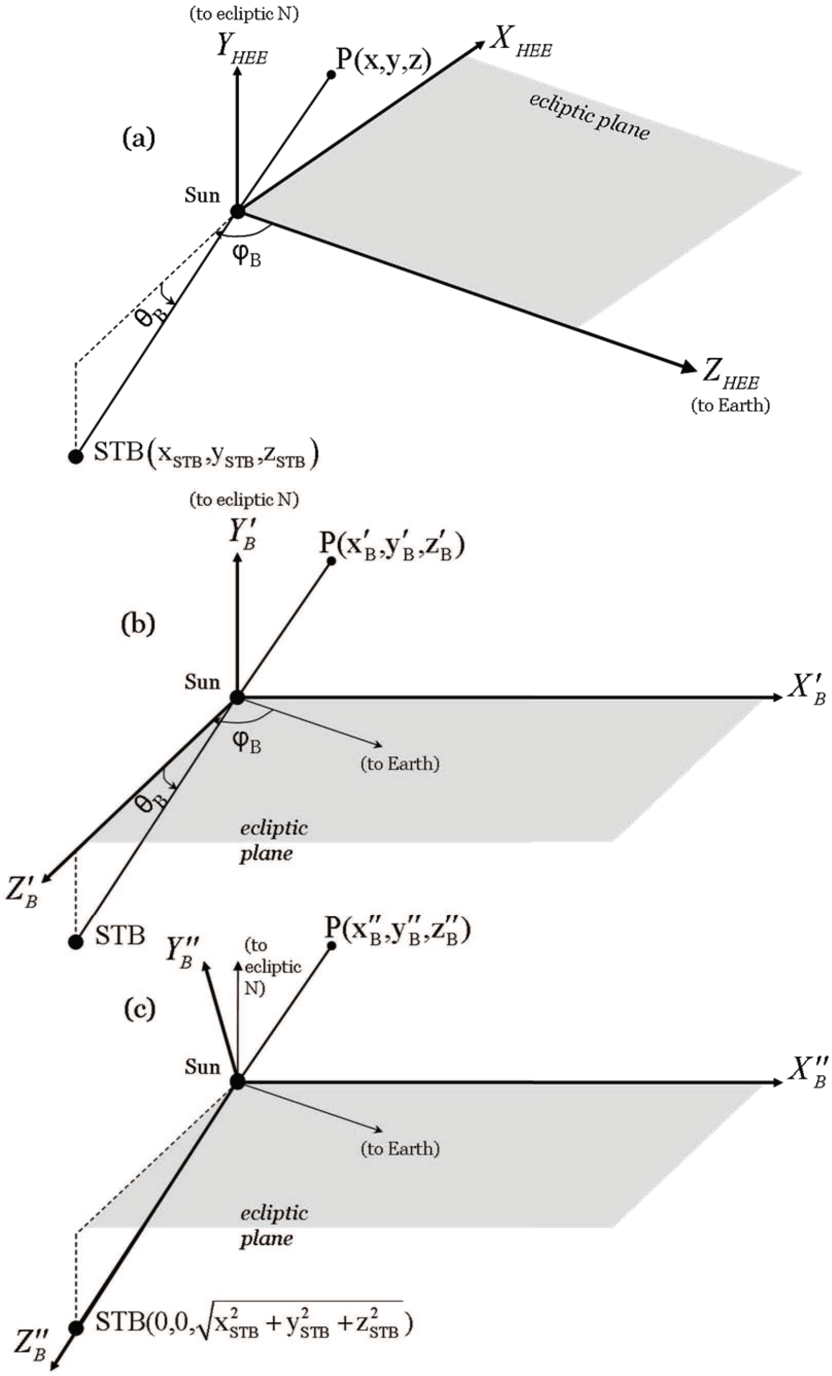

Figure 2.4 (a) Shows a point $P(x, y, z)$ in rHEE system. θ_B and φ_B are latitude and longitude of STEREO B. (b) rHEE system is rotated in clockwise sense about Y_{HEE} through φ_B. (c) Rotation about the X'_B axis by angle θ_B in anti-clockwise direction.

The second rotation is about the X'_A axis through angle $-\theta_A$ ($|\theta_A| < 0.13°$), and it can be written as:

$$\begin{pmatrix} x''_A \\ y''_A \\ z''_A \end{pmatrix} = \begin{pmatrix} 1 & 0 & 0 \\ 0 & \cos\theta_A & -\sin\theta_A \\ 0 & \sin\theta_A & \cos\theta_A \end{pmatrix} \begin{pmatrix} x'_A \\ y'_A \\ z'_A \end{pmatrix} \tag{2.2}$$

θ_A can be both positive and negative. A positive (negative) value of θ_A implies a clockwise (anticlockwise) rotation about the X'_A axis. Thus, the sign of θ_A rightly takes care of the sense of rotation. Figure 2.3 shows STEREO A with a positive value of θ_A. Combining Equations 2.1 and 2.2, gives us:

$$\begin{aligned} \begin{pmatrix} x''_A \\ y''_A \\ z''_A \end{pmatrix} &= \begin{pmatrix} 1 & 0 & 0 \\ 0 & \cos\theta_A & -\sin\theta_A \\ 0 & \sin\theta_A & \cos\theta_A \end{pmatrix} \begin{pmatrix} \cos\varphi_A & 0 & -\sin\varphi_A \\ 0 & 1 & 0 \\ \sin\varphi_A & 0 & \cos\varphi_A \end{pmatrix} \begin{pmatrix} x \\ y \\ z \end{pmatrix} \\ \therefore \begin{pmatrix} x''_A \\ y''_A \\ z''_A \end{pmatrix} &= \begin{pmatrix} x\cos\varphi_A - z\sin\varphi_A \\ -x\sin\varphi_A\sin\theta_A + y\cos\theta_A - z\cos\varphi_A\sin\theta_A \\ x\sin\varphi_A\cos\theta_A + y\sin\theta_A + z\cos\varphi_A\cos\theta_A \end{pmatrix} \end{aligned} \tag{2.3}$$

Similarly, the rotation matrices for orienting the rHEE system to STEREO B are

$$\begin{pmatrix} x'_B \\ y'_B \\ z'_B \end{pmatrix} = \begin{pmatrix} \cos\varphi_B & 0 & -\sin\varphi_B \\ 0 & 1 & 0 \\ \sin\varphi_B & 0 & \cos\varphi_B \end{pmatrix} \begin{pmatrix} x \\ y \\ z \end{pmatrix} \tag{2.4}$$

$$\begin{pmatrix} x''_B \\ y''_B \\ z''_B \end{pmatrix} = \begin{pmatrix} 1 & 0 & 0 \\ 0 & \cos\theta_B & -\sin\theta_B \\ 0 & \sin\theta_B & \cos\theta_B \end{pmatrix} \begin{pmatrix} x'_B \\ y'_B \\ z'_B \end{pmatrix} \tag{2.5}$$

Since $\varphi_B < 0$, Equation 2.4 would always mean a clockwise rotation about the Y_{HEE} axis through angle $|\varphi_B|$. Combining Equations 2.4 and 2.5 gives us:

$$\begin{pmatrix} x''_B \\ y''_B \\ z''_B \end{pmatrix} = \begin{pmatrix} 1 & 0 & 0 \\ 0 & \cos\theta_B & -\sin\theta_B \\ 0 & \sin\theta_B & \cos\theta_B \end{pmatrix} \begin{pmatrix} \cos\varphi_B & 0 & -\sin\varphi_B \\ 0 & 1 & 0 \\ \sin\varphi_B & 0 & \cos\varphi_B \end{pmatrix} \begin{pmatrix} x \\ y \\ z \end{pmatrix}$$

$$\therefore \begin{pmatrix} x''_B \\ y''_B \\ z''_B \end{pmatrix} = \begin{pmatrix} x\cos\varphi_B - z\sin\varphi_B \\ -x\sin\varphi_B\sin\theta_B + y\cos\theta_B - z\cos\varphi_B\sin\theta_B \\ x\sin\varphi_B\cos\theta_B + y\sin\theta_B + z\cos\varphi_B\cos\theta_B \end{pmatrix} \tag{2.6}$$

Thus, (x''_A, y''_A) and (x''_B, y''_B) are the (x, y) coordinates as seen from STEREO A and STEREO B respectively. Note that it is possible to directly equate coordinates of the rotated system to image coordinates of the two STEREO spacecraft because of the unconventional choice of axes that we assumed for the rHEE system.

2.4.3 The Epipolar Constraint

Equations 2.3 and 2.6 together give us a set of 6 simultaneous equations. However, the STEREO A and STEREO B images can provide us only x''_A, y''_A, x''_B and y''_B. Also, since the Z''_A and Z''_B axes are respectively aligned with the STEREO A and STEREO B lines of sight, we do not have any information about z''_A and z''_B. Thus we have the following four relations:

$$x''_A = x\cos\varphi_A - z\sin\varphi_A \tag{2.7}$$

$$x''_B = x\cos\varphi_B - z\sin\varphi_B \tag{2.8}$$

$$y''_A = -x\sin\varphi_A\sin\theta_A + y\cos\theta_A - z\cos\varphi_A\sin\theta_A \tag{2.9}$$

$$y''_B = -x\sin\varphi_B\sin\theta_B + y\cos\theta_B - z\cos\varphi_B\sin\theta_B \tag{2.10}$$

We now have the Equations 2.7–2.10 from which we have to obtain (x, y, z), which is an over-determined system. However, we can solve these equations exactly by invoking the epipolar constraint discussed in § 2.3. Once we identify a feature either in image from STEREO A or from STEREO B, it is possible to determine projection of the epipolar plane passing through the feature selected, on the image from the second spacecraft. The positions of the two spacecraft are precisely known, in addition, we need one more coordinate to specify the epipolar plane uniquely. For this, the two image coordinates from the first spacecraft along with an assumed pair of points are converted to the heliocentric Earth equatorial (HEEQ) coordinate system, thus specifying the epipolar plane independent of the observer. The HEEQ coordinates of these points are then converted to the image coordinates of the second spacecraft to obtain the projection of the two points on its image. The projection forms a line passing through the feature selected in the first image. The images can be oriented so that the STEREO mission plane (the plane containing STEREO A and STEREO B and passing through the Sun's centre) is along the horizontal in both the images (Inhester, 2006) using the standard SolarSoft routine `scc_roll_image` for this purpose. As a result of this orientation, any epipolar plane projects as a horizontal line in the two images. This line then passes through the selected feature in the second image, thus constraining the value of the y-coordinate of the feature in the second image to a known value, which leaves us with three equations.

Since we need to determine the coordinates in the HEE system, we assume that the STEREO mission plane (STPLN) and the ecliptic plane are the same, which is valid since angle between the two planes is less than 0.5°, and can be neglected.

Equations 2.7 and 2.8 are solved for x and z to obtain:

$$x = \frac{x''_B \sin\varphi_A - x''_A \sin\varphi_B}{\sin(\varphi_A - \varphi_B)} \tag{2.11}$$

$$z = \frac{x''_B \cos\varphi_A - x''_A \cos\varphi_B}{\sin(\varphi_A - \varphi_B)} \tag{2.12}$$

Suppose, we select a feature in image from STEREO A first, then we know x''_A, y''_A and $x''B$. The value of y"B is known because of the horizontal epipolar line passing through the feature in the image from STEREO B. Therefore, Equation 2.9 can be used to solve for y along with Equations 2.11 and 2.12 to give,

$$y = \frac{y''_A}{\cos\theta_A} + \left(\frac{x''_B}{\sin(\varphi_A - \varphi_B)} - \frac{x''_A}{\tan(\varphi_A - \varphi_B)}\right)\tan\theta_A \tag{2.13}$$

Similarly, if we select the feature in image B first, then Equation 2.10 can be combined with Equations 2.11 and 2.12 to give,

$$y = \frac{y''_B}{\cos\theta_B} + \left(\frac{x''_B}{\tan(\varphi_A - \varphi_B)} - \frac{x''_A}{\sin(\varphi_A - \varphi_B)}\right)\tan\theta_B \tag{2.14}$$

Thus, we are able to obtain the true coordinates (x, y, z) of point P in the HEE system. The coordinates can then be converted into any other system as required. It should be emphasised that although while making the transformations, we assumed an unconventional choice of axes for the HEE system, the definition of latitude and longitude was not affected. Hence, latitude and longitude for the point P is in the HEE system, as given in the equations below, where r, ϕ and θ are respectively the distance from Sun's centre, longitude and latitude of point P. Also note that we have not imposed any conditions on the location of point P. Therefore, we can employ this technique not just to coronagraph images, but also to solar disc images to determine true height of a feature, like an erupting filament.

$$r = \sqrt{x^2 + y^2 + z^2} \tag{2.15}$$

$$\phi = \tan^{-1}\left(\frac{x}{z}\right) \tag{2.16}$$

$$\theta = \tan^{-1}\left(\frac{y}{\sqrt{x^2 + z^2}}\right) \tag{2.17}$$

We thus have developed a stereoscopic reconstruction technique based on triangulation. The technique can be employed to determine the true coordinates of a solar feature, may it be on the solar disc or out into the corona.

2.4.4 Limitations and Errors of the Technique

Several stereoscopic reconstruction techniques are listed and discussed earlier in this chapter. Some of the techniques are shown to be applicable on coronagraph images (Mierla *et al.*, 2008; Thernisien, Vourlidas, and Howard, 2009), while some others on EUVI images Gissot *et al.* (2008); Liewer *et al.* (2009). Our technique has the advantage of being the only one apart from `scc_measure` (Thompson, 2009) which is demonstrated to be applicable to images obtained from both the coronagraphs and disc images from EUVI. However, the assumption of affine geometry used while deriving the reconstruction equations demands that the distance between a selected feature and Sun should be very small compared to the distance between the spacecraft and Sun. Hence, use of this technique to the HI instrument which images the interplanetary space would give erroneous results.

Human error is the main source of error in any form of stereoscopic reconstruction based on triangulation or tie-pointing. In order to minimise the error, the solar features in the two images should be identified as correctly as possible. For our technique, we have assumed a human error of three pixels in identifying the feature correctly. The error in pixels is propagated using Equations 2.11-2.17 to determine the errors in height, longitude and latitude. The estimated errors in height for EUVI, COR1, and COR2 images are $0.02\,R_\odot$, $0.12\,R_\odot$, and $0.6\,R_\odot$ respectively, while the errors in longitude and latitude are less than $2°$.

2.5 Validation of the Technique

In order to validate the technique, we have compared the results obtained from our technique with those obtained from the well-known technique, `scc_measure` (Thompson, 2009). For this purpose, we have selected a filament eruption on 2007

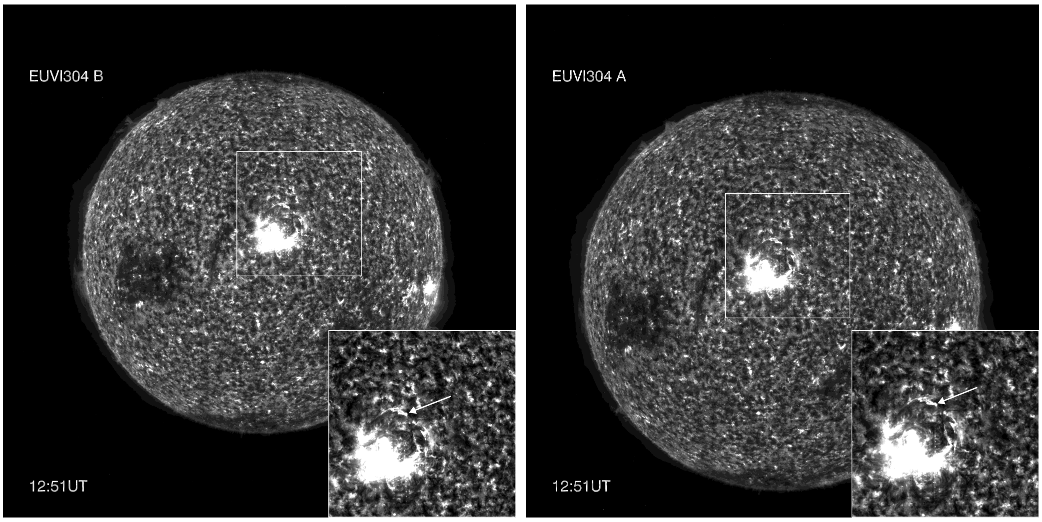

Figure 2.5 304 Å images of a filament eruption on 2007 May 19 as seen from EUVI B (left) and A (right). The box in each panel on the figure shows the area blown up in the inset. The feature used for reconstruction is marked in the inset with the help of an arrow.

May 19 observed in 304 Å images from EUVI. We have selected a bright knot in the filament spine for reconstruction. For this event, the separation angle between the two spacecraft was 8.6°. The second event selected for comparison was a CME observed on 2007 June 05 in COR1. The CME appeared as a very slow moving front at the south-west limb of the Sun. The spacecraft separation angle during this event was 11.3°. Images of both the events from the two spacecraft, along with the feature used for reconstruction, are shown in Figures 2.5 and 2.6.

Results from the reconstruction are shown in Figures 2.7 and 2.8. In the absence of any reconstruction tools, we can obtain speeds from only projected measurements, as can be seen in the leftmost panels of the two figures. Thus, we only have the position angle from the solar north, and the projected height. On applying the stereoscopic reconstruction however, we are able to get full information of the selected features. The middle and right panels in the figures show the reconstructed results from our technique and `scc_measure`, respectively. For the sake of comparison, the y-axis ranges for one coordinate are kept the same for results from the two techniques. The longitudes and latitudes shown are in Stonyhurst

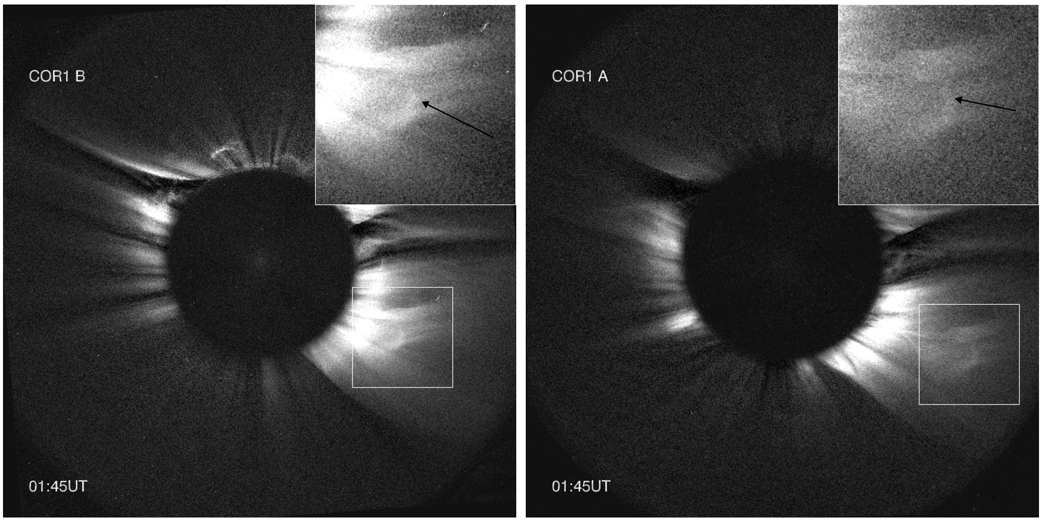

Figure 2.6 Images of CME on 2007 June 05 as seen from COR1 B (left) and A (right). The box in each panel shows the area blown up in the inset. The feature in leading edge used for reconstruction is marked in the inset with the help of an arrow.

heliographic system. In this coordinate system, the longitude is 0° at the central meridian, and increases towards solar west. We can see that results from both the techniques are in very good agreement considering the errors in measurements.

The 2007 May 19 filament was earlier also studied by Gissot *et al.* (2008) and Kilpua *et al.* (2009). It was an active region filament whose eruption was accompanied by a CME. The filament was on the disc centre, and could be seen in emission at the start of its eruption. It rapidly moved across the disc towards the west direction. From Figure 2.7, we find that the filament height remains more or less constant till 13:11 UT, after which the height starts increasing rapidly indicating the onset of eruption. During this period, longitude varies only a little between 3° and 8°, while latitude is almost constant near 14° as determined from the two techniques. As the eruption starts, filament height increases up to 2 $R_\odot$. It should be emphasised that measurement of true height of a filament on the disc is possible because of stereoscopy. From a single viewpoint, one does not have this information at all. During eruption, longitude increases to 13°, confirming the westward motion of prominence, and the latitude shows a slight decrease.

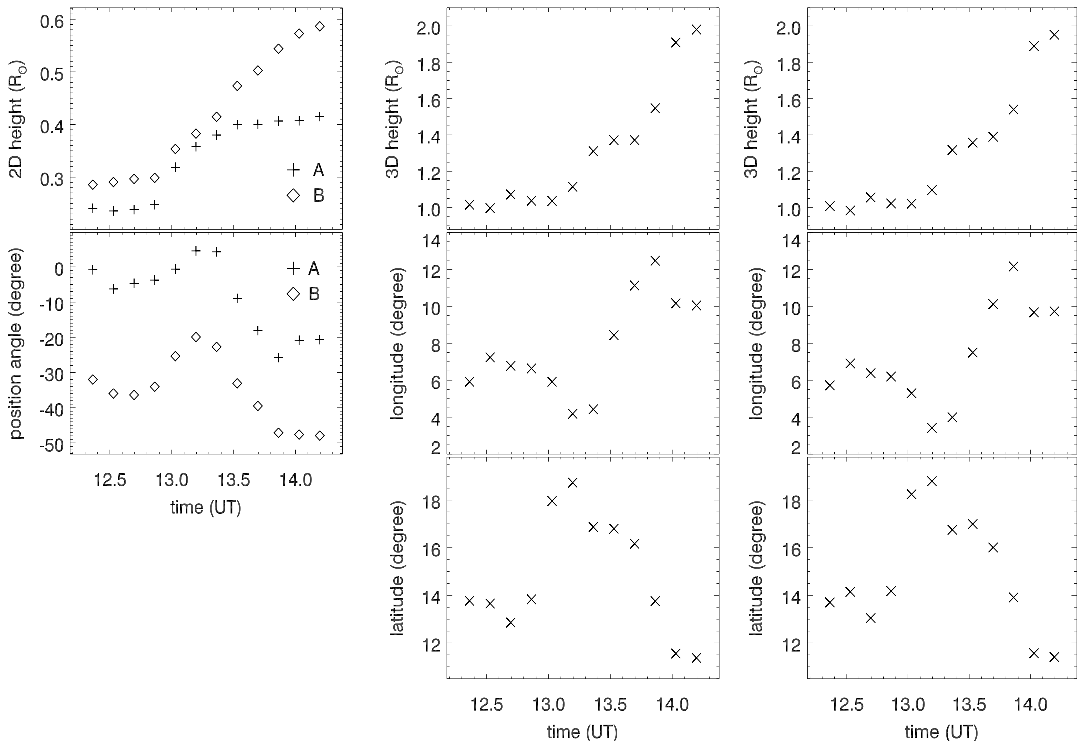

Figure 2.7 *Left panel:* Projected coordinates of the feature in the erupting filament on 2007 May 19 in STEREO A (+ symbols) and B (◇ symbols), marked in Figure 2.5. The true height, and heliographic longitude and latitude of the feature calculated from our triangulation technique are in the *middle panel*, while those from `scc_measure` are in the *right panel*.

The CME on 2007 June 05 occurred in the south-west direction. It was a very slow event showing a faint but well-defined leading edge. During almost 2.5 hours of observation, the true height of a feature in the leading edge increased only by 1 $R_\odot$ giving a speed of 84 $\mathrm{km\,s^{-1}}$ from both the techniques. The heliographic longitude of the CME was centred around 136° from our technique, while it was around 132° from `scc_measure`, indicating that the CME was in the western limb of the Sun, but on the far side with respect to the Earth. The CME latitude was approximately $-21°$ as determined from the two techniques.

Thus, a new triangulation technique is developed for simultaneous pair of images from STEREO spacecraft. This technique is validated, and found to be successful, by comparing its results with those from `scc_measure`, an established

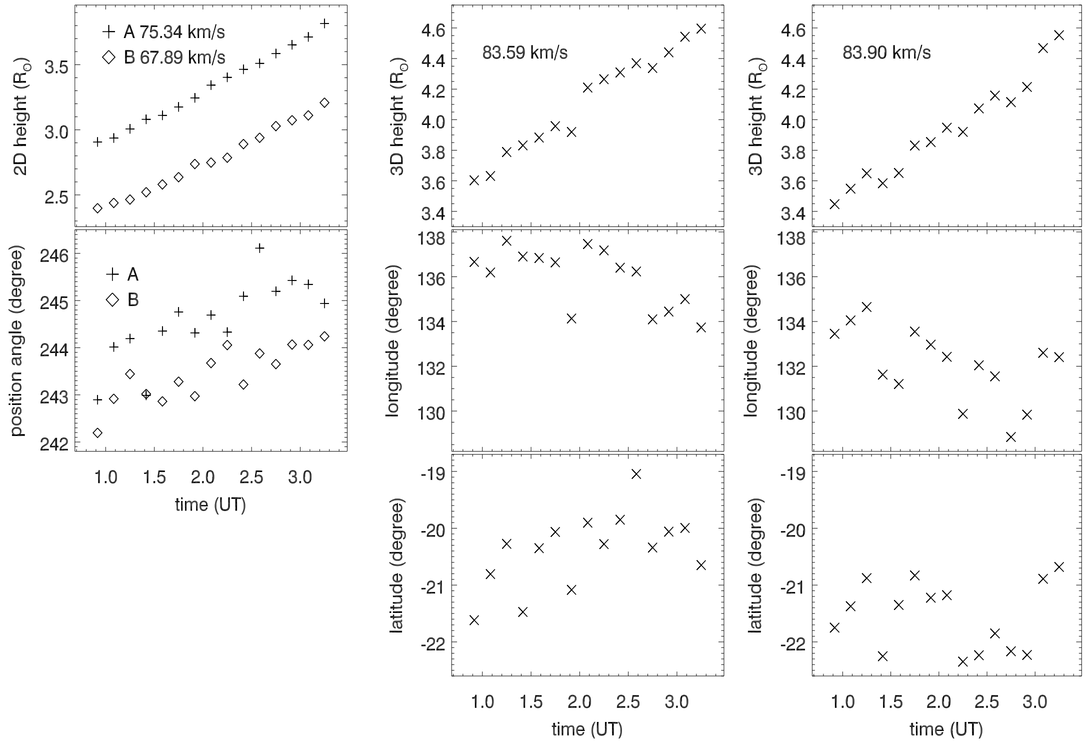

Figure 2.8 *Left panel:* Projected coordinates of a feature in leading edge of the CME on 2007 June 05 in STEREO A (+ symbols) and B (⋄ symbols), marked in Figure 2.6. The true height, and heliographic longitude and latitude of the feature calculated from our triangulation technique are in the *middle panel*, while those from `scc_measure` are in the *right panel*.

reconstruction technique. Our technique is applicable to both on-disc and coronagraph images. Hence, most of the results from reconstruction presented in this thesis are obtained from this technique.

Chapter 3

Kinematics of Eruptive Prominences

3.1 Introduction

Solar prominences most of the times end their life on the surface of the Sun by means of eruption. In § 1.3, we have described the different types of eruptions in brief. In this chapter, we have described some aspects of the kinematics of prominence eruptions, viz, slow-rise before the eruption, helical twist, and non-radial propagation.

Amongst the earliest ones to study prominences during their eruptions was Valniček (1964). He classified the prominences as being parts of a flare, or associated with a flare, or simply of the quiescent type. For the quiescent filaments, he observed that speed increases only slowly at the start of the *disparition brusque*, but it picks up high speed later. Further, he also observed that the active-region prominences had a higher average velocity ($500 - 1200\,\mathrm{km\,s^{-1}}$) than the quiescent ones ($200 - 800\,\mathrm{km\,s^{-1}}$). More recently, Schrijver *et al.* (2008) used the *Transition Region and Coronal Explorer* (TRACE) (Handy *et al.*, 1999) observations to detect slow rise in filaments with velocity of the order of ($1 - 15\,\mathrm{km\,s^{-1}}$). This slow rise of a filament can be understood as a build-up of magnetic pressure inside the filament cavity, that starts to push the overlying coronal arcade (Martin *et al.*, 2008). Similar studies were also carried out by Sterling and Moore (2004a,b, 2005); Joshi and Srivastava (2007), which will be discussed in more detail later.

Vršnak *et al.* (1988) have observed four prominences that exhibited helically twisted structures during their eruption. The twists between the two legs were found to lie in the range 2π to 7π radian. More studies dealing with the helical nature of prominences can be found in the references cited by Vršnak *et al.* (1988). Vršnak, Ruzdjak, and Rompolt (1991) have assumed a helical fit for 28 of such well-observed EPs, including the granddaddy prominence seen in Figure 1.8, and have determined parameters like prominence height, and pitch angle of its helical pattern. A similar study of measurement of physical parameters of EPs showing helical structure was carried out by Srivastava, Ambastha, and Bhatnagar (1991); Srivastava and Ambastha (1998). Gilbert *et al.* (2001) have explained such helical structures by means of a kinking filament.

Non-radial propagation of EPs is a relatively neglected aspect of prominence dynamics. Gopalswamy, Hanaoka, and Hudson (2000a) observed a non-radial structure in EUV wavelengths associated with an EP on 1997 December 14. Plunkett *et al.* (2001) also observed such a non-radial structure accompanying a CME on 1998 June 2 in LASCO C1. It is not yet certain if it is only a coincidence that both the events occurred during the ascending phase of the solar cycle. A simple model was developed by Filippov, Gopalswamy, and Lozhechkin (2001) to explain this motion during the minimum phase of solar activity cycle, wherein they regarded the filament as a toroidal flux rope.

3.1.1 The Roll Effect

Another dynamic phenomenon associated with a prominence in its eruptive stage is the roll effect, first discovered and studied by Martin (2003). The prominence is treated as a ribbon for this purpose. As it starts to erupt, the top of the prominence begins to roll. This roll eventually propagates down the two legs of the prominence, giving rise to twists in the legs in mutually opposite directions. There can be two possible directions of the roll. If we consider the photospheric magnetic polarities on either side of the prominence, we can describe this roll to be either from positive polarity to negative polarity, or vice-versa. Accordingly, the roll is defined to be *positive* if its direction is same as that of the overlying field, and *negative* if its direction is opposite. Martin (2003) have regarded the phenomenon of roll effect as a dynamic form of chirality, i.e., the direction of the roll bears a one-to-one correspondence with the dextral and sinistral nature of filaments.

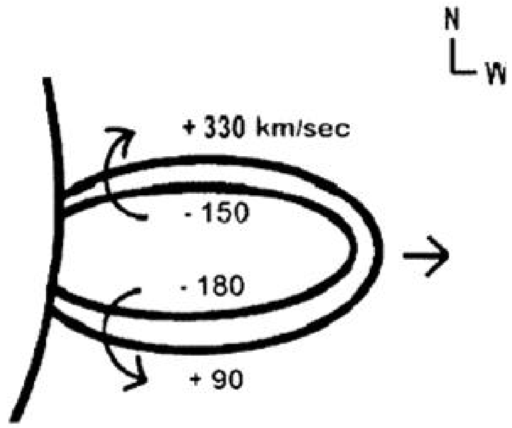

Figure 3.1 Doppler observations of an EP carried out from Mount Wilson Observatory by M. A. Ellison on 1947 June 11. The velocity values were determined from the amount of Doppler shifts on the inside and outside of each prominence leg.

A means to observe and quantify the roll effect is the Doppler measurements of EPs. Martin (2003) also cautions however, that unambiguous recognition of roll effect is possible only in those favourably oriented prominences in which one can identify with certainty as to which leg lies closer to the observer, and which lies farther away. Martin (2003) cites work by M. A. Ellison[1] titled *Eruptive Prominence of 1947 June 11 and Some Motion Forms of its Hα Line* based on observations

[1]Only the title and information about this work are available from Martin (2003). No other publication or record is known to exist.

of an EP from Mount Wilson Observatory. Ellison had observed opposite Doppler shifts on either side of each of the two prominence legs, as depicted in Figure 3.1. The inside of both legs showed a blue-shift, while the outside showed red-shift, indicating that the two legs experienced twists in opposite directions, which is a proxy for the roll effect. Martin has further listed a few more events where Doppler observations have revealed the sense of roll in the legs of prominences. Upon comparing this with the chirality of prominences, it was found that dextral prominences undergo a positive roll, and sinistral ones undergo a negative roll.

Bangert, Martin, and Berger (2003) have considered that the overlying coronal arcade plays a major role during this phenomenon. It is observed that the arcade is not exactly perpendicular to the filament spine, but skewed with respect to it (Martin and McAllister, 1995). The skew is defined as the acute angle between direction of the arcade and the filament axis. A filament is said to be *left-skewed* or *right-skewed* if, while looking at the filament in a direction perpendicular to its axis, the acute angle lies on the observer's left-hand or right-hand side. It was also reported by Martin (1998b) that left-skewed arcades overlie dextral filaments, while right-skewed arcades overlie sinistral filaments. According to the model by Bangert, Martin, and Berger (2003), as the filament starts to erupt, the overlying coronal arcade pushes the rising filament downwards. As a result, the top of the filament ribbon is deflected to one side, while the bottom keeps on rising, producing a roll at the top. The model also states, that it is the direction of the skew that decides the direction in which the filament top will be deflected. Thus, they observe that filaments with a positively skewed arcade will experience negative roll, and vice-versa.

3.1.2 Motivation

Most of the studies cited above use observations from a single viewpoint to study the dynamics of an EP. However, in this chapter, I will discuss results from the stereoscopic reconstruction (Chapter 2) applied to images from the twin STEREO spacecraft of two EPs that showed a highly twisted structure. The two phenomena discussed above, viz, helical motion and non-radial propagation, have separately been a subject of study by several researchers. This is the first time though that a combined study has been made of these two phenomena using three-dimensional reconstruction. Joshi and Srivastava (2007), using EIT 304 Å images from SoHO, have obtained the acceleration values of EPs in their slow-rise and fast-eruptive stage. In this study, we go a step forward, and show that the two phenomena of helical motion and non-radial propagation, determine the true acceleration of the prominences during their fast-eruptive stage. In the second part of the chapter, I will discuss another prominence that erupted on 2008 December 12, which was part of a study carried out with our collaborators. The prominence exhibited non-radial propagation during its eruption, and was observed to roll at the top, as inferred from its stereoscopic reconstruction study. Additionally, the CME associated with it also showed non-radial propagation, consistent with that of the EP.

3.2 Helically Erupting Prominences

Here, we focus mainly on two aspects of prominence eruptions, namely, the kinematics during the slow-rise and the fast-eruptive phases, and the helical twist of prominences during the fast-eruptive phase. By twist we mean the filament axis leaving its plane and forming a loop-like structure, such as seen in the TRACE images, e.g., Figure 1 of Török and Kliem (2005) and Figure 3 of Chifor *et al.* (2006).

3.2.1 Observations and Analysis

We have used 304 Å images from EUVI/STEREO to reconstruct the true shape of the prominences on 2010 April 13 and 2010 August 01. Both of these are high latitude northern hemisphere prominences which erupted over a period of a few hours. In spite of the large separation between the two spacecraft, (139° on 2010 April 13 and 149° on 2010 August 01), the elevated heights of the two prominences made the three-dimensional reconstruction possible. To identify a feature unambiguously in both the images, and then track it correctly in subsequent images, we have extensively relied upon time-lapse movies of the events. The movies guided us to safely neglect features that did not persist for the entire duration of the eruption, and consider only those that could be identified and tracked in all of the images. However, since both the prominences are located very close to the solar limb as seen from each spacecraft, even such a time-lapse movie is not enough to reveal the sense of twist in the prominence, making the reconstruction absolutely necessary. We not only had to track both the prominences for as long as possible, but also had to trace their shape. For this reason, several features along the prominence spines, that could be identified in images from the two spacecraft, were chosen.

2010 April 13 Prominence

This is a high-latitude northern polar crown prominence. Images from EUVI B (left column) and A (right column) at different instants of time are shown in Figure 3.2. We name the prominence leg on the right hand side in EUVI A image in Figure 3.2 as L1 and the one on the left (in EUVI A image) as L2. At 05:06 UT, we see that the prominence is oriented in such a direction, that leg L2 is not visible from EUVI B. In EUVI A however, the prominence appears almost side-on, giving us a complete view of its evolution. It should be emphasised at this point, that although EUVI A offers a complete view of the prominence spine, it is only in the side-on view of EUVI B that we clearly see the twisting spine late into the eruption. At 05:56 UT, L2 starts to show up in EUVI B images. Mass flows in L2 are observed during this time in both the images.

We chose five features along the leg L1 of this prominence to be reconstructed; numbered 1 to 5 from bottom of the leg up to the top of the spine. In addition, once leg L2 was visible in both the images, from 05:36 UT onwards, we identified

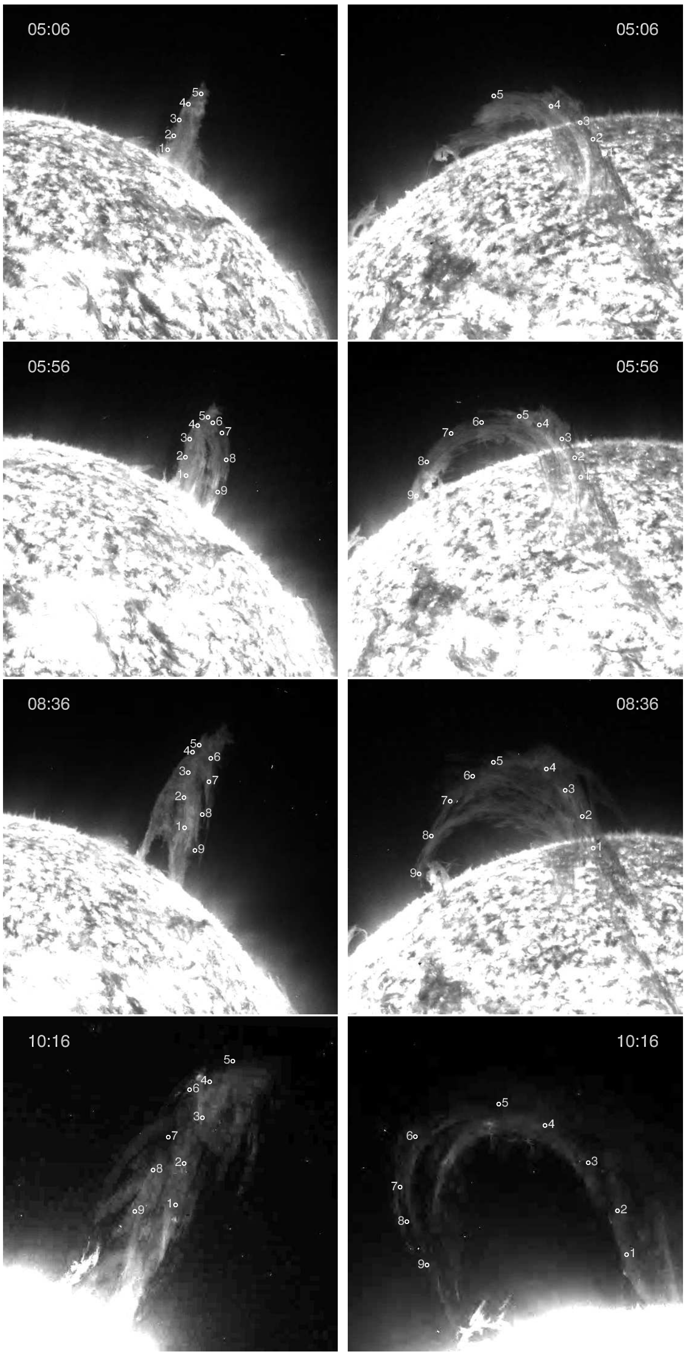

Figure 3.2 Erupting prominence on 2010 April 13 seen in 304 Å images from EUVI B (left) and A (right) on board the twin STEREO spacecraft. Observation times in UT are shown for each image. The features used for reconstruction are marked and numbered along the prominence. Leg L2 was visible in EUVI B only from 05:36 UT onwards, hence numbers 6 to 9 are not shown in the image at 05:06 UT.

four features along it; numbered 6 to 9 starting from top of the spine and reaching bottom of L2, and followed those too. The features are marked and numbered on the images in Figure 3.2. As the eruption progressed, the prominence became more twisted, and also grew fainter as it rose in height. The features selected for reconstruction were followed carefully until it was no longer possible to identify them unambiguously.

2010 August 01 Prominence

This too is a northern polar crown prominence. EUVI images in 304 Å of the prominence at different instants of time from EUVI B (left column) and A (right column) can be seen in Figure 3.3. We name the prominence leg seen on the right hand side in EUVI B image Figure 3.2 as L1, and the one on the left as L2. While the prominence is seen as a hedgerow in EUVI B image at 04:57 UT, we can see only its spine in the corresponding EUVI A image. At 07:27 UT, as the prominence starts to rise, we can see an arch in EUVI B image. Till this time, in EUVI A, the leg L2 of the prominence is not visible because the line-of-sight of the spacecraft is along the prominence spine. At around 08:16 UT, the rising prominence starts to twist, and L2 can be seen in EUVI A as well. Further, at 09:26 UT we can clearly see the twist in the prominence legs in 304 Å image from EUVI A.

Leg L1 of the prominence can be seen clearly in all the images from EUVI B and A, hence we chose five features along this leg for reconstruction, numbered 1 to 5 from bottom of the leg up to the top of the spine. Once the eruption starts and the prominence spine begins to twist, leg L2 becomes visible from 07:36 UT onwards. We consider four features along this leg for reconstruction, numbered 6 to 9 starting from top of the spine and reaching bottom of L2. This gives us a complete picture of the true shape of the prominence.

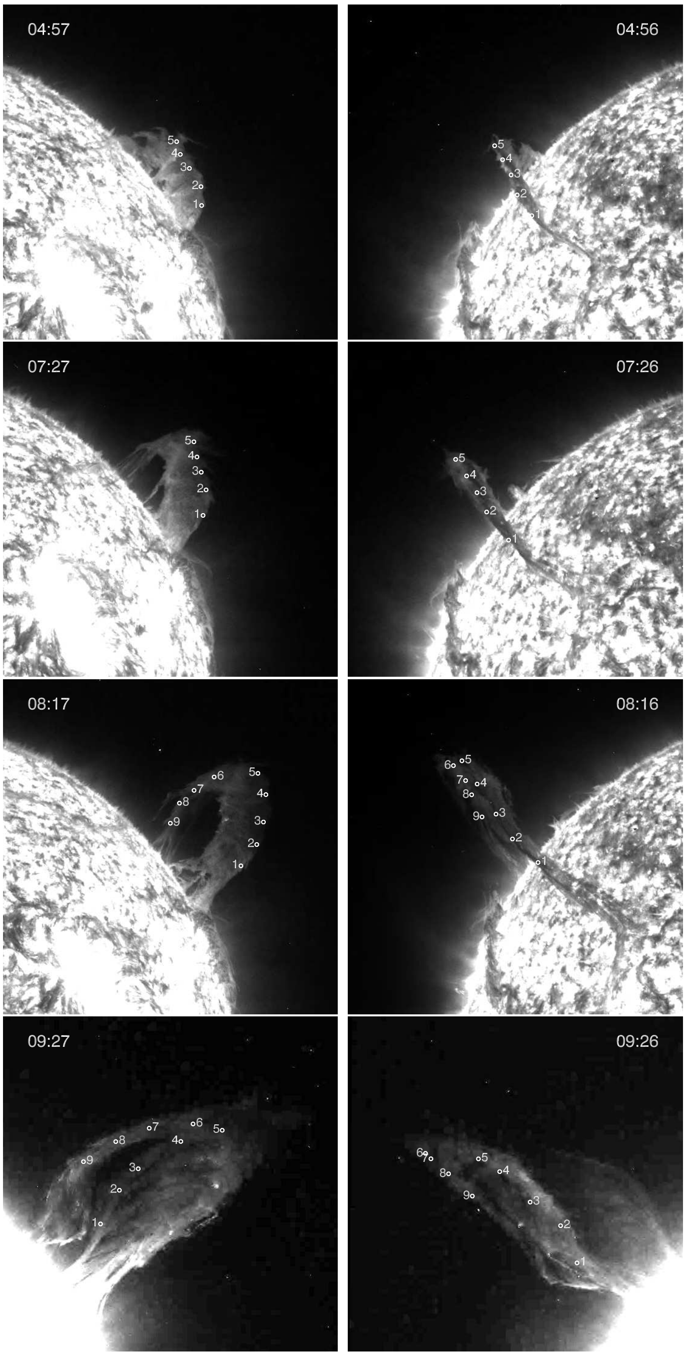

Figure 3.3 Erupting prominence on 2010 August 01 seen in 304 Å images from EUVI B (left) and A (right) on board the twin STEREO spacecraft. Observation times in UT are shown for each image. The features used for reconstruction are marked and numbered along the prominence. Leg L2 was visible in EUVI A only from 07:36 UT onwards, hence numbers 6 to 9 are not shown in the images at 04:56 UT and 07:26 UT.

3.2.2 Results and Discussion

2010 April 13 Prominence

This prominence is seen nearly side-on in 304 Å images from EUVI A, while the line-of-sight is along the spine for EUVI B. The prominence leg seen on the right in EUVI A image at 05:56 UT in Figure 3.2 is named L1, and the other is named as L2. We chose five features in L1 and four in L2 for reconstruction. Leg L2 which was obstructed from view by L1, became visible from 05:36 UT onwards. Hence, the four features along this leg could be observed only from this time onwards. We have employed two means through which the true shape of the prominence can be visualised. Figure 3.4 shows the prominence evolution in three dimensions in heliographic coordinates. All the points reconstructed for a given time are shown to be connected by straight lines. Since, cadence for the entire duration is constant at 10 minutes, we see from this figure that the prominence rises slowly for over five hours (several closely spaced lines) before erupting rapidly in two hours (widely-spaced lines). On the other hand, Figure 3.5 shows the variation with time of true height and the longitude and latitude in heliographic coordinates of each of the nine features. Features 1 to 5 belong to leg L1, while features 6 to 9 belong to leg L2.

From Figure 3.5, we can study in detail the evolution of the whole prominence structure. All the features are shown in different colours. In addition, to distinguish between features selected along the two legs, we have used different symbols. Triangles and asterisks are used for features in L1 and L2, respectively. Feature 1 is the lowest one in L1, as can be seen clearly in the plot for true height. As we move along L1 to the top of the spine, up to feature 5, the heights consistently increase throughout the time of the observations. From the time we start observing leg L2, feature 6 is the highest feature in it. The heights of features in L2 decrease as we go to the lowest one, which is feature 9.

The middle panel of Figure 3.5 shows that the longitudes of the features 1

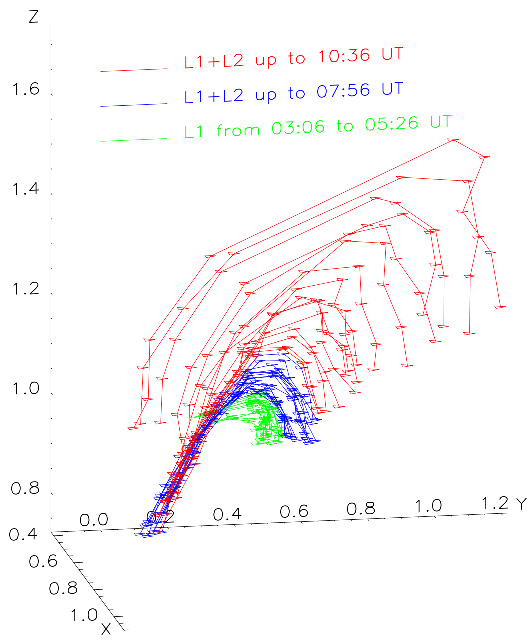

Figure 3.4 Evolution of the erupting prominence on 2010 April 13 as seen in the heliographic coordinate system. The position of the prominence determined by joining all the reconstructed points is shown at different instants of time, as marked on the plot. The coordinate system is centred on the Sun, with the Z axis along the solar rotation axis, and the X axis pointing towards the Earth. All the axes are in units of $R_\odot$.

to 5 in L1 are significantly higher ($\sim 20°$ to $60°$) than those in L2, features 6 to 9, ($\sim 0°$ to $30°$), *i.e.* leg L1 of the prominence is closer to the central meridian than leg L2. We can see that longitudes of all the features in L1 steadily increase throughout the period of observations, whereas longitudes of features in L2 remain almost constant before the eruption, but decrease appreciably once the eruption starts at 08:36 UT to reach an almost constant value of $\sim 0°$. The bottom panel of Figure 3.5 shows latitudes of the nine reconstructed features. Latitudes of features in leg L1 (triangles) are seen to decrease throughout the period of observations. Further we also observe that the decrease in latitude of the lowest feature, 1, in L1 is the maximum, from 55° to 43°. While the decrease for the highest feature, 5, is the least, from 55° to 50°. Contrary to leg L1, we find that latitudes of the two lowest features, 8 and 9, in leg L2 show an increase of a few degrees,

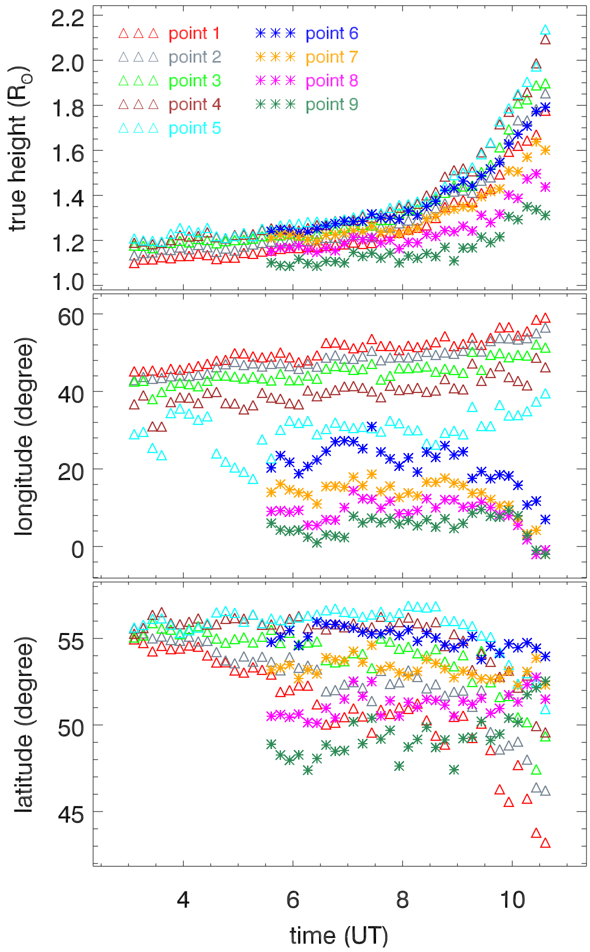

Figure 3.5 The heliographic coordinates of different features of the prominence on 2010 April 13. Features 1 to 5 are from leg L1 to the top of spine, while features 6 to 9 are from spine to the lowest feature in leg L2 of the prominence.

while latitudes of the two other features, 6 and 7, do not show significant change. Figure 3.6 shows a cartoon sketch of the prominence projected against the solar disc. Changes in latitudes of the reconstructed features are shown as vertical arrows, while the overall direction of twist in the prominence is shown as thick curved arrows. Length of the vertical arrows are roughly indicative of the change in latitude for each feature.

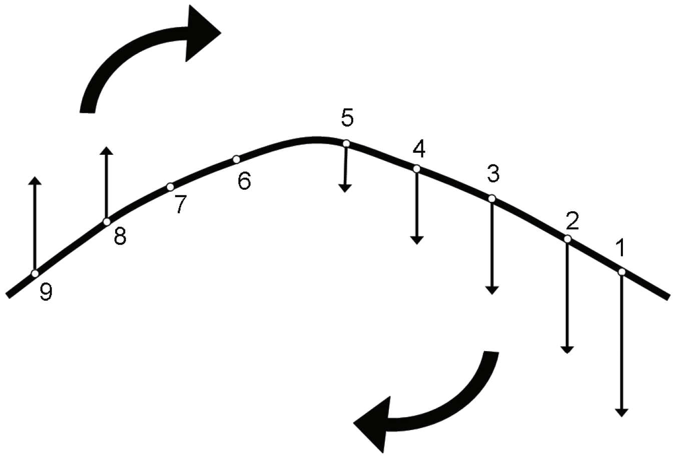

Figure 3.6 A cartoon sketch, showing the prominence on 2010 April 13 projected against the solar disc, where, longitude is along the horizontal and latitude is along the vertical. The long curved line is the prominence, on which features 1 to 9 are marked as circles. The changes in latitude are shown as straight arrows, and the large curved arrows show the direction of prominence rotation, indicating a clockwise helical twist in the prominence spine.

Earlier studies have shown that prominences tend to travel in a non-radial equatorward direction during their eruption (Filippov, Gopalswamy, and Lozhechkin, 2001). Our own analysis in Panasenco *et al.* (2011) shows such a deviation of prominences from their radial path in 3 events using stereoscopic reconstruction. Another dynamic form that a prominence exhibits during eruption is the writhe in its axis. Gilbert *et al.* (2001) have observed helical motion in prominences in He I 10830 Å images, while Gilbert, Alexander, and Liu (2007) have tried to explain this motion by the means of a kinking filament. We propose that the prominence motion described in our study is due to superposition of these two separate motions. The first motion is the overall non-radial direction of propagation of the prominence, which directs the entire prominence towards the solar equator. While, the second motion is the helical twisting motion of the prominence spine. Leg L1 is at higher longitude than L2, hence L1 can be regarded as the western leg. Since changes in latitudes of features in L1 are quite large, as shown above, we infer that the twisting motion and non-radial motion are acting in the same direction for this leg (Figure 3.6). On the other hand, for leg L2, which is at a lower longitude than L1, the changes in longitudes are small as compared to L1, hence we can say that the twisting motion and non-radial motion are acting in opposite directions for this leg. Therefore, the western leg, L1, shows a decrease in its latitude, while the eastern leg, L2, would have shown an increase in its latitude, but it is overpowered by the overall non-radial motion of the prominence. Thus we deduce that as the prominence erupts, its spine is seen to twist in a clockwise direction.

2010 August 01 Prominence

With respect to orientation relative to the two STEREO spacecraft (Figures 3.2 and 3.3), the two prominences in this study are mutually opposite. The prominence of 2010 August 01 initially appears like a hedgerow in 304 Å images from EUVI B, but only its spine is visible from EUVI A. The prominence leg seen on the right in EUVI B at 08:17 UT in Figure 3.3 is named L1, and the other leg is named as L2. For getting its shape in three dimensions, we chose five features in leg L1 of the prominence. Leg L2 was obstructed from view by L1 for most of the time, and it became visible late into the eruption, from 07:36 UT onwards. Four more features along this leg were selected for reconstruction. As before, Figure 3.7 shows the prominence evolution in three dimensions in heliographic coordinates, and Figure 3.8 shows the true height along with the longitude and latitude of each of the nine features at different instants of time. Similar to Figure 3.4, the numerous closely spaced lines in Figure 3.7 too indicate a slow rise for about six hours, before a rapid eruption lasting around 2.5 hours. In Figure 3.8, features 1 to 5 belong to L1, while features 6 to 9 belong to L2.

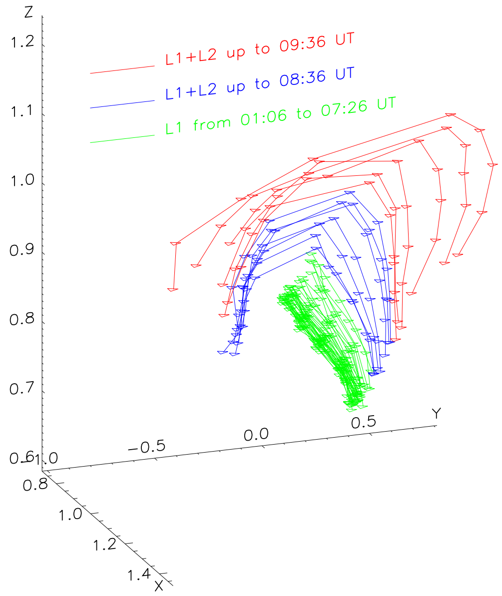

Figure 3.7 Evolution of the erupting prominence on 2010 August 01 as seen in the heliographic coordinate system. The position of the prominence determined by joining all the reconstructed points is shown at different instants of time, as marked on the plot. The coordinate system is centred on the Sun, with the Z axis along the solar rotation axis, and the X axis pointing towards the Earth. All the axes are in units of $R_\odot$.

The top panel in Figure 3.8 gives true height of all features stereoscopically reconstructed in the prominence on 2010 August 01. The spread in heights of the features for this prominence is small compared to the spread seen for 2010 April 13 prominence. However, we still see that the height increases from the lowest feature, 1, to the highest feature, 5, in L1, and then decreases from the highest feature, 6, to the lowest one, 9, in the L2, consistently throughout the observation period.

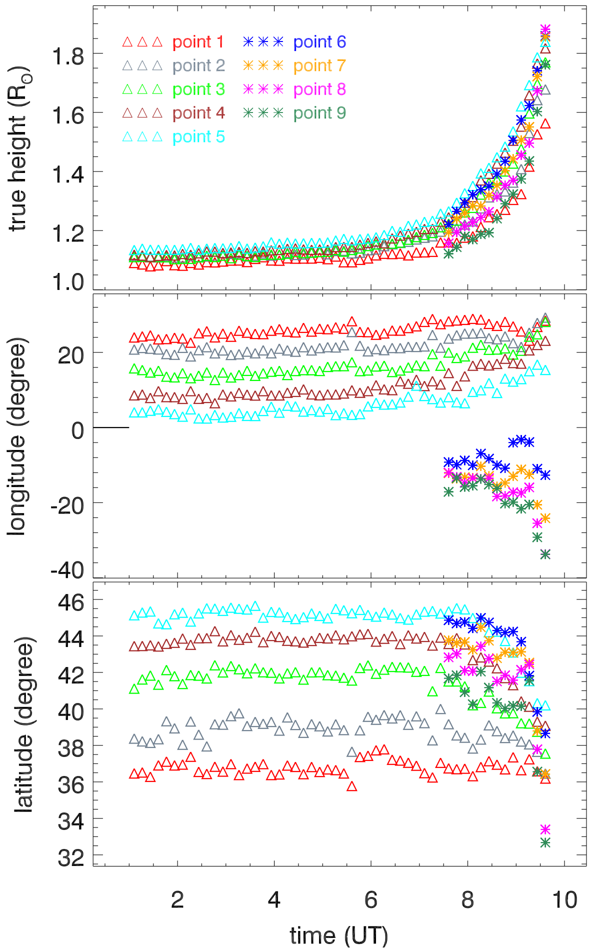

Figure 3.8 The heliographic coordinates of different features of the prominence on 2010 August 01. Features 1 to 5 are from L1 to the top of spine, while features 6 to 9 are from spine to the lowest feature in leg L2 of the prominence.

The latitudes and longitudes of the reconstructed features do not show as large a change as for those along the 2010 April 13 prominence. As we go from the lowest feature, 1, in L1 through the spine to the lowest feature, 9, in L2, we see that the longitude decreases more or less uniformly. Both longitude and latitude values for features in L1 remain almost constant prior to the eruption. However, once the eruption starts at 07:06 UT, features 3, 4 and 5, which lie close to the spine show an increase in longitude of about 10° each, while the two lower features, 1 and 2, do not show any change in longitude. Leg L2 could be observed only once the eruption starts. With the exception of feature 6, longitudes of features 7, 8 and 9 are seen to decrease during the eruption. While features 7 and 8 decrease in longitude by the same amount of $\sim 10°$, the decrease in the lowermost feature in L2 is 15°. The latitudes of all the features except 1 and 2, are seen to decrease roughly by 6°.

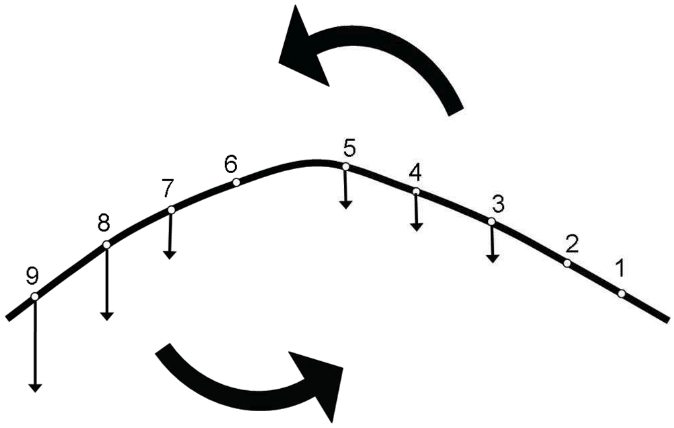

Figure 3.9 A cartoon sketch, showing a top-down view of the prominence on 2010 August 01, where, longitude is along the horizontal and latitude is along the vertical. The long dark line is the prominence, while features 1 to 9 are marked as circles. The changes in latitude are shown as straight arrows, and the large curved arrows show the rotation direction of the prominence legs. This indicates an anticlockwise twist in the prominence spine.

An argument similar to the 2010 April 13 event about the two separate motions experienced by the prominence can be extended towards this event too. Leg L1 is at higher longitude that L2, hence L1 can be termed as the western leg, and L2 as the eastern leg. As explained above, features 1 and 2 do not show much change either in their latitudes or longitudes. Features 3, 4 and 5 in the western leg however, show a small decrease in latitude, and a small increase in longitude. While, features in the eastern leg (L2) show a significant change in both latitude and longitude. In this case, we find that it is the eastern leg that experiences a stronger decrease in latitude compared to the western leg, because of the opposing motions of twist and non-radial equatorward direction of propagation of the prominence during its eruption. Hence, we can infer that the prominence on 2010 August 01 showed a twist in its axis in the anticlockwise direction. The prominence projected against the solar disc is shown in the form of a cartoon sketch in Figure 3.9. Changes in latitudes of the reconstructed features are shown as vertical arrows, while the overall direction of twist in the prominence is shown as thick curved arrows. Length of the vertical arrows are roughly indicative of the change in latitude for each feature.

3.2.3 Acceleration of the Prominences

Studies have found that a prominence is observed to display two phases during their eruption, the slow rise and the fast eruption. Sterling and Moore (2005) have found a slow rise phase with a constant velocity, and then an accelerating fast eruptive phase. On the other hand Joshi and Srivastava (2007) have reported a small acceleration of about $4 - 12\,\mathrm{cm\,s^{-2}}$ even in the slow rise phase, while Sterling and Moore (2004a; 2004b) have found the prominence to rise with constant velocities of the order of $1 - 100\,\mathrm{km\,s^{-1}}$ during both the phases. It must be noted that these conclusions were based on observations from a single viewpoint. For the two prominences studied here, we identified a time of eruption after which the true height increased very rapidly. A 2^{nd} order polynomial was fitted separately to the prominence height before and after the time of eruption. The fitted function was used to obtain the true speed and acceleration of all the features of the prominences.

The slow rise phase

The two prominences analysed by us exhibit slow rise followed by a fast eruption. From Figure 3.8 top panel, we see that the prominence on 2010 April 13 increased in height over a period of almost five hours before its eventual eruption which commenced at 08:36 UT. The features in leg L1 show an almost uniform motion during this phase, rising with an average acceleration of $67\,\mathrm{cm\,s^{-2}}$. However, features in L2 showed a wide range of acceleration, ranging from $-46\,\mathrm{cm\,s^{-2}}$ for feature 9 to

$123\,\mathrm{cm\,s^{-2}}$ for feature 7. We believe that the large spread in acceleration values for leg L2 is because of the lesser number of points available in the slow rise phase for fitting a 2nd order polynomial.

A similar procedure was employed to obtain true acceleration of the features for 2010 August 01 prominence. The eruption for this event was found to begin at 07:06 UT. We once again find an almost constant acceleration in leg L1; its average value being $31\,\mathrm{cm\,s^{-2}}$ for features 2 to 5. Feature 1, however, showed a relatively low acceleration at $4\,\mathrm{cm\,s^{-2}}$. Since leg L2 could be observed only once the eruption started, it was not possible to observe the slow rise in this leg prior to the eruption.

The values for constant acceleration of the features during the slow rise of prominences obtained here are considerably higher than those obtained by Joshi and Srivastava (2007) which were in the range $4 - 12\,\mathrm{cm\,s^{-2}}$.

The fast eruptive phase

On fitting the true heights of all the features in the eruptive phase for both the prominences with a polynomial function, it was found that they rose with a constant acceleration. For the 2010 April 13 prominence, each of the five features in leg L1 showed a constant value of acceleration ranging from $9 - 12\,\mathrm{m\,s^{-2}}$, with an average value of $11\,\mathrm{m\,s^{-2}}$. Whereas, the four features in leg L2 showed acceleration in the range $2 - 8\,\mathrm{m\,s^{-2}}$, with an average value of $5\,\mathrm{m\,s^{-2}}$. The significant difference between values of average acceleration in the two legs during the eruptive phase can be attributed to the two forces acting on the prominences. This prominence is shown to twist in clockwise direction, which means that in the western leg, L1, the two forces, viz, helical twist and non-radial motion, are acting in the same direction, but they are acting in opposite directions on the eastern leg, L2. Therefore, L1 shows a higher value of average acceleration in the eruptive phase, whereas, L2 shows a relatively lower value of average acceleration.

For the 2010 August 01 prominence too, a constant acceleration for each reconstructed feature was derived. For the five features in L1, the values range from $9 - 11\,\mathrm{m\,s^{-2}}$, with an average value of $10\,\mathrm{m\,s^{-2}}$, while for the four features in L2 had their acceleration values ranging from $16 - 23\,\mathrm{m\,s^{-2}}$ with an average of $20\,\mathrm{m\,s^{-2}}$. A very similar argument as put forward above can be used to explain the markedly distinct values of average acceleration observed in the two legs of this prominence as well. As shown earlier, this prominence twists in the anticlockwise direction during eruption. Thus, in the eastern leg, L2, the twisting motion and the non-radial propagation act in the same direction giving rise to a higher acceleration, compared to the western leg, L1, wherein these two motions act in mutually opposite directions.

We find that the values for constant acceleration of the features during the fast eruptive phase of prominences are slightly lower than the maximum acceleration in the range of $3 - 77\,\mathrm{m\,s^{-2}}$ obtained by Joshi and Srivastava (2007), but an order of magnitude lower than the value found by Sterling and Moore (2005), which is $1.0\,\mathrm{km\,s^{-2}}$. This may be due to the fact that the prominences analysed by Joshi and Srivastava (2007) and the two prominences in the present study are quiescent in nature, whereas those analysed by Sterling and Moore (2005) are active region prominences.

3.3 Non-Radial Motion of EP and CME

We have analysed an EP and the associated CME on 2008 December 12. The prominence was a large northern hemisphere polar crown prominence that showed a rolling motion, as described in Martin (2003), in addition to non-radial motion inferred from the reconstructed coordinates. EUVI 304 Å images of the EP from STEREO B and A are shown in Figure 3.10.

3.3.1 Rolling Motion in EPs

This work has been carried out in collaboration with researchers from Helio Research, namely, Olga Panasenco and Sara F. Martin, and is published as Panasenco

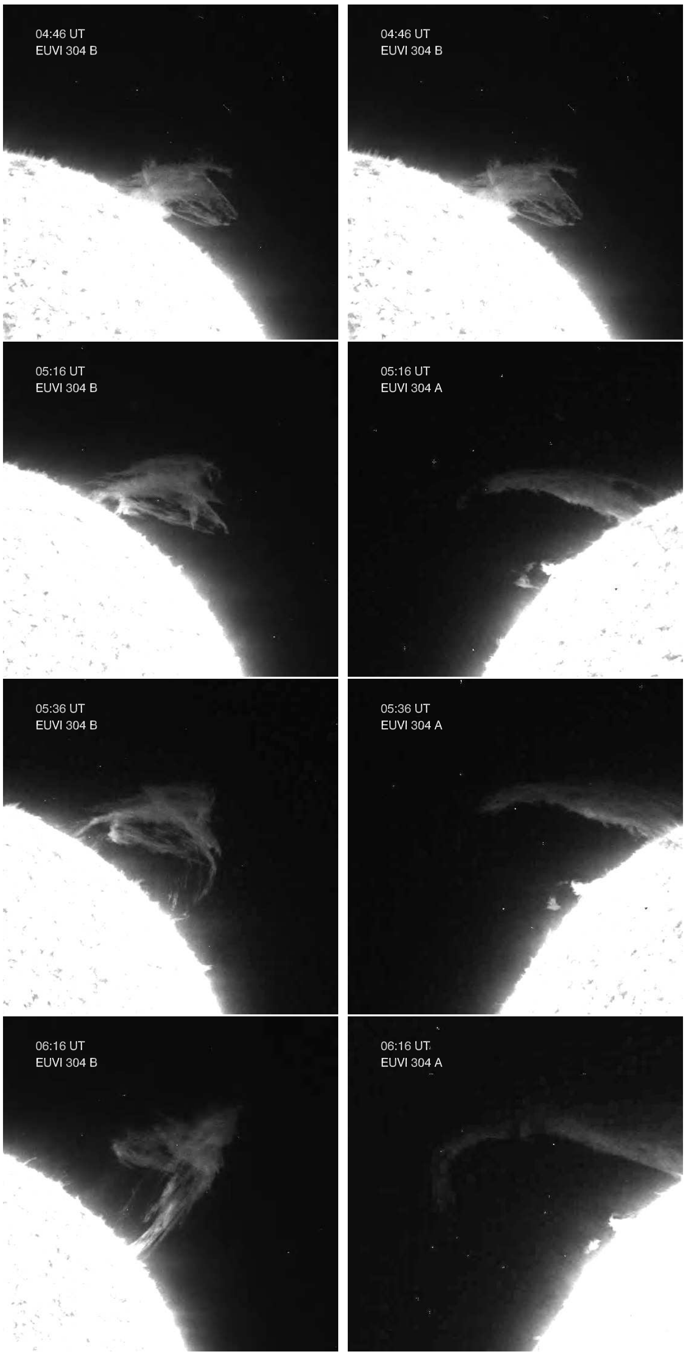

Figure 3.10 Erupting prominence on 2008 December 12 seen in 304 Å images from EUVI B (left) and A (right) on board the twin STEREO spacecraft. Observation times in UT are shown for each image.

et al. (2011). I have discussed the dynamic phenomenon of roll effect in § 3.1.1. It should be emphasised that not all the prominences display this phenomenon

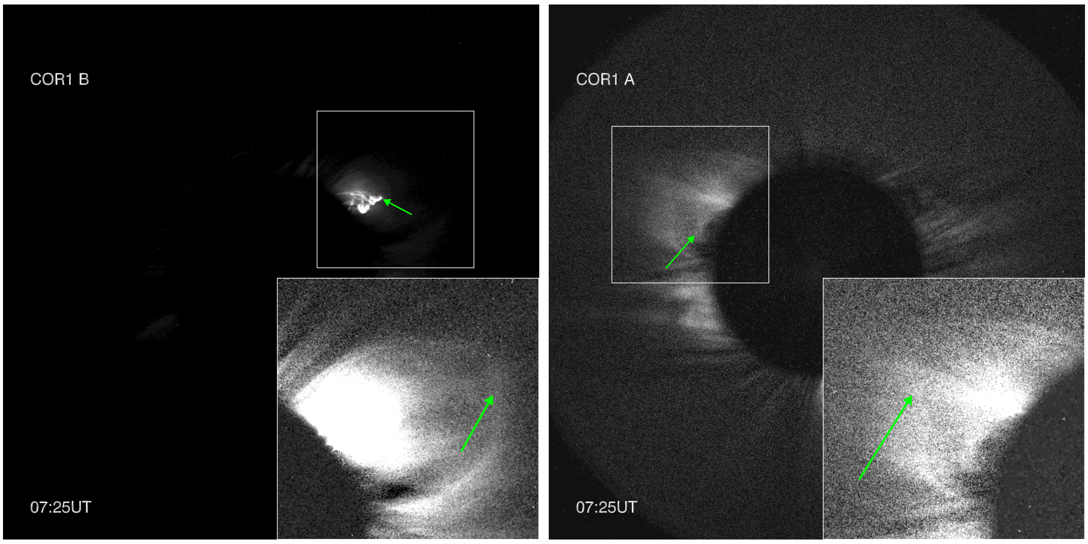

Figure 3.11 Erupting prominence on 2008 December 12 seen in images from COR1 B (left) and A (right) on board the twin STEREO spacecraft. Observation times in UT are shown for each image. The features in the prominence and CME LE used for reconstruction are marked.

during their eruption, and even then, the observations could be marred by an unfavourable orientation of the prominence with respect to the observer. Of the three events studied in the paper Panasenco *et al.* (2011), I will present here the prominence on 2008 December 12 that was observed to roll at the top during its eruptive stage. Images of the prominence during its eruption are shown in Figure 3.10. There was also a CME associated with this prominence. Since the EP and the associated CME could be observed very well by both the STEREO spacecraft, its stereoscopic reconstruction was carried out using the IDL^{TM} routine `scc_measure` (Thompson, 2009). Individual features in the prominence mass and the CME LE were selected and tracked in several pairs of images of EUVI 304 Å and COR1. From the top to bottom panels in Figure 3.12 the true height and heliographic longitude and latitude of the selected feature obtained from the stereoscopic reconstruction are shown. The left and middle panels show results of the EP as seen in EUVI 304 Å images and the coronagraphs COR1 and COR2, respectively. The right panels show the coordinates of CME LE as seen in COR1 and COR2. The speeds shown in the top panel are obtained from a linear fit to the eruptive stage of the corresponding feature.

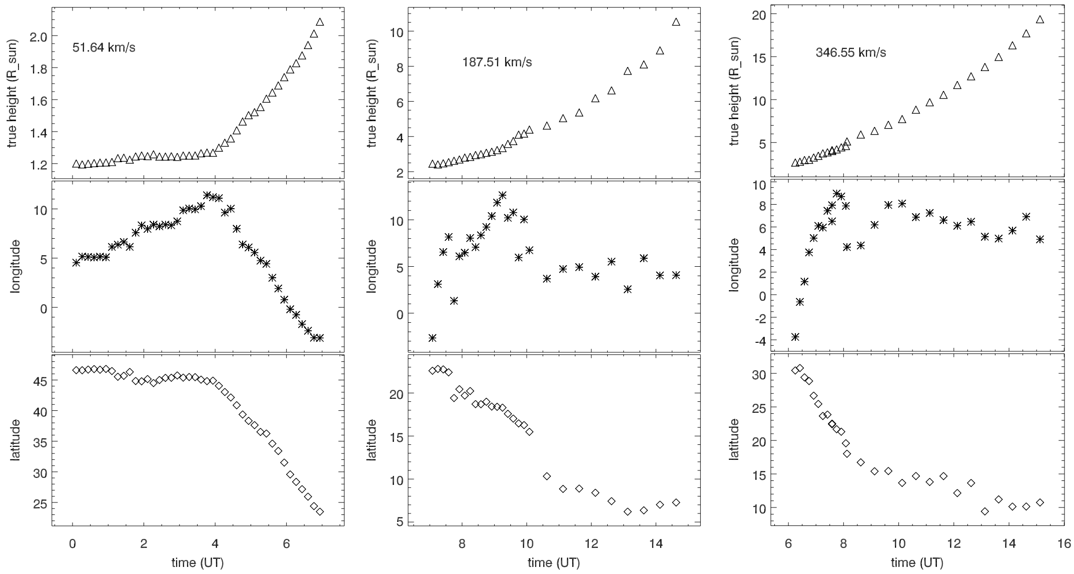

Figure 3.12 Results from stereoscopic reconstruction applied to a feature in the EP and in the associated CME LE. The true heliographic coordinates of EP seen in EUVI 304 Å images (*left panel*), EP as seen in coronagraphs COR1 and COR2 (*middle panel*), and those of CME LE as seen in COR1 and COR2 (*right panel*). The speeds shown in the top panel are obtained from a linear fit to the eruptive stage of the corresponding feature.

From Figure 3.12, we find that the prominence undergoes a slow rise before the eruption for about two hours. During this time, its latitude remains at a constant value of $\sim 45°$, but its longitude increases significantly from 5° to 12°. However, once the eruption starts, both the latitude and longitude start to decrease. When the prominence is further tracked in COR1 and COR2 FOVs, newer dynamics are revealed owing to the 3D reconstruction. As the prominence starts to erupt we observe that its longitude decreases as can be seen from the left panel of Figure 3.12. However, once the prominence enters the COR1 FOV, its longitude increases and then decreases in the COR2 FOV. The latitude on the other hand continues to decrease throughout the FOV of both the coronagraphs, from 45° during the slow rise phase to $\sim 5°$ at the end of COR2 observations. This implies that the feature selected shows a monotonic equatorward non-radial motion. However, the selected prominence feature appears to sway longitudinally, with its value varying from $5°$ to $10°$ to $-4°$ in the EUVI FOV, and then increasing up to $10°$ and decreasing a little to attain an almost constant value of $5°$ in FOV of the two coronagraphs. The behaviour of CME LE is very much similar to that of the EP in the coronagraphs FOV. The latitude of CME decreases from around $30°$ to reach a constant value of $10°$, while its longitude changes to a constant value of $\sim 8°$ after an increase from almost $-4°$.

In a statistical study of CMEs observed from LASCO/SoHO, Cremades and Bothmer (2004) have reported CMEs to deviate towards the equator because of the high-speed solar wind coming from polar coronal holes. Similarly, Gopalswamy *et al.* (2009) have considered a coronal hole adjacent to the source region of a CME responsible for a *driverless* shock observed at the Earth, i.e., a shock without an accompanying CME or magnetic cloud. The non-radial motion that we observe in the prominence and the associated CME on 2008 December 12 is consistent with both these conclusions.

However, in addition to the non-radial motion, we also observe the prominence sway longitudinally. Since, the feature tracked lies at the top of the EP, this motion can be considered to be sideways roll of the prominence top (Panasenco *et al.*, 2011). It is proposed that two levels of deflecting forces are present with different time-scales. First is the local magnetic force imbalance due to a coronal hole near the filament channel. This force is mainly responsible for the rolling motion observed in the EP. The second force is the global magnetic force imbalance, which causes the CME to travel in a non-radial direction.

In the first part of this chapter, I have presented results from a stereoscopic study two EPs on 2010 April 13 and 2010 August 01. These prominences displayed two phases of eruption, the slow-rise phase and the fast-eruptive phase, with a constant value of acceleration for both the events in both the phases. The stereoscopic reconstruction revealed that the prominences showed a helically twisted spine, and non-radial motion during the fast-eruptive phase. The acceleration in the legs of the prominences during their fast-eruptive stage was found to be commensurate with the sense of helical twist and the non-radial direction. Thus, for the first time it is shown that a prominence can experience different acceleration in its two legs, and these two motions together can explain this difference. We also studied the eruptive prominence on 2008 December 12, which was part of a study carried out with our collaborators Olga Panasenco and Sara F. Martin. The prominence was seen to roll at the top, which was confirmed by the results obtained on reconstructing a feature in the EP observed in EUVI 304 Å images.

Chapter 4

Acceleration of CMEs and associated EPs

4.1 Introduction

Coronal Mass Ejections (CMEs) are transient events where mass from the Sun is expelled out into the interplanetary (IP) space. Hansen *et al.* (1974) from the ground based K-coronameter, and Gosling *et al.* (1974) from the coronagraph on board the Skylab spacecraft were among the earliest observers of CMEs. In the early days of its discovery, CMEs were also labelled as coronal depletions or coronal transients. In § 1.3, we have discussed in brief about the CMEs and their association with EPs. This section first elaborates on the same topic, and later objectives of the study carried out are outlined in brief.

A CME can be identified as a three-part structure comprising of a bright outer *rim*, followed by a dark cavity surrounding a bright central core (Illing and Hundhausen, 1985, 1986). However, prior to this conclusion about the broader structure of a CME, Tandberg-Hanssen (1974) and Fisher and Poland (1981) had suggested that a complex knot of twisted fields observed underneath the bright rim is the prominence, while Low, Munro, and Fisher (1982) had proposed that the dark cavity just below the rim is nothing but the dark region often found surrounding a prominence. Previously a CME was assumed to have a two-dimensional loop-like structure. However, it later became clear that the CME is more like a three-dimensional bubble (Howard *et al.*, 1982), which is visible due to the Thomson-scattering of photospheric light by the electrons in the CME. Since, the outermost part of the bubble has a high concentration of electrons along the line of sight (LOS), it is this LOS-integrated light that we see as the bright outer *rim* or *loop*. We now refer to this outer rim as the leading edge (LE) of the CME.

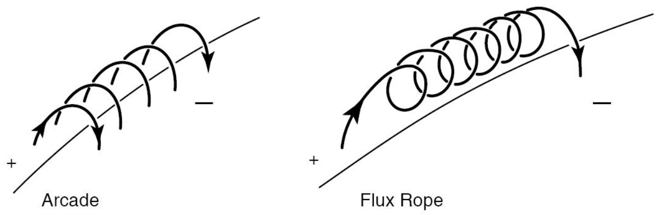

Figure 4.1 The magnetic field configuration before a CME erupts can be either of an arcade type (left) or of a flux rope type (right) (Klimchuk, 2001). The number of turns in the flux-rope type configuration is highly exaggerated.

The coronal magnetic field before a CME erupts is in equilibrium, and can be of two types: *arcade* or *flux-rope*, as shown in Figure 4.1. However, the magnetic configuration of a propagating CME is believed to be a helical flux-rope (Chen *et al.*, 1997; Dere *et al.*, 1999). When the equilibrium is lost owing to factors such as flux emergence, flux cancellation, reconnection, shear, etc. (Chen and Shibata, 2000; Forbes *et al.*, 2006; Seaton *et al.*, 2011), a CME occurs. Once the equilibrium is lost, the energy needed for its propagation, and often acceleration is derived from the surrounding magnetic field (Forbes, 2000; Low, 2001; Alexander, 2006). Priest (1988) proposed that it is the coronal streamer overlying a filament that first undergoes the loss of equilibrium which initiates a CME, which is followed by the eruption of the filament. On the other hand, Browning and Priest (1986) have stated that it is the filament which slowly rises and stretches the overlying field lines, which causes a flare, and also may be responsible for a CME. Both these opposite viewpoints were unified by Low (1996), where he regarded different phenomena associated with a CME as a response to the "cyclical injection of fresh magnetic flux".

Several authors have attempted to explain the eruption of a CME through theoretical models, which can be divided into two main classes: *directly driven* and *storage and release* (Klimchuk, 2001). In the first class, energy is imparted in an impulsive manner to the CME, much like the explosion of a bomb. Examples of this type are thermal blast (Dryer, 1982; Wu, 1982), and dynamo (Klimchuk, 1990). In the second class of CME models, energy is slowly built up, until a trigger releases the stored energy to propel a CME. Wolfson and Saran (1998) proposed such a model, named as the mass loading type, wherein, the prominence mass was shown to provide the strain necessary to store energy in magnetic fields (Fong, Low, and Fan, 2002). However, the two models that have gained currency in the past few years are breakout or tether straining model (Antiochos, Dahlburg, and Klimchuk, 1994; Antiochos, DeVore, and Klimchuk, 1999), and the catastrophe or tether release or tether cutting model (Forbes and Isenberg, 1991; Isenberg, Forbes, and Demoulin, 1993). It cannot be claimed with certainty as to which model is the correct description of a CME, as Schrijver *et al.* (2008) and Lin, Gallagher, and Raftery (2010) have showed that different models may have to be applied for explanation of different observed physical and kinematic properties of CMEs.

Determining the speed with which a CME moves through the IP medium is of great interest because of the geomagnetic effects it can lead to. The charged particles in a fast CME would hit the Earth sooner, and may lead to a geomagnetic storm (Gopalswamy *et al.*, 2001). A slow CME can have a speed of about $100\,\mathrm{km\,s^{-1}}$, while the fastest CME can have a speed of $\sim 3000\,\mathrm{km\,s^{-1}}$ (Gopalswamy *et al.*, 2005). It is observed that as a CME travels through the IP medium to reach a distance of 1 AU, it experiences a change in its speed. Gopalswamy *et al.* (2000b) have found that although the initial CME speeds range from $124 - 1056\,\mathrm{km\,s^{-1}}$, the speeds of the corresponding IP ejecta are found to lie in the range of $320 - 650\,\mathrm{km\,s^{-1}}$, *i.e.* the slow CMEs accelerate, and the fast ones decelerate. Cargill (2004) too has reported that speeds of interplanetary CMEs (ICMEs) corresponding to CMEs with speeds ranging from $100 - 2000\,\mathrm{km\,s^{-1}}$, as measured from coronagraphs, lie within $100 - 200\,\mathrm{km\,s^{-1}}$ of the ambient solar wind.

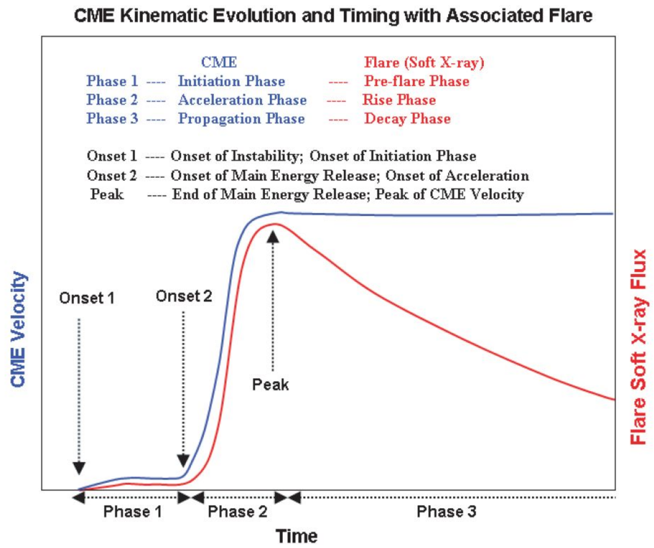

Figure 4.2 A schematic plot of kinematic evolution of a typical CME comprised of three phases: initiation, acceleration, and propagation. (Adopted from Zhang and Dere (2006)). The temporal relation of the CME speed (blue line) is also shown as a function the soft X-ray flux of the associated flare (red line).

The kinematic evolution of CMEs can be understood by taking into account the forces acting on it during its propagation, viz Lorentz force, viscous drag and gravity (Vršnak, 2001a; Cargill, 2004). Of these three forces, viscous drag is the most dominant force beyond a few solar radii (Vršnak, 2001b; Vršnak and Gopalswamy, 2002), and the other two can be neglected. Indeed, Vršnak *et al.* (2010) have used a numerical model to show that the ambient solar wind decides the eventual speed of a CME near the Earth. However, there are some CMEs, which are reported to have reached the Earth in less than 24 hours. This indicates that such CMEs are fast and extremely energetic, for which the velocity close to the Sun decides their arrival time at the Earth.

In order to fully determine the propagation mechanism of a CME, it is also essential to understand its launching mechanism. Based on an earlier study involving three events observed from SoHO/LASCO by Zhang *et al.* (2004); Zhang and Dere (2006) carried out a statistical study of 50 CMEs to study their evolution. They have regarded the CME evolution as a three-phase process involving initiation, acceleration and propagation (Figure 4.2). The initiation phase is marked by slowly rising coronal streamers, which is followed by a rapid increase in velocity in the main acceleration phase. In the propagation phase, CME acceleration is zero. In another study, Zhang *et al.* (2001) also have shown that soft X-ray flux of the associated flare and the CME velocity are related quantities. According to their study, the peak of the X-ray flux coincides with the time of maximum velocity of the CME, shown schematically in Figure 4.2.

Chen and Krall (2003) in their study of three CMEs conducted using SoHO/LASCO observations, have proposed that CME acceleration occurs in two phases, the *main* phase and the *residual* phase. While most of the acceleration occurs in the main phase, just like in Figure 4.2, there lies a second phase of acceleration known as the residual acceleration in the outer corona. They have employed a magnetic flux rope model (Chen, 1989) to establish a relation between the height at which the main acceleration phase peaks, and footpoint separation of the CME flux rope. In their model, Chen and Krall (2003) have proposed that a change in duration of the flux injection (Krall, Chen, and Santoro, 2000) determines the strength of the residual acceleration phase.

CMEs are either associated with flares, *i.e.* ARs, which carry high magnetic field, or prominences, which involve smaller magnetic fields. Although, there also have been instances where a CME was observed without any source region observed on the solar photosphere (Sheeley *et al.*, 1980; Fisher and Poland, 1981). Accordingly, the CME speeds have been classified on the basis of their source regions. Gosling *et al.* (1976), using the coronagraph on Skylab spacecraft, were the first ones to report that CMEs associated with flares are faster than those associated with prominences. This was supported by analysis of CMEs observed from the K-coronameter at MLSO by MacQueen and Fisher (1983), who also observed that the former type showed lower acceleration with increase in height than the latter. Sheeley *et al.* (1999) have also reported a similar result based on their technique to track features observed in SoHO/LASCO coronagraphs. Moon *et al.* (2002) in a statistical study involving over 3200 CMEs observed from SoHO/LASCO have reported that flare-associated CMEs have a higher median speed than those associated with EPs. They also found that although the median acceleration of all the events is zero, it decreases slightly with speeds if only those CMEs with speeds greater than $500\,\mathrm{km\,s^{-1}}$ are considered. Srivastava *et al.* (1999; 2000) have found that gradual CMEs attain the speed of the ambient solar wind at about $20\,\mathrm{R}_\odot$ from the Sun. Consistent with this study, Gopalswamy *et al.* (2001) have reported deceleration as high as $-100\,\mathrm{m\,s^{-2}}$ for fast CMEs (speed $> 900\,\mathrm{km\,s^{-1}}$) from a combined study of SoHO/LASCO and radio observations from the Waves instrument on Wind spacecraft.

We have learnt that CMEs exhibit a bimodal acceleration profile, consisting of the main phase and the residual phase. We also know that CME speeds are classified depending on whether the source region is a flare or a filament. Typically, flare-associated CMEs are found to be faster that filament-associated ones. It should be noted that most of these studies are carried out using observations from a single viewpoint, which inherently suffer from projection effects, leading to an underestimation of the height. In this chapter, we carry out a study of a few CMEs, some of which were associated with EPs, while the others were not. By applying a stereoscopic reconstruction technique, we determine the true evolution characteristics of the CMEs and the associated prominences.

4.2 Analysis of Observations

We have analysed six CMEs that were observed from the COR1 and COR2 coronagraphs aboard the twin STEREO spacecraft, that occurred on 2007 November 16, 2007 December 31, 2008 April 09, 2009 December 16, 2010 April 13, and 2010

August 01. A feature that could be identified in the CME LE in both COR1 and COR2 images was selected. Such a feature in most cases was located not in the outermost part of the CME LE, as it was difficult to track such a feature, but was located in central part of the LE. Three of the CMEs on 2008 April 09, 2010 April 13, and 2010 August 01 were associated with EPs. In order to make a comparative study of the kinematics of a CME and the associated EP, the three EPs were studied using 304 Å images from EUVI. A feature that could be identified unambiguously in the EP was selected for this purpose too. The EPs on 2010 April 13 and 2010 August 01 have been studied in Chapter 3 for the helical twist in their spines, and the kinematics during their eruptions (Joshi and Srivastava, 2011a). A brief description of each event is given below.

2007 November 16 CME This was a faint and slow CME seen on the south-west limb of the Sun from both the STEREO spacecraft (Figure 4.3). The CME first appeared in the COR1 A field of view (FOV) at 07:25 UT, and in COR1 B FOV at 08:15 UT. The CME entered the COR2 A FOV at 10:37 UT, and in the COR2 B FOV two hours later at 12:37 UT. EUVI A 304 Å images show a surge eruption on the far-side of the Sun. The surge eruption commenced at 06:26 UT, and could be observed up to 09:46 UT.

2007 December 31 CME This was a bright CME with a well-defined symmetrical LE on the south-east limb of the Sun, as seen in Figure 4.4. The CME was associated with a C8 flare which originated in NOAA AR 10980. The CME appeared in the COR1 B FOV at 00:55 UT, and at 01:00 UT in COR1 A FOV. The CME crossed the COR1 FOV in about one hour, indicating that it was a relatively fast CME, and appeared in the COR2 FOV at 01:37 UT in the two spacecraft. This CME showed an unusual cusp in its LE, which was distinctly visible in the COR2 images. We have used this feature for the purpose of three-dimensional reconstruction. On the eastern limb of the 304 Å image obtained from EUVI B, a flare can be seen at 00:46 UT, followed

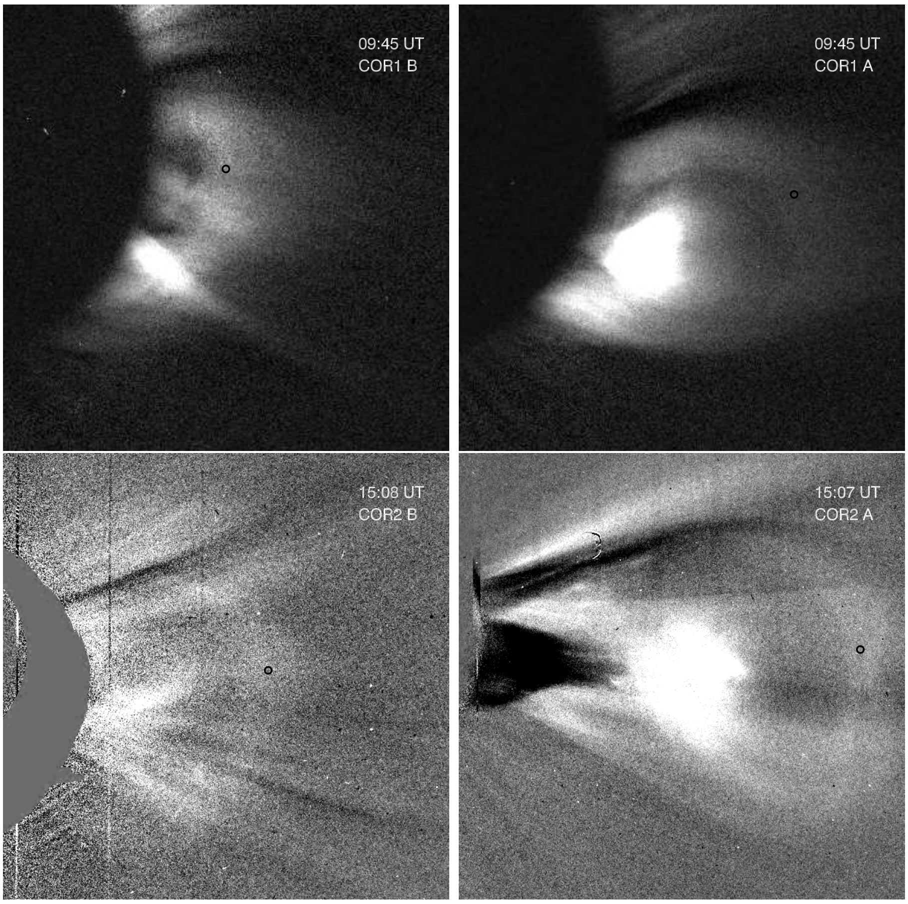

Figure 4.3 The CME on 2007 November 16 seen in images from COR1 (top panels) and COR2 (bottom panels), from STEREO B (left) and A (right). The feature used for reconstruction is circled in each image.

by opening up of the field lines, which can be clearly seen in 171 Å and 195 Å images from EUVI B. From the GOES soft X-ray flux data, we find that the flare started at 00:45 UT, and peaked at 01:03 UT.

This CME was one of the more widely studied CMEs of the rising phase of solar cycle 24. A kinematic analysis of this CME was carried by Temmer *et al.* (2010) who have found its acceleration to be 1300 m s^{-2}, and also by Lin, Gallagher, and Raftery (2010), who have found it over 1000 m s^{-2}. Although both the results above are obtained from stereoscopic reconstruction of the CME, such different values can be expected, as different reconstruction

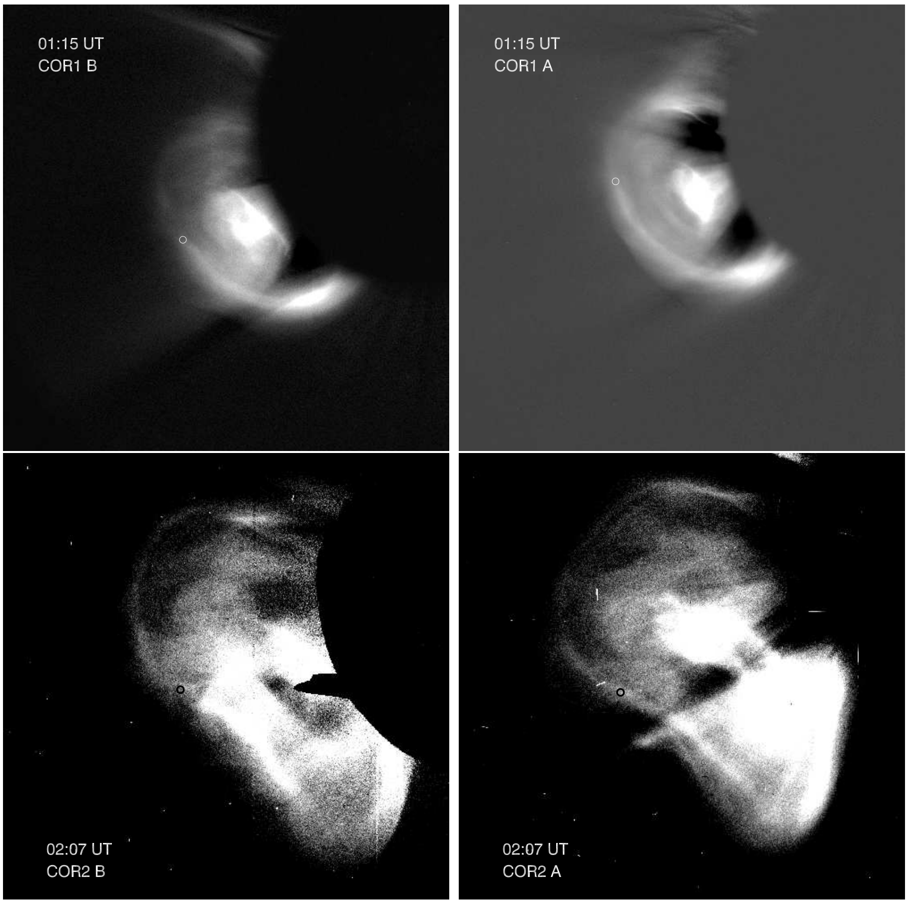

Figure 4.4 The CME on 2007 December 31 seen in images from COR1 (top panels) and COR2 (bottom panels), from STEREO B (left) and A (right). The feature used for reconstruction is circled in each image.

techniques involve different assumptions, and hence can lead to different values of true distance (Mierla *et al.*, 2010). Thernisien, Vourlidas, and Howard (2009) have used the graduated cylindrical shell model (Thernisien, Howard, and Vourlidas, 2006) to fit two shells flanking the cusp seen in the LE of this CME, and employed the forward modelling technique to determine its true direction of propagation and speed.

2008 April 09 CME and EP The CME on 2008 April 09 was associated with an active-region prominence, and was observed on the south-west solar limb, as shown in Figure 4.5. The CME first appeared in the COR1 A and B

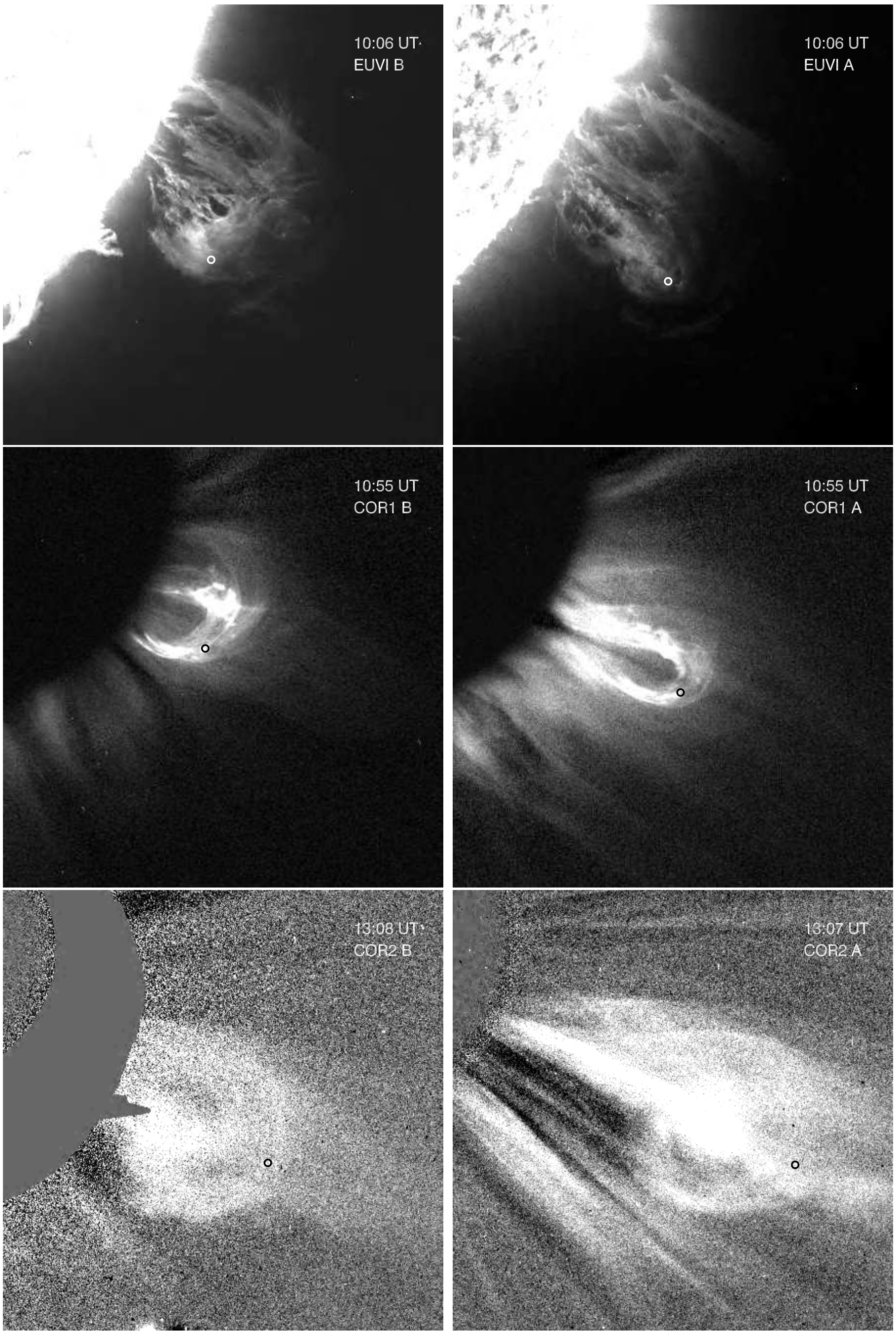

Figure 4.5 The EP on 2008 Apr 09 seen in EUVI 304 Å (top panels), and the associated CME seen in COR1 (middle panels) and COR2 (bottom panels), from STEREO B (left) and A (right). The feature used for reconstruction is circled in each image.

FOVs at 10:15 UT and 10:25 UT respectively, while it could be just seen in COR2 A and B FOVs at 12:07 UT. The LE showed a bright knot close to its highest point, which was tracked during the reconstruction. The prominence material could be seen in 304 Å images from 09:26 UT onwards in EUVI A and 09:46 UT onwards in EUVI B images.

2009 December 16 CME This CME was associated with a C5.3 flare in NOAA AR 11035. It first appeared in the COR1 A and B FOVs at 01:40 UT and 01:35 UT respectively, while it could be just seen in COR2 A and B FOVs at 03:08 UT and 03:39 UT respectively (Figure 4.6). The GOES soft X-ray flux data reveal the flare class to be C5.3, which started at 00:59 UT, and peaked at 01:09 UT.

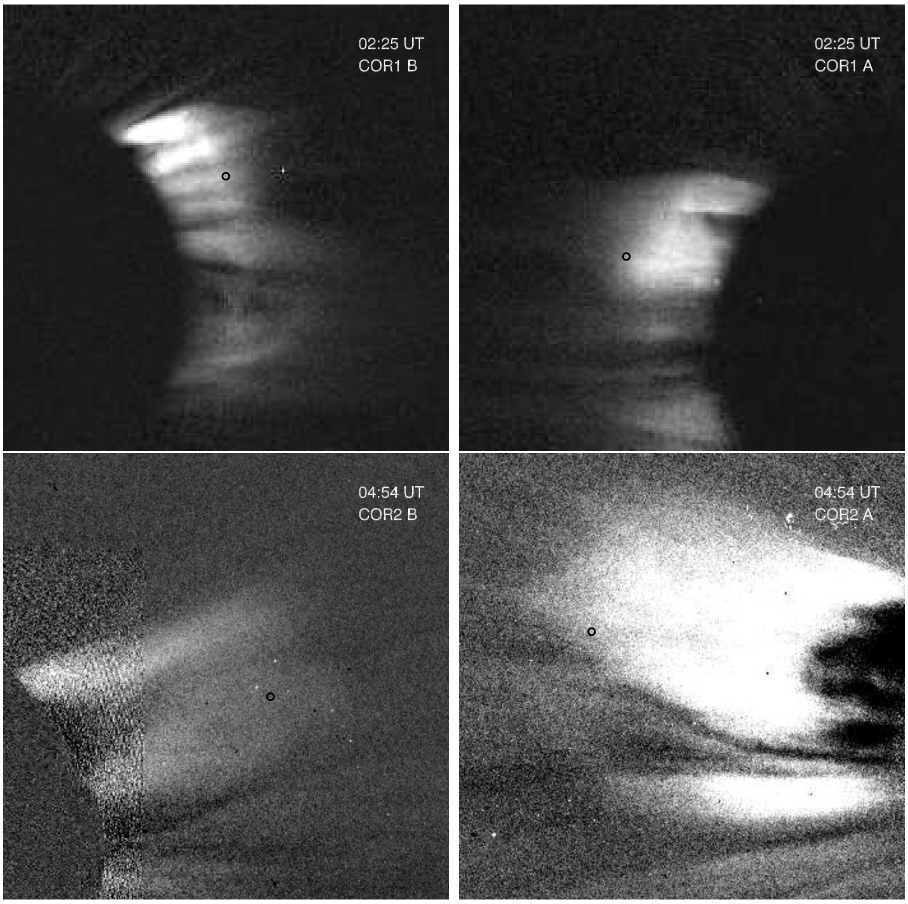

Figure 4.6 The CME on 2009 Dec 16 seen in images from COR1 (top panels) and COR2 (bottom panels), as seen from STEREO B (left) and A (right). The feature used for reconstruction is circled in each image.

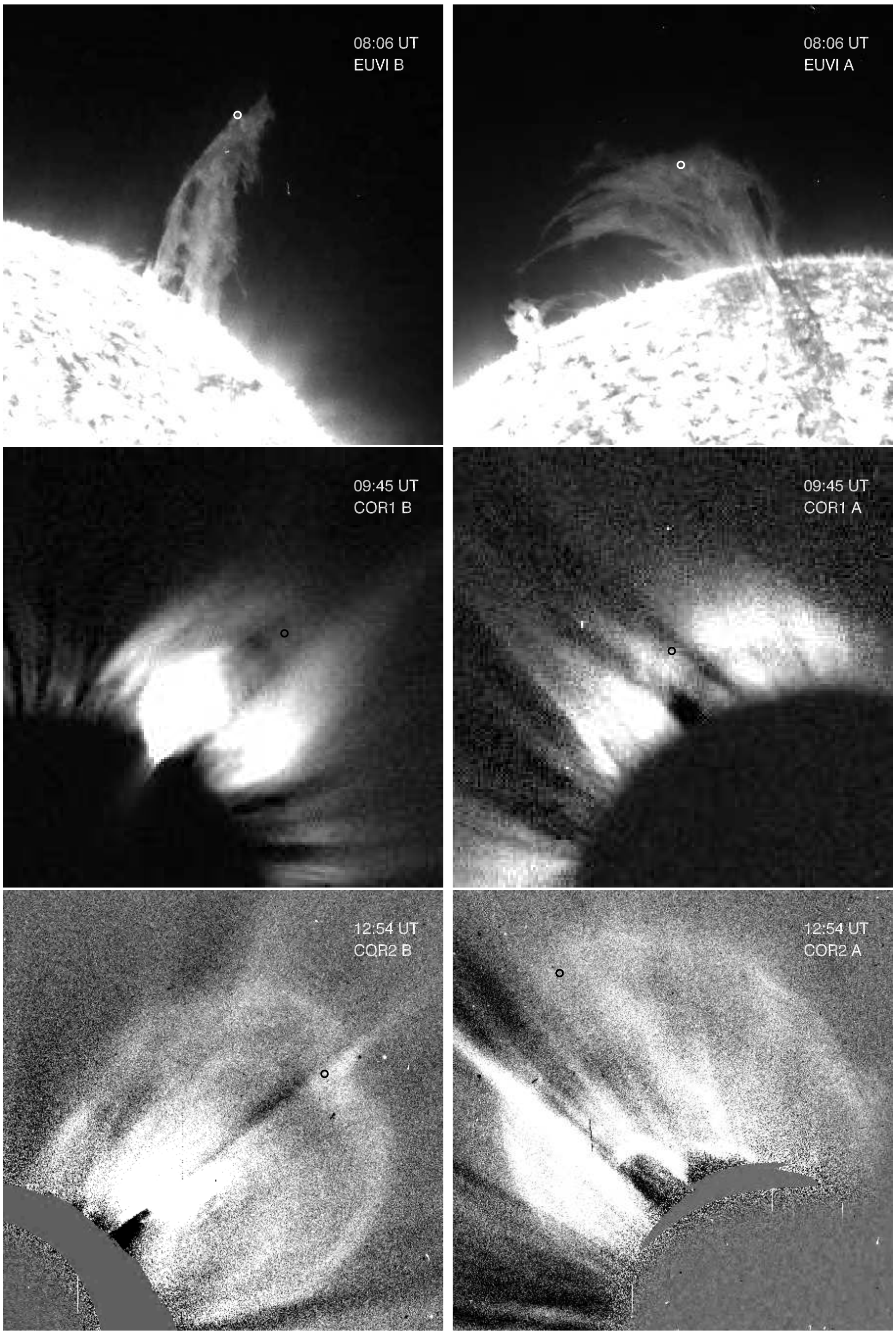

Figure 4.7 The EP on 2010 Apr 13 seen in EUVI 304 Å (top panels), and the associated CME seen in COR1 (middle panels) and COR2 (bottom panels), from STEREO B (left) and A (right). The feature used for reconstruction is circled in each image.

2010 April 13 CME and EP This CME was associated with a large northern polar crown prominence, as seen in Figure 4.7. The prominence spine showed a highly twisted helical structure during its eruption, which was analysed by Joshi and Srivastava (2011a), and is described in Chapter 3. The filament

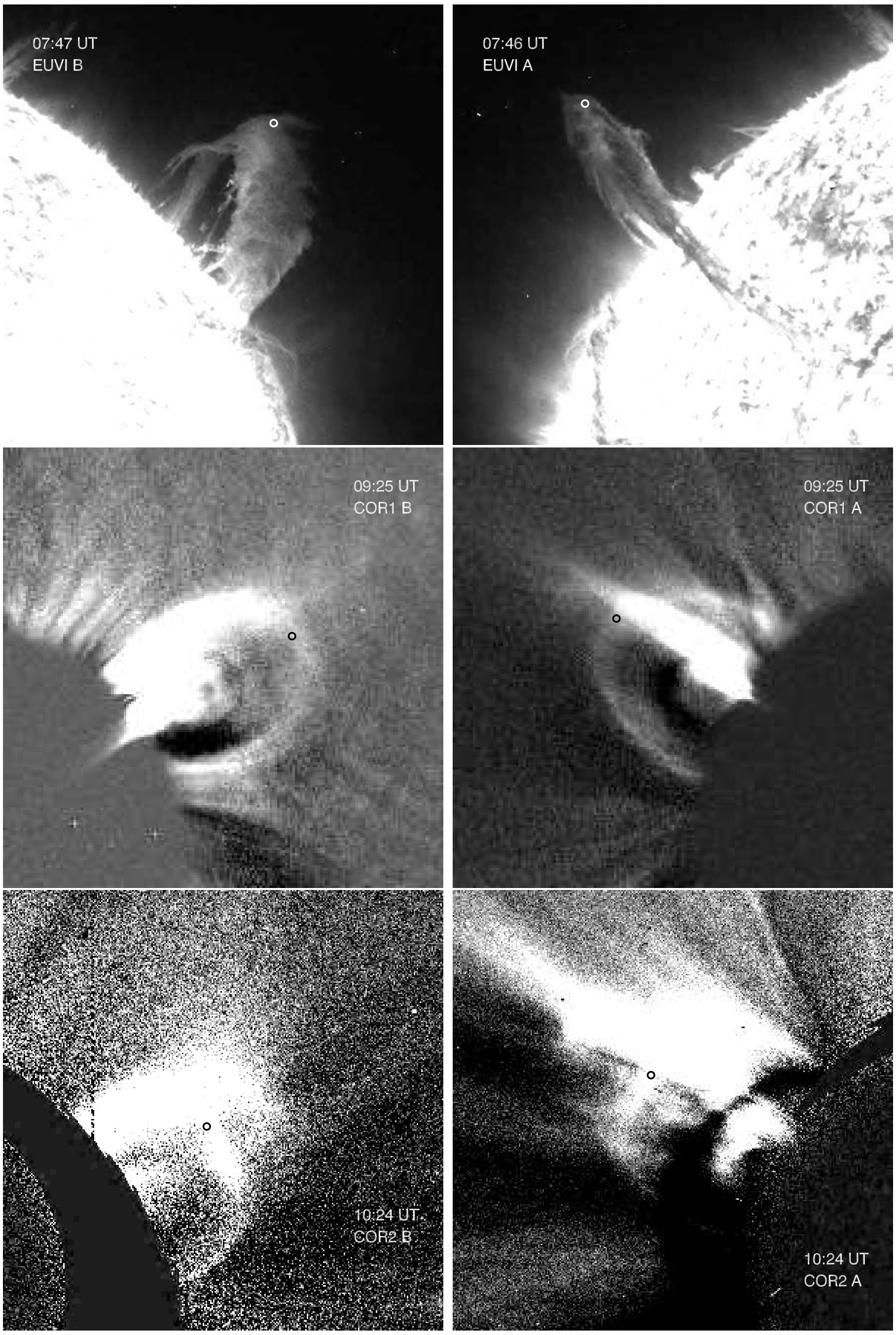

Figure 4.8 The EP on 2010 Aug 01 seen in EUVI 304 Å (top panels), and the associated CME seen in COR1 (middle panels) and COR2 (bottom panels), from STEREO B (left) and A (right). The feature used for reconstruction is circled in each image.

appeared edge-on on the western limb in the EUVI B FOV, but it could be seen extending from the central meridian right up to the north-east limb in EUVI A image. The prominence eruption commenced at 08:36 UT, and the CME LE could be seen at 08:50 and 08:40 UT respectively in COR1 A and B FOVs. The CME LE could be seen in the COR2 FOV 10:39 UT onwards. The prominence material could also be very conspicuously seen in images from both the coronagraphs on the two spacecraft.

2010 August 01 CME and EP This CME was also associated with a northern polar crown filament as seen in Figure 4.8. The filament appeared as a hedgerow prominence in EUVI B 304 Å images, while the line-of-sight was along the spine in EUVI A images. The CME was first seen in COR1 A FOV at 08:10 UT, and at 08:25 UT in COR1 B FOV. Due to a data gap in the COR2 observations, the CME was seen only in single image at 10:24 UT in A and B.

4.3 Results and Discussion

In this chapter, we concentrate mainly on the kinematics of the selected EPs and CMEs, in particular their acceleration as a function of true height. The stereoscopic reconstruction developed by us and described in Chapter 2 is used to determine the true coordinates in heliographic system of the features selected in both the EUVI images and those from the two coronagraphs. In order to determine the kinematics of the features, we have fitted a polynomial, typically of order 5 or 6, to the reconstructed height. The reason to fit a polynomial of such a high order is to be able to see the changes in acceleration, which is the second derivative of height, as a function of time as well as height.

As explained in Chapter 2, the errors in determining the height in images obtained from EUVI, COR1, and COR2 instruments are $0.02\,R_\odot$, $0.12\,R_\odot$, and $0.6\,R_\odot$, respectively. Based on these errors in height, the error propagation formula was implemented on the polynomial fit to calculate the errors in speed and acceleration. Accordingly, the maximum errors in speed and acceleration are $40\,\mathrm{km\,s^{-1}}$ and $25\,\mathrm{m\,s^{-2}}$ respectively.

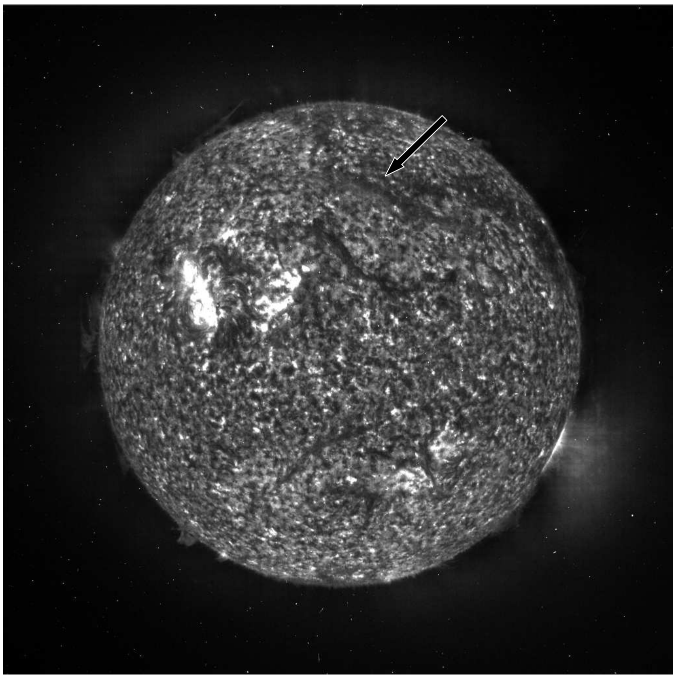

Figure 4.9 The filament on 2010 August 01 appears as a limb prominence in both the STEREO spacecraft as seen in Figure 4.8. However, from this image taken in 304 Å from SoHO/EIT, we see it as a filament on the disc, marked with an arrow. This highlights the importance of the STEREO spacecraft, and the stereoscopic reconstruction possible using images from these spacecraft.

From a single viewpoint, one can measure the projected heights of a CME in a coronagraph. However for a filament on the disc, there are few means available to determine its height. One can make Doppler measurements to estimate the velocity of an on-disc filament, however, such observations are not readily available. As an example, consider the prominence on 2010 August 01, which appeared as a limb event in both the STEREO spacecraft (Figure 4.8). However, when seen from the Earth, it appeared as a filament on the disc, marked in Figure 4.9, which is a 304 Å image from the Extreme Ultraviolet Imaging Telescope (EIT), on board the SoHO satellite. It is not possible to determine the kinematic evolution of this filament from such an image alone. It is only with the advent of STEREO, with its two spacecraft separated in the ecliptic plane, that we are able to carry out three-dimensional measurements extensively.

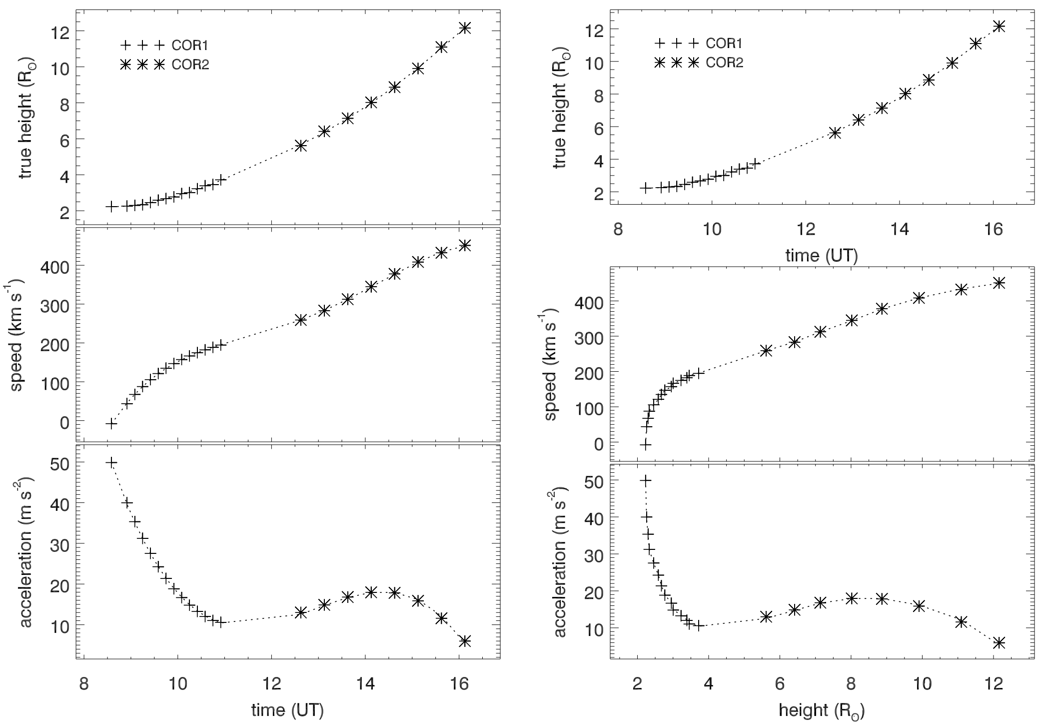

Figure 4.10 Results from the stereoscopic reconstruction applied to a feature in LE of the CME on 2007 November 16. Left: True height of the CME feature against time in the top panel, followed by the true speed and acceleration against time in the middle and bottom panels. Right: True height of the CME against time at the top, followed by the true speed and acceleration against true height in the middle and bottom panels. Plus signs (+) and asterisks (*) indicate that the feature was observed in COR1 and COR2 FOVs, respectively.

2007 November 16 CME In Figure 4.10, the plots on the left show change in reconstructed height, and the resultant speed and acceleration obtained from the fitted polynomial, as a function of time, while the plots on right show speed and acceleration as a function of true height. From this figure we find that the CME speed increases very rapidly in the COR1 FOV, and is almost constant in COR2 FOV. The acceleration at the start of the CME is $50\,\mathrm{m\,s^{-2}}$, but it falls rapidly, and reaches $11\,\mathrm{m\,s^{-2}}$ at about $3.7\,\mathrm{R_\odot}$. Thus, maximum value of acceleration, and the height at which the CME attained this value, are not available to us. We however point out that the maximum acceleration of the CME occurred at or less than $2\,R_\odot$ in height. In the higher corona, *i.e.*, in the COR2 FOV we see that the acceleration once again rises by a small amount to reach $18\,\mathrm{m\,s^{-2}}$ at a height of around $8\,R_\odot$, which can be attributed to the residual acceleration phase, as proposed by Chen and Krall (2003), discussed in § 4.1.

2007 December 31 CME This CME was associated with a solar flare on the eastern limb, with the GOES soft X-ray class C8. The CME speed increased in the lower corona to reach $812\,\mathrm{km\,s^{-1}}$ at a height of $4.5\,R_\odot$, and showed a little dip before attaining a constant value of around $870\,\mathrm{km\,s^{-1}}$ (Figure 4.11). This CME has the highest value of maximum acceleration of all the CMEs studied here, which is over $1500\,\mathrm{m\,s^{-2}}$ at a height of about $2\,R_\odot$. This is typical of CMEs associated with flares, which are termed as impulsive by Sheeley *et al.* (1999) and Moon *et al.* (2002). However, the flare in this case was classified with X-ray class C8, and such high values of CME acceleration are earlier reported to be associated with X-class flares. For example, acceleration of over $1700\,\mathrm{m\,s^{-2}}$ has been reported by Alexander, Metcalf, and Nitta (2002) for a CME associated with an X1.2 class flare. This CME achieved its maximum value somewhere below $2\,R_\odot$, and later showed a residual acceleration of $90\,\mathrm{m\,s^{-2}}$ at a height of $6\,R_\odot$.

2008 April 09 CME and EP The LE of this CME showed very smooth changes in both its speed and acceleration, as can be seen from Figure 4.12. The speed increased till the CME reached about $4\,R_\odot$, but the peak of the acceleration profile could not be observed, which as in the previous case occurred below $2\,R_\odot$. The acceleration kept on decreasing till it reached a value of around $-14\,\mathrm{m\,s^{-2}}$. Correspondingly, the speed attained a maximum of $530\,\mathrm{km\,s^{-1}}$, before decreasing till $\sim 11.5\,R_\odot$. The prominence associated with this CME

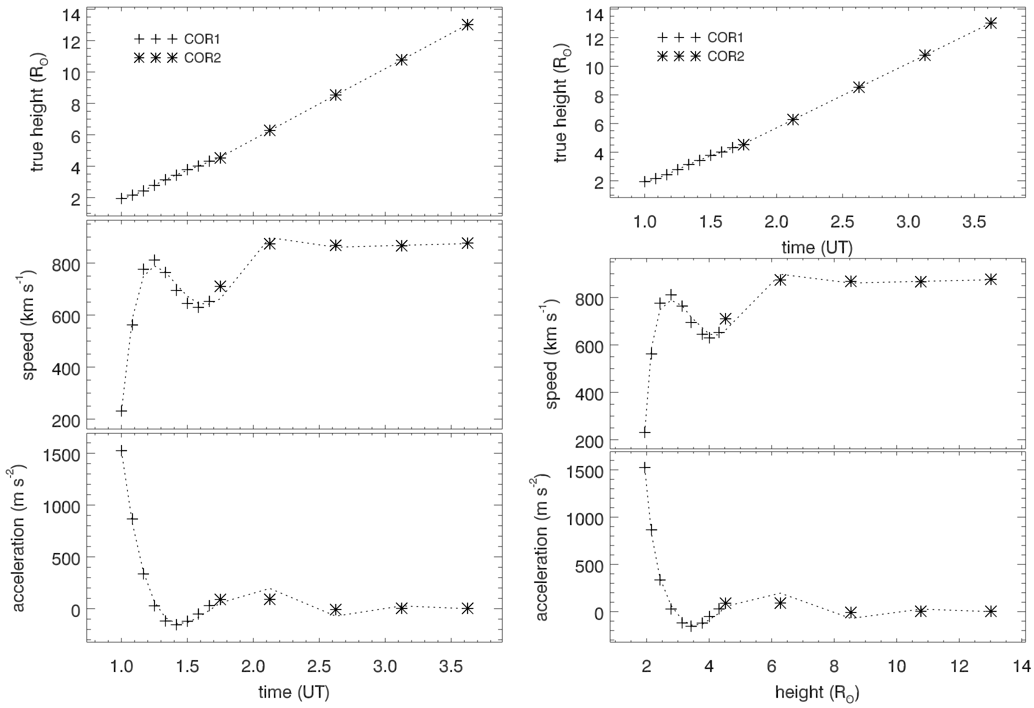

Figure 4.11 Results from the stereoscopic reconstruction applied to a feature in LE of the CME on 2007 December 31. *Left*: True height of the CME feature against time in the top panel, followed by the true speed and acceleration against time in the middle and bottom panels. *Right*: True height of the CME against time at the top, followed by the true speed and acceleration against true height in the middle and bottom panels. Plus signs (+) and asterisks (*) indicate that the feature was observed in COR1 and COR2 FOVs, respectively.

showed an increase in acceleration up to a height of almost 4 $R_\odot$, till the time it could be observed in COR1 images. A prominence is generally not known to accelerate at such large heights. However, velocity of the prominence ($\sim$250 km s^{-1}) was found to be less than that of the CME ($>$ 400 km s^{-1}).

2009 December 16 CME From the COR1 observations, we could not observe the peak of acceleration of the CME. We could only observe the drop in acceleration from around $90 - 0$ m s^{-2} as the CME travels from a height of 2 to 6 $R_\odot$, as seen in Figure 4.13. Once the acceleration reached 0 m s^{-2} at 6 $R_\odot$, the CME velocity attains a value of 350 km s^{-1}. Later, at a height of around 11 $R_\odot$, we find that acceleration shows a smaller rise before reaching

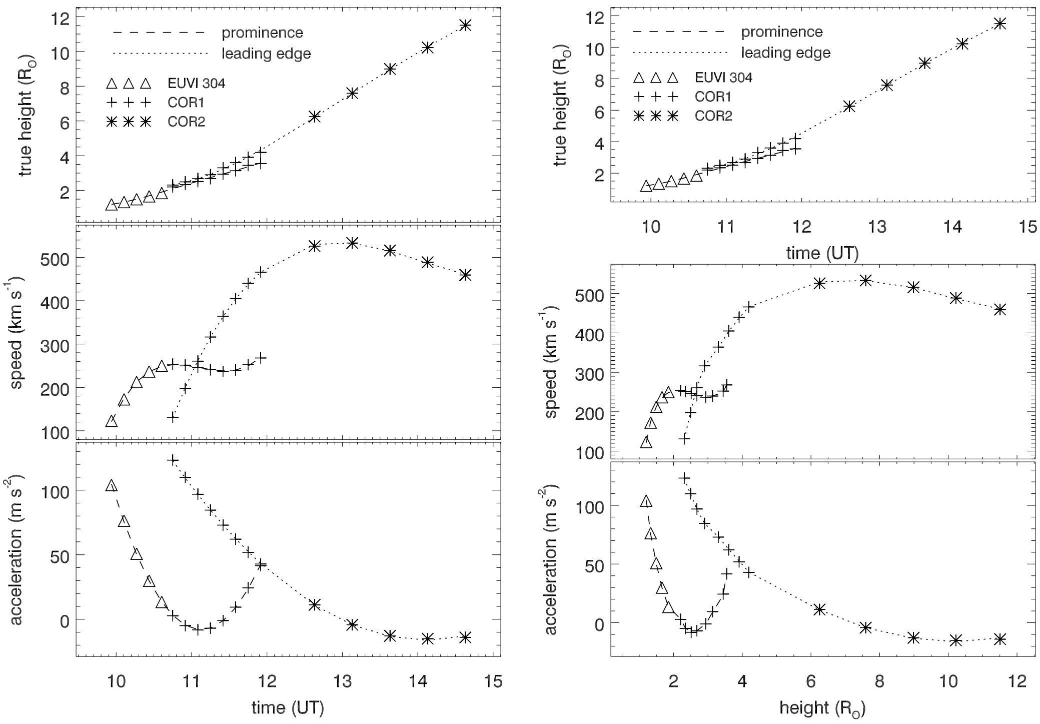

Figure 4.12 Results from the stereoscopic reconstruction applied to features in the LE and the associated prominence of the CME on 2008 April 09. *Left*: True height of the features against time in the top panel, followed by the true speed and acceleration against time in the middle and bottom panels. *Right*: True height of the CME against time at the top, followed by the true speed and acceleration against true height in the middle and bottom panels. Here, triangles (△), plus signs (+) and asterisks (*) indicate that the feature was observed respectively in EUVI 304 Å, COR1 and COR2 FOVs. Dashed line is the polynomial fit to prominence measurements, whereas dotted line is the fit to LE measurements.

a value of $-20\,\mathrm{m\,s^{-2}}$ at $14\,\mathrm{R_\odot}$, similar to the rise observed in the CMEs on 2007 November 16 and 2007 December 31.

2010 April 13 CME and EP This CME was associated with a large northern hemisphere polar crown prominence eruption. The LE showed changes in speed and acceleration similar to the one on 2007 November 16 (Figures 4.10 and 4.14). Its speed reached $300\,\mathrm{km\,s^{-1}}$ at height $\sim 4\,\mathrm{R_\odot}$, and during the same time its acceleration dropped from 60 to $27\,\mathrm{m\,s^{-2}}$. The peak of the acceleration however could not be observed. Like the event of 2008 April 09,

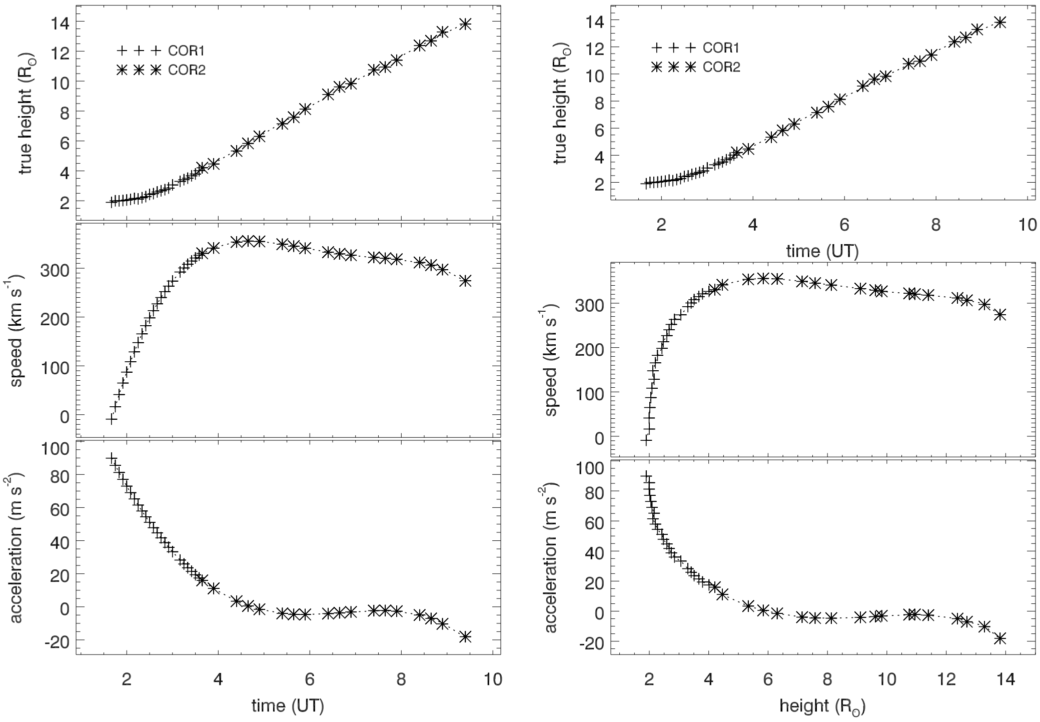

Figure 4.13 Results from the stereoscopic reconstruction applied to a feature in LE of the CME on 2009 December 16. Left: True height of the CME feature against time in the top panel, followed by the true speed and acceleration against time in the middle and bottom panels. Right: True height of the CME against time at the top, followed by the true speed and acceleration against true height in the middle and bottom panels. Plus signs (+) and asterisks (*) indicate that the feature was observed in COR1 and COR2 FOVs, respectively.

here too we find the prominence showing an increasing acceleration at least till $4\,R_\odot$.

2010 August 01 CME and EP This CME too was associated with a large northern hemisphere polar crown prominence eruption, just like the CME on 2010 April 13. The LE behaved very differently from that of the other CMEs analysed in this study. Its speed was very low at the start, and it gradually reached a maximum speed of $\sim 570\,\mathrm{km\,s^{-1}}$, as shown in Figure 4.15. At this height of around $4.5\,R_\odot$, the CME was still showing acceleration over $200\,\mathrm{m\,s^{-2}}$, but owing to a data gap in the COR2 observations, its peak value could not be determined. The prominence in this case showed an accelera-

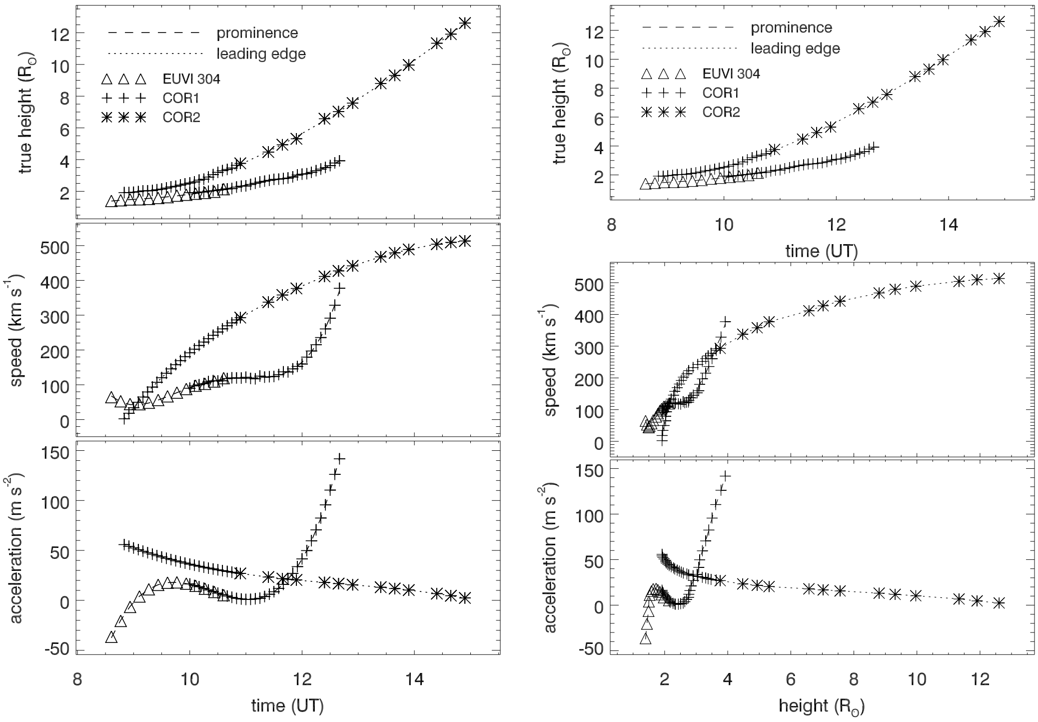

Figure 4.14 Results from the stereoscopic reconstruction applied to features in the LE and the associated prominence of the CME on 2010 April 13. *Left*: True height of the features against time in the top panel, followed by the true speed and acceleration against time in the middle and bottom panels. *Right*: True height of the CME against time at the top, followed by the true speed and acceleration against true height in the middle and bottom panels. Here, triangles (△), plus signs (+) and asterisks (*) indicate that the feature was observed respectively in EUVI 304 Å, COR1 and COR2 FOVs. Dashed line is the polynomial fit to prominence measurements, whereas dotted line is the fit to LE measurements.

tion peak at about $1.5\,R_\odot$ with a value of $40\,\mathrm{m\,s^{-2}}$, and then showed a steady decrease to around $10\,\mathrm{m\,s^{-2}}$ at a height of $3\,R_\odot$.

4.4 Conclusions

The eruption of solar prominences and CMEs is closely linked, as very often the filament material is ejected along with the CME. Models describing initiation of CMEs like breakout (Antiochos, DeVore, and Klimchuk, 1999) and tether-cutting (Forbes and Isenberg, 1991) take into account the filament lying at the base of

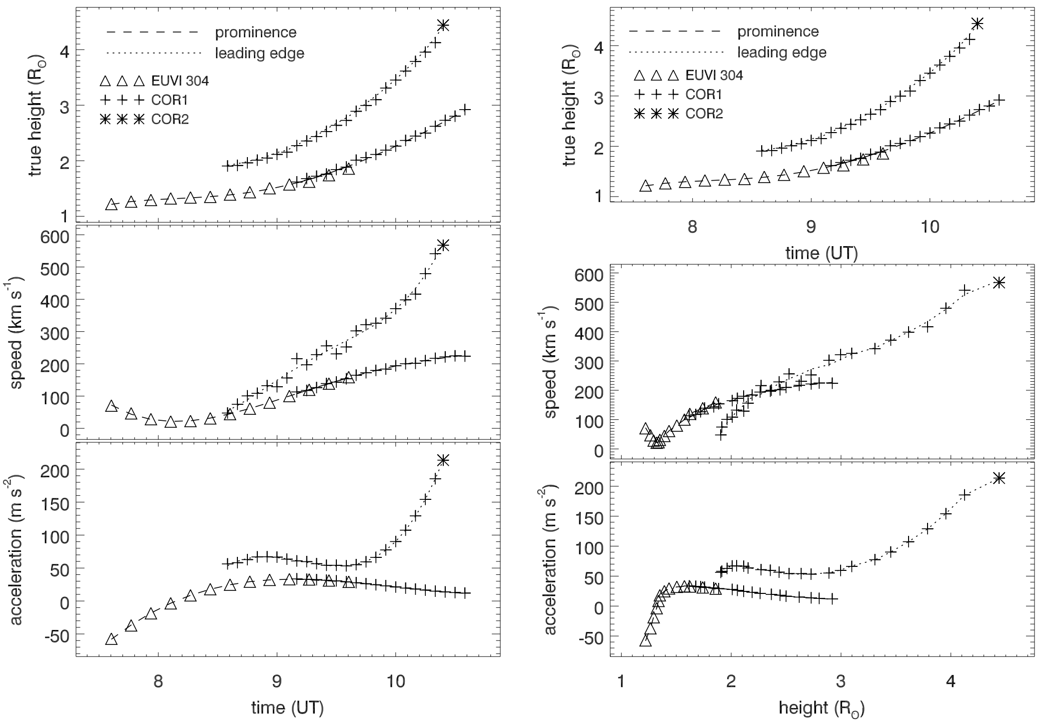

Figure 4.15 Results from the stereoscopic reconstruction applied to features in the LE and the associated prominence of the CME on 2010 August 01. *Left*: True height of the features against time in the top panel, followed by the true speed and acceleration against time in the middle and bottom panels. *Right*: True height of the CME against time at the top, followed by the true speed and acceleration against true height in the middle and bottom panels. Here, triangles (△), plus signs (+) and asterisks (*) indicate that the feature was observed respectively in EUVI 304 Å, COR1 and COR2 FOVs. Dashed line is the polynomial fit to prominence measurements, whereas dotted line is the fit to LE measurements.

magnetic field lines. To study the dynamics of these closely-associated phenomena together, we have analysed six CMEs observed by the coronagraphs COR1 and COR2, and the associated EPs in three of the cases observed by EUVI on board the identical STEREO A and B spacecraft. We identified and tracked a feature in the LE of all the CMEs in both COR1 and COR2, and also in the three associated EP. While most of the earlier studies on CME acceleration were carried out using projected measurements, we have used a stereoscopic reconstruction technique, discussed in Chapter 3, and also in Joshi and Srivastava (2011a), to obtain the true coordinates, and hence the true speed and acceleration of the feature. On fitting

Event	v_{max} ($\mathrm{km\,s^{-1}}$)	height of v_{max} ($R_\odot$)	a_{max} ($\mathrm{m\,s^{-2}}$)	height of a_{max} ($R_\odot$)	v at $10\,R_\odot$	a at $10\,R_\odot$
16 Nov 2007 LE	451	12.2	50	2.2	408	16
31 Dec 2007 LE	876	13.0	1524	1.9	860	2
9 Apr 2008 LE	533	7.6	123	2.3	488	-15
16 Dec 2009 LE	356	5.8	90	1.9	488	-15
13 Apr 2010 LE	522	12.6	61	1.9	193	36
1 Aug 2010 LE	567	4.4	213	4.4	—	—
9 Apr 2008 EP	268	3.5	104	1.2	—	—
13 Apr 2010 EP	377	3.9	141	3.9	—	—
1 Aug 2010 EP	224	2.9	34	1.6	—	—

Table 4.1 Summary of the 6 LEs and 3 EPs analysed using three-dimensional reconstruction. v_{max} and a_{max} denote the maximum speed and acceleration of the CME calculated. The heights at which CMEs attained these values are also provided. The last two columns show the speed and acceleration of the CMEs at a distance of $10\,R_\odot$.

a high-order polynomial function to the true height, the speed and acceleration of the CMEs and EPs as a function of time and the true height were determined. The results of the kinematic study of EPs and the CME LEs are shown in Figures 4.10–4.15. We summarise the results obtained from reconstruction in Table 4.1.

Earlier studies (Zhang *et al.*, 2001; Chen and Krall, 2003), have observed CMEs in all the three SoHO/LASCO coronagraphs which together cover a range from $1.1-32\,R_\odot$. In such studies, the initiation phase of the CME, as well as peak of their acceleration could be observed. The COR1 and COR2 coronagraphs together image the solar corona from $1.4-15.0\,R_\odot$, which are the plane-of-sky FOVs of the coronagraphs. Because of projection effects, height obtained from stereoscopic reconstruction of a feature in the corona is always more that its height measured in the plane-of-sky. Thus, from reconstruction, we obtain heights of CME features from just a little less than $2.0\,R_\odot$, well above the lowest height at which the COR1 coronagraph could observe. Thus, in most of the cases we do not capture the rise phase acceleration of the LE of CME. In all but one case studied here, the acceleration peak has already passed from the time we start observing the CME. At this point, it is necessary to point out that the heights determined in this study are true heliocentric distances, hence they are seen to be significantly different than the projected heights obtained from previous studies which relied upon observations from a single spacecraft.

We estimated the maximum acceleration, average acceleration, acceleration magnitude, and acceleration duration, attained by the CMEs and EPs. Acceleration duration is defined as the time interval between the maximum and the zero value of acceleration, while acceleration magnitude is the velocity increase during this time divided by acceleration duration (Zhang and Dere, 2006). The very high acceleration for the 2007 December 31 CME ($> 1500\,\mathrm{m\,s^{-2}}$) makes the event an *outlier*, hence, we have not included that value in the scatter plots in Figure 4.16. The left panel shows scatter plot of speed at maximum acceleration versus the maximum acceleration. From this figure we find that for the events studied, higher the maximum value of acceleration, higher is the speed at that instant. While, the right panel of Figure 4.16 shows scatter plot of height at the instance of maximum acceleration versus the value of maximum acceleration. This figure suggests that higher the acceleration, higher up in the corona it occurs.

It is believed that most of the CME acceleration typically occurs in the lower corona. Chen and Krall (2003) have taken the height of maximum acceleration of CME to be less than $2-3\,\mathrm{R}_\odot$, while, Vršnak (2001b) have considered this height to be $4\,\mathrm{R}_\odot$. However, from our reconstructed results (Figures 4.10–4.15), we observe that in all the cases studied here, the peak of main phase of acceleration of the CME LE lies below the true height of $2\,\mathrm{R}_\odot$. Thus, we now have a refined upper limit for height at which the peak of CME acceleration takes place, indicating that most of the CME dynamics occurs closer to the Sun than previously suggested. Since projected measurements tend to underestimate the height, such a result coming from reconstructed measurements is a little counter-intuitive.

The CME on 2007 December 31, analysed in this study, was associated with a C-class flare, however, as mentioned above, it showed an acceleration of over $1500\,\mathrm{m\,s^{-2}}$ (Figure 4.11). Previous studies have shown that the acceleration phase

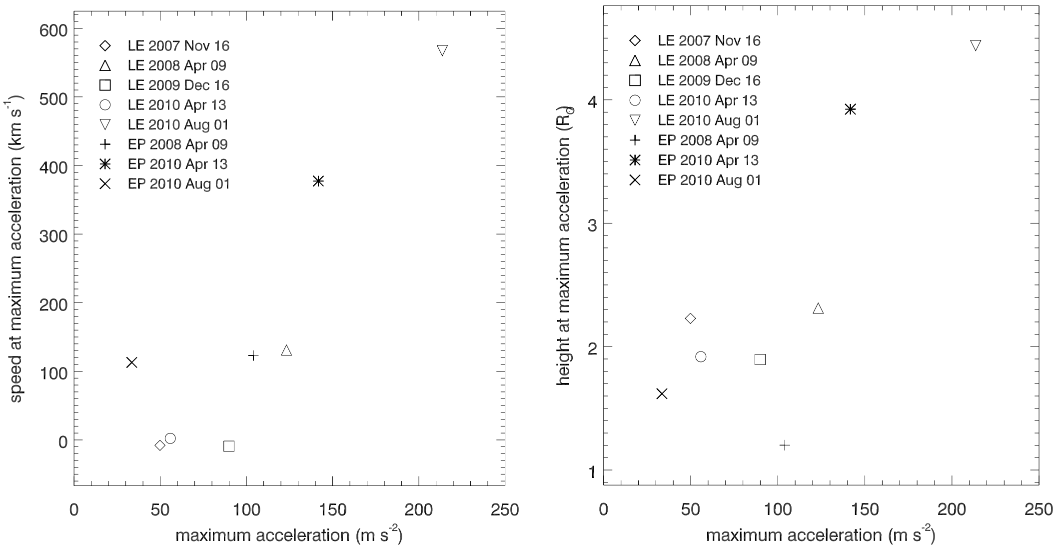

Figure 4.16 Scatter plots of speed (left panel), and height (right panel) at the instance of maximum acceleration versus the maximum acceleration of the 6 CMEs and 3 EPs studied. The legend shows data points corresponding to each event. Data point for 2007 December 31 is not shown since it has a very high value of maximum acceleration of $1524\,\mathrm{m\,s^{-2}}$.

of CMEs coincides with the increase in soft X-ray flux due to the associated flare (Neupert *et al.*, 2001; Shanmugaraju *et al.*, 2003). Maričić *et al.* (2007) have also

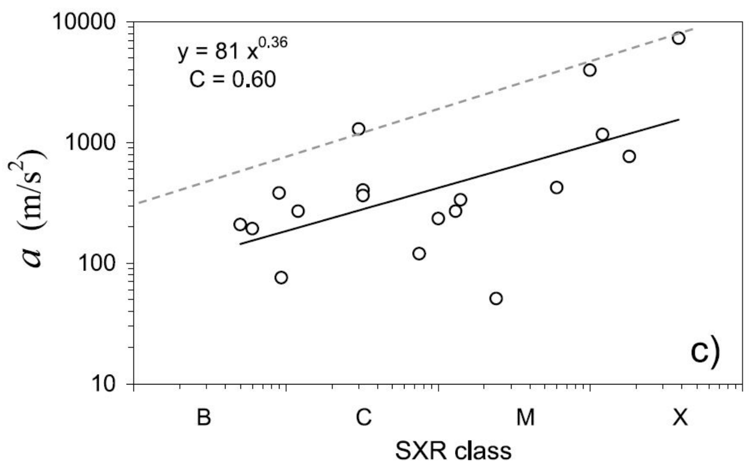

Figure 4.17 Result from a statistical study of 22 events by Maričić *et al.* (2007). The acceleration of CMEs as a function of the soft X-ray class of the associated flares. The least squares fit is shown by means of a solid line, whereas the dashed line shows an upper limit.

shown from a statistical study of 22 events, that both the velocity and acceleration of the CME show a significant correlation with the X-ray class of the associated flare, shown in Figure 4.17 taken from their paper. As per the least squares fit obtained from their study, acceleration of the CME associated with a C8 flare should be less than 400 $\mathrm{m\,s^{-2}}$. The acceleration calculated by us however, is almost 4 times this value, suggesting that the flare energy alone might not be the only driving force for a CME. In such a scenario, the supposition that impulsive and gradual CMEs are respectively associated with flares and EPs (MacQueen and Fisher, 1983; Moon *et al.*, 2002) should also be subjected to further scrutiny. Also, deviations to the findings reported by Maričić *et al.* (2007), where acceleration of CMEs is dependent on the X-ray class of the associated flare, should not be ignored.

Previous studies have reported that acceleration of a CME shows bimodal distribution (Chen and Krall, 2003). We observe such a bimodal distribution in 3 CMEs, the ones which are not associated with prominence eruptions. The residual acceleration for the very impulsive 2007 December 31 CME was 90 $\mathrm{m\,s^{-2}}$, while for the CMEs on 2007 November 16 and 2009 December 16, it was found to be 18 $\mathrm{m\,s^{-2}}$ and -2 $\mathrm{m\,s^{-2}}$, respectively (Figures 4.10, 4.11 and 4.13). The other CMEs, which are associated with EPs do not show such a bimodal acceleration profile. Chen and Krall (2003) have invoked the flux injection mechanism to trigger an eruption in a magnetic flux rope, which leads to the residual acceleration phase. We observe that only the flare-associated CMEs undergo residual acceleration, which indicates that flux injection seems to be a good explanation for eruption of the flare-associated CMEs studied here, but a different mechanism should be considered for EP-associated CMEs.

Of the three CMEs associated with prominences, the 2010 April 13 and 2010 August 01 CMEs were associated with large quiescent polar crown prominences, while the one on 2008 April 09 was associated with an active-region prominence. We find that the prominences on 2008 April 09 and 2010 April 13 showed a strong positive acceleration in the COR1 FOV, when they attained a height of $\sim 4\,R_\odot$. During the same time however, acceleration of the CME LE was decreasing. Srivastava *et al.* (2000); Maričić *et al.* (2004), based on observations from a single spacecraft have shown that forces acting on the CME and the EP are the same. However, acceleration profiles of the two prominences on 2010 April 13 and 2010 August 01 obtained from stereoscopic reconstruction indicate, that even at a height of $4\,R_\odot$, these forces cannot be considered to be the same.

All the results presented in this chapter are inferred from the six cases studied, and have been published in Joshi and Srivastava (2011b). In order to make a more conclusive statement about the factors governing dynamics of CMEs and EPs, it is necessary to analyse several more such events. This study has been carried out by employing the three-dimensional reconstruction technique, for which the events observed by the STEREO spacecraft were the most suitable. Thus, inadvertently, we had to select the events occurring in the long and deep minimum preceding solar cycle 24. In future, one also has to investigate if the some of the results would be altered if the events belong to the maximum phase of the solar cycle.

Chapter 5

Doppler and Full-Disc Hα Observations

5.1 Introduction

In the earlier chapters, dynamics of prominences are discussed in their pre-eruptive and eruptive stages, as also the kinematics of the associated CMEs. The observations for these studies are from the twin STEREO spacecraft. The simultaneous images from the identical instruments of the SECCHI suite on board STEREO allow us to make three-dimensional stereoscopic reconstruction of various solar features, thus providing us with a knowledge of their true evolution.

These activations cannot be observed using Hα images alone, as the changes taking place in the spine are gain additional importance, since the present prominence models do not take into account the motions at such a small scale. Such small-scale motions could be a proxy for filament activations, and may slowly build up causing a filament to erupt. Indeed, .

Such studies are important in order to understand the dynamics of prominences in their eruptive stages. However, filaments continuously exhibit motions at a small scale. Filaments are observed to show activation, which is a precursor to eruption, up to 1–4 days prior to their eruptions (Sara Martin, *private communi-*

cation). In order to study the activation of filaments, Hα imaging data alone can prove to be insufficient. Once the velocities become large, the Doppler shifts will carry the filament away from the line centre, and out of the Hα pass-band. Especially important are the EPs close to the central meridian, as CMEs associated with them (§ 1.3.2) are more likely to be geo-effective (Srivastava and Venkatakrishnan, 2004). Thus, by observing the activation of filaments close to disc-centre, it should be possible to issue a forewarning of an imminent CME, which would be extremely helpful from the point of view of space weather. With this as a future goal, we have installed a new telescope at the USO premises, named the Hα Doppler Imager (HaDI). This telescope is equipped with a tunable Fabry-Pérot etalon (FP), which will be used to obtain image of the Sun in line centre and wings of the Hα line, from which line-of-sight velocities can be determined. Thus, it would allow us to study the filaments even in their activated stages.

Figure 5.1 The building housing the Hα Doppler Imager, with the dome fully collapsed, while recording observations. The telescope is enclosed in the white box on top of the building.

5.2 Hα Doppler Imager

This is a new instrument developed and installed at the USO premises, and is being set up to study different aspects of solar filaments (Figure 5.1). Its main aim is to monitor the activation and eruption of filaments, by measuring their line-of-sight velocities. The optical set-up of the telescope is shown in Figure 5.2. The objective is a 15 cm singlet lens, followed by a collimating lens, an imaging lens, and the CCD camera. We have used a camera procured from Finger Lakes Instrumentation, having a Kodak CCD chip of size 4096×4096 pixels. A narrow-band FP with a Lithium Niobate ($LiNbO_3$) wafer is the major component of this telescope. It is placed in the collimating beam of the telescope. At four positions the light beam is folded by means of plane mirrors to keep the beam within the box. The telescope is in the form of a closed box and is housed in a building, as shown in Figure 5.1. The building has a collapsible dome, which can be fully opened. Because of the open dome, even a small wind flow eliminates any temperature differences around the telescope. This leads to better seeing conditions throughout the day, compared to a conventional dome with a slit.

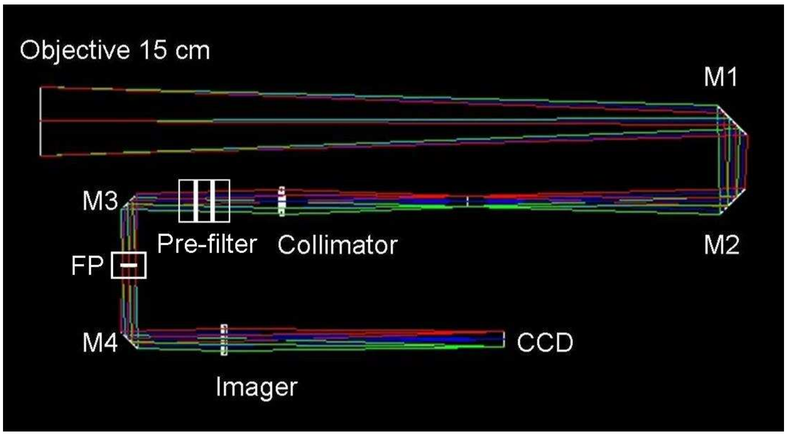

Figure 5.2 Optical set-up of the Hα Doppler Imager. The objective is a 15 cm singlet lens, followed by a collimating lens, an imaging lens, and a CCD camera. The pre-filter and FP are placed in the collimating beam. M1 to M4 are folding mirrors to keep the light beam within the enclosure.

For our set-up, we use a combination of the $LiNbO_3$ FP and a relatively broad-band interference filter with a pass-band of 1 Å, which acts as a pre-filter. Light passing through the FP shows periodic transmission peaks, known as channels, described in more detail in § 5.2.1. We would be centring one of the FP channels in the wings of the Hα line. To suppress all the other channels, we use the pre-filter. It consists of two 1.4 Å single-period interference filters. Sandwiched between them are a linear polarizer (LP) and a quarter wave plate (QWP), which eliminate internal reflections between the two interference filters. The pre-filter is also centred on the Hα line.

The pass-bands of the FP and the pre-filter are sensitive to temperature, and hence both have to be kept at a constant temperature. Hence, the FP is kept in at temperature controlled oven maintained at 42.5°C, which is the maximum ambient temperature at Udaipur. The oven, which is built at USO, is accurate up to 0.0625°C. A 12-bit digital temperature sensor, DS620, from Dallas Semiconductors, is used for measuring the oven temperature. The oven is designed such that in case the temperature exceeds 47°C, power to the heating element is cut off and is restored only once it drops below 45°C. The pre-filter is similarly kept inside an oven at a constant temperature of 45°C, designed at USO.

The FP has to be tuned at various positions along the Hα line to measure velocities along the line-of-sight. If the pre-filter is fixed on the Hα line centre, the transmitted intensity would decrease due to the pre-filter profile as the FP is tuned away from the line centre. For this reason, the pre-filter also has to be tuned at the same position as the FP. The tuning is done by rotating the pre-filter about the normal direction. As it is rotated away from the normal, its pass-band peak shifts towards the blue side, *i.e.*, to lower wavelengths. Hence, the pre-filter oven is set at a temperature of 45°C, so that when at normal incidence, the pre-filter is centred in the red wing of the Hα line.

Figure 5.3a shows the theoretical profiles of the FP (dotted line) and pre-filter (dash-dotted line) plotted over the Hα absorption line (solid line). The pre-filter

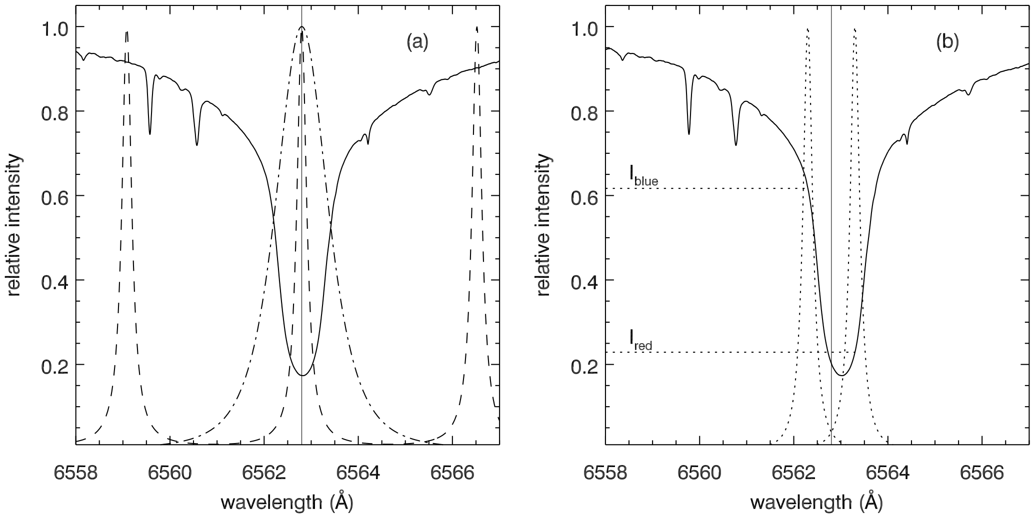

Figure 5.3 (a) Theoretical profiles of FP (dotted line) and pre-filter (dash-dotted line) plotted over the Hα absorption line (solid line). (b) Hα line with a Doppler shift of 0.2 Å shown along with combined transmission profile of FP and pre-filter at ± 0.5 Å having intensities I_{blue} and I_{red}.

and one of the FP channels is centred over the Hα line centre. Figure 5.3b shows the Hα line with a Doppler shift of 0.2 Å, where the Hα line centre is marked with the solid vertical line. The combined transmission profile of FP and pre-filter is shown at $\lambda_0 - 0.5$ Å and $\lambda_0 + 0.5$ Å, where the intensity in the Hα line is I_{blue} and I_{red} respectively. The Doppler velocity, v, can be determined by the following relation.

$$I_{blue} - I_{red} \propto \lambda - \lambda_0 \tag{5.1}$$

$$\text{where,} \quad \frac{\lambda - \lambda_0}{\lambda} = \frac{v}{c} \tag{5.2}$$

To determine the proportionality factor in Equation 5.1, we will construct a look-up table which will be used to determine the Doppler velocity directly from the intensities in the blue and red wings of Hα.

5.2.1 The Fabry-Pérot (FP) etalon

An FP works on the principle of multiple-beam interferometry. It consists of two highly polished thin plates separated either by air or a medium. A ray diagram for an air-spaced FP is shown in Figure 5.4. Point P_1 on an object makes an angle of incidence θ on the FP, shown having plates E_1 and E_2. Rays from the FP are focused by a lens L on the screen at point P_2. If μ is the refractive index of the medium between the two plates separated by a distance d, then for a given angle of incidence θ, the maximum occurs at the wavelengths where an integer value of m satisfies the following relation.

$$2\,\mu\,d\,\cos\theta = m\,\lambda \tag{5.3}$$

For a given angle of incidence, the wavelengths that satisfy the above equation for integer values of m have the maximum transmission. Each maximum is known as a channel, which occur periodically. The separation between two consecutive channels is known as the free spectral range (FSR), and is given by:

$$FSR = \frac{\lambda^2}{2\,\mu\,d} \tag{5.4}$$

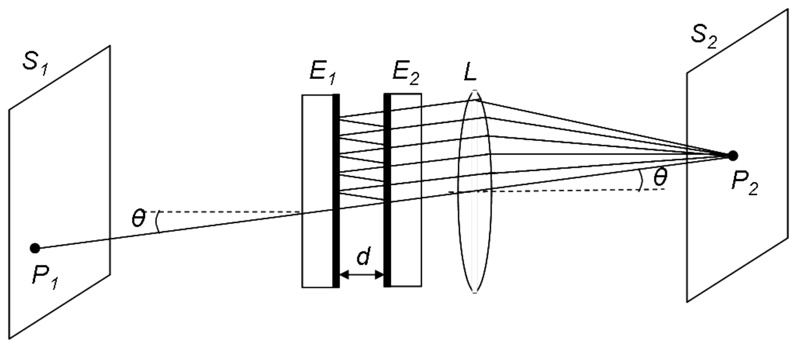

Figure 5.4 A ray from point P_1 is imaged on the screen at P_2 after passing through the FP etalon with plates E_1 and E_2 separated by a distance d. Adopted from Jenkins and White (2001)

The pass-band of the FP is given by:

$$A(x) = \left(1 + \frac{4F^2}{\pi^2}\sin^2 x\right)^{-1}, \tag{5.5}$$

where, $F = (\pi/\sqrt{R})/[(1-R)^2]$ is the reflective finesse, and R is the reflectivity. The argument x is given by

$$x = \frac{2\,\pi\,\mu\,d\cos\theta}{\lambda}. \tag{5.6}$$

5.2.2 The Lithium Niobate FP

$LiNbO_3$ is a birefringent crystal, *i.e.* light after passing through this crystal, gets split into the ordinary beam (o) and the extraordinary (e) beam, *i.e.* there are two sets of channels each with refractive indices μ_o and μ_e that satisfy Equation 5.3. The two beams are linearly polarised in mutually orthogonal directions. The FP that we have used in HaDI has a y-cut crystal with a thickness of 160 μm, *i.e.* the plane of the crystal is perpendicular to its y-axis. $LiNbO_3$ is an electro-optic crystal, *i.e.*its refractive index can be changed by applying a voltage across the crystal. This property of the crystal is used in our telescope to tune the FP at different wavelengths.

The $LiNbO_3$ FP has been extensively used for varied purposes in solar physics primarily because of its fast tuning capability at any desired position along a spectral line. Rust (1985) and Burton, Leistner, and Rust (1987) have investigated the use of $LiNbO_3$ in an imaging spectrophotometer for the study of solar oscillations. Bonaccini and Smartt (1988) have shown that $LiNbO_3$ is an excellent material to observe emission lines in the solar corona. This crystal has also been used in a solar video magnetograph that provided near simultaneous observations of photospheric longitudinal magnetic field, Hα, and photospheric Ca I line at 6122 Å (Mathew, 1998; Mathew *et al.*, 1998; Debi Prasad *et al.*, 1998). It is also used for spectroscopic studies of the Sun (Netterfield *et al.*, 1997; Kentischer *et al.*, 1998).

Due to its electro-optic nature, we are able to change its refractive index, and consequently the centre of the pass-band of its channels, by applying a suitable voltage to it. The calibration of FP was carried out on a spectrograph set up using the 15 cm Coudé telescope at the optics laboratory at USO. A diffraction grating having 1200 lines per mm was used to select the spectral region roughly centred around the Hα line. The grating is blazed at 22° to give maximum efficiency in the 2^{nd} order. A linear dispersion of 17 mÅ is obtained on a Roper Scientific camera having a CCD of size 1368×1016 pixels. An image of the FP channels of the *o*-beam is shown in Figure 5.5. The channel in the centre of the image is less intense than the others because of its proximity to the Hα line centre.

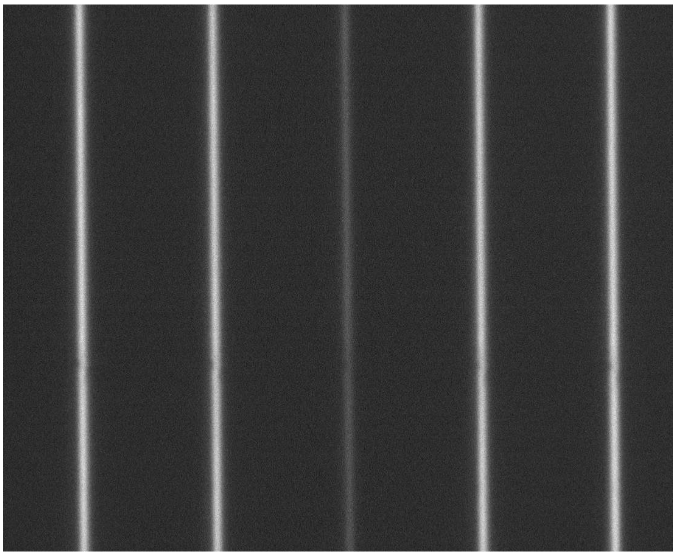

Figure 5.5 Image from the spectrograph showing the FP channels, along the vertical direction, of the *o*-beam. The channel in the centre of the image appears less intense because of its proximity to the Hα line centre.

5.2.3 Calibration of Lithium Niobate FP

We have carried out voltage calibration of the FP for both the channels. This would allow us to apply the correct voltage to centre the FP channel at the desired position along the Hα wings. A preliminary calibration was also done earlier using a different set-up, and is detailed in Joshi *et al.* (2010). For $LiNbO_3$, the *o*-channel is more sensitive to voltage than the *e*-channel (Bonaccini and Smartt, 1988). Thus, the channel that showed larger wavelength shifts with voltage was identified as the *o*-channel. A polariser was used to select the *o*-channel at one time, and the *e*-channel the second time to conduct the calibration. Voltage was applied to the FP in the range -2500 to $1000\,\mathrm{V}$ in steps of $50\,\mathrm{V}$. The shift in wavelength as a function of the applied voltage is shown in Figure 5.6.

A high voltage power supply from *Applied Kilovolts*, that is capable of producing up to $\pm 5000\,\mathrm{V}$, was used for this purpose. To avoid a possible damage to the FP due to very high voltage, its range has been restricted to $\pm 2500\,\mathrm{V}$. The power supply is controlled by a low voltage input ranging from -10 to $+10\,\mathrm{V}$. A sudden application of high voltage may damage the $LiNbO_3$ wafer. To prevent this, voltage is applied in steps of $10\,\mathrm{V\,ms^{-1}}$. A 16-bit digital-to-analog converter and the required software, with a voltage resolution of $1\,\mathrm{V}$, is developed at USO (Mathew and Gupta, 2010).

We also need to exactly determine the voltage necessary to centre the FP on the Hα line centre. For this, maximum transmitted intensity of the FP *o*-channel that crossed the Hα line was observed, as successively higher voltages were applied to it. As this channel crossed the Hα line, the maximum intensity varied in the same manner as that of the Hα line itself, as shown in Figure 5.7. On fitting a Gaussian function to the intensity, we obtain the voltage where intensity transmitted through the FP channel is minimum. From Figure 5.7, we find that this voltage is $-652\,\mathrm{V}$.

The FSR of the FP is determined for the *o* and *e* channels. In order to centre the FP at any desired spectral position, the FP channels have to be shifted by at most half the FSR. The voltage corresponding to this shift is the *half FSR voltage*, which roughly is a measure of the highest voltage that needs to be applied to the FP. Table 5.1 gives these values for the $LiNbO_3$ FP for the *o* and *e* channels.

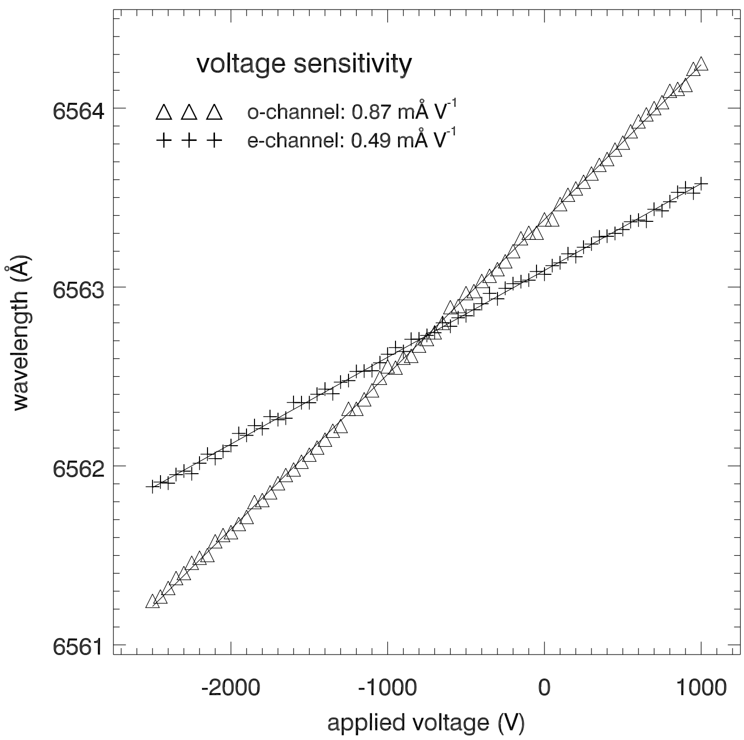

Figure 5.6 Shifts in wavelength as a function of the applied voltage to the o and e channels from -2500 to $1000\,\mathrm{V}$. The o-channel ($\triangle$) is more sensitive to voltage than the e-channel ($+$), as seen from the slope of the two lines.

	o-channel	e-channel
FSR (Å)	3.72	3.88
pass-band (Å)	0.25	0.26
voltage sensitivity ($\mathrm{m\AA\,V^{-1}}$)	0.87	0.49
half FSR voltage (V)	2137	3959

Table 5.1 Properties of the o and e channels of the $LiNbO_3$ FP.

5.2.4 Preliminary Observations

I present here Doppler observations recorded on 2011 November 18 using the HaDI. Voltage was applied to the FP from 0 to $-1000\,\mathrm{V}$ in steps of $50\,\mathrm{V}$, and the image was recorded at each step. A filament was present close to the south-east solar limb near NOAA active region 11354. When no voltage was applied to the FP,

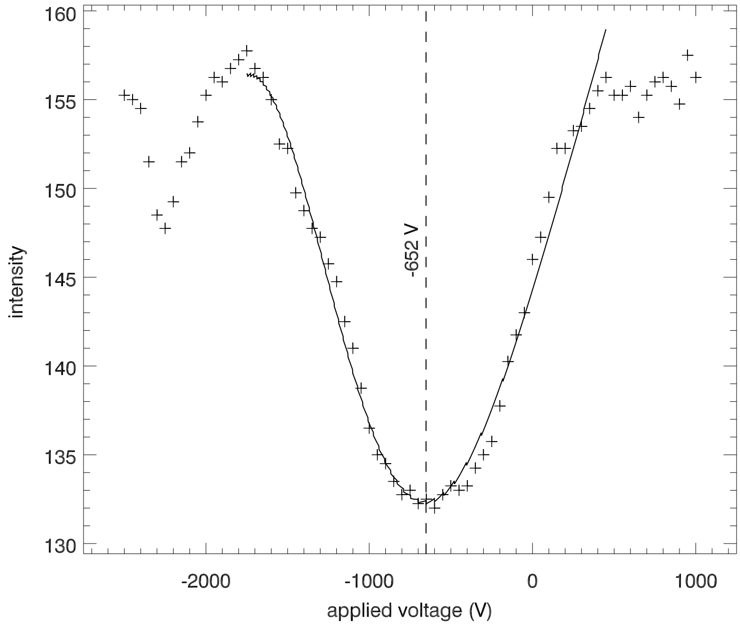

Figure 5.7 Maximum transmitted intensity, in arbitrary units, of an FP *o*-channel that crossed the Hα line. The minimum of the Gaussian fit to the observed intensity corresponds to the point where the channel is centred on Hα line centre, which is at -652 V.

only the bright plage region could be seen, but no features in Hα were visible. As voltage was applied gradually, off-band features started to appear at around -300 V, which are the chromospheric features seen in the wings of Hα line. The filament could be viewed clearly when the voltage was around -650 V. On further applying voltage, the filament ceased to be seen, and no chromospheric features could be observed at -1000 V.

From Figure 5.7 we know that the FP is centred on Hα line at -652 V. Hence, we consider the image at -650 V to be at the Hα line centre, the error being 1.7 mÅ. Figure 5.8 shows three images with the voltages of -400 V (left), -650 V (centre), and -900 V (right) applied to the FP. Since the sensitivity of the FP is 0.87 mÅ V^{-1} (Figure 5.6 and Table 5.1), the image at -400 V is at $\lambda_0 + 218$ mÅ, *i.e.* in the red wing, and the one at -900 V is at $\lambda_0 - 218$ mÅ, *i.e.* in the blue wing. λ_0 is the wavelength of the Hα line centre.

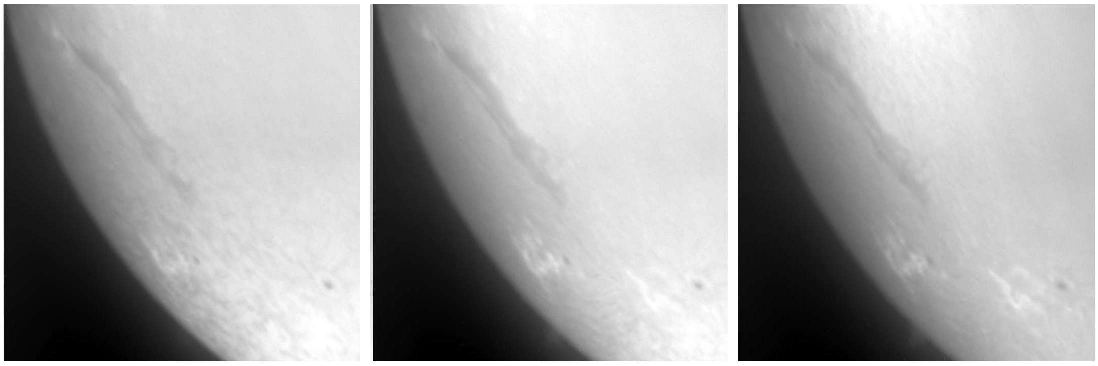

Figure 5.8 Hα images red wing (left), line centre (centre), and blue wing (right). The images in red and blue wings are separated from the line centre by 218 mÅ.

We generated the Hα line profile by taking the average intensity over a quiet region of the Sun. The normalised intensity as a function of different values of the applied voltage is shown in Figure 5.9. A Gaussian fit to the average intensity shows that the minimum occurs in the image taken at −550 V. The difference in

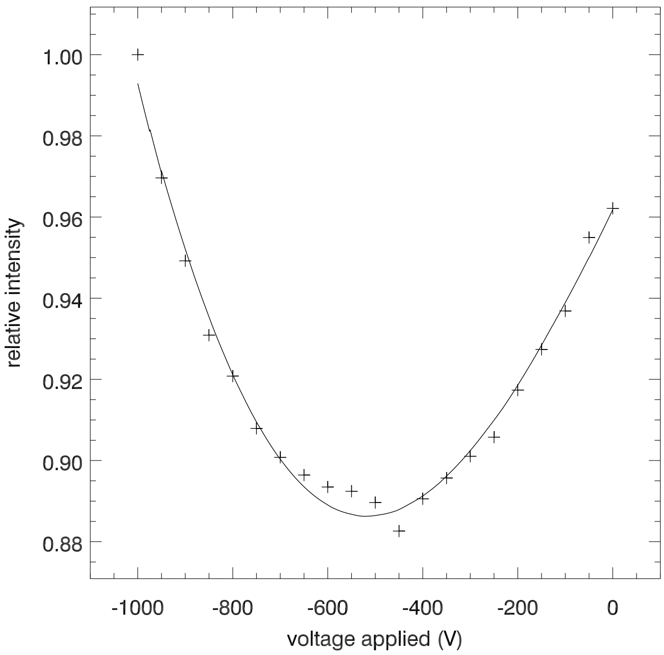

Figure 5.9 The variation of average intensity over a quiet region of the Sun as a function of voltage applied to the FP from 0 to −1000 V. The curve shows a Gaussian fit to the average intensity.

voltage at minimum intensity might be because of change in the angle of incidence of the beam over the FP and pre-filter.

Present Status

The observations presented above are only preliminary in nature, and there are a few improvements that need to be made before the telescope can be used for regular observations. We need to develop a robust guiding mechanism for the telescope that minimises image motion during observations. The images in Hα line centre and wings presented above are raw images, and have not been dark-subtracted and flat-fielded. We need to build an automated routine to record dark and flat frames before regular observations commence. Reliable Dopplergrams can then be obtained by taking voltage scans across the Hα line profile.

5.3 Automatic Detection of Filaments

We have deomnstrated above that the HaDI is capable of observing the activation of filaments by means of Doppler scans in the wings of Hα line. In order to fully exploit the capability of this instrument we have developed an algorithm for automatic detection of filaments on the solar disc. This algorithm can not only identify filaments in Hα images, but also track them through an entire day of observation. It provides physical parameters of the tracked filaments, namely, total area in pixels, length in pixels, and the number of fragments. We have applied this algorithm to several filaments that disappeared and also those that did not, observed on ten different days using images from different ground-based solar observatories. A more extensive study of the same kind would allow us to to establish a threshold value for the above parameters that would tell us with minimum uncertainty whether a filament would disappear.

With the advent of several ground-based telescopes as well as space-borne instruments, and the ever-increasing storage capacities of digital media, an objective automated detection facility of solar phenomena is the need of the hour. The past decade has seen several researchers focusing on this aspect of solar observations (Preminger, Walton, and Chapman, 2001; Qu *et al.*, 2003; Zharkova *et al.*, 2003; Robbrecht and Berghmans, 2004; Curto, Blanca, and Martínez, 2008). They have devised new techniques to achieve an automated detection system for identifying solar features like sunspots, CMEs, prominences, etc., and have also adopted techniques successfully used in other fields.

Gao, Wang, and Zhou (2002) have used an algorithm that detects filament disappearances to carry out a statistical analysis of filaments observed from BBSO. They were able to identify disappearing filaments as a function of their latitudes over the entire year 1999. Shih and Kowalski (2003) have employed advanced local thresholding technique and morphological operations to detect filaments efficiently. Bernasconi, Rust, and Hakim (2005) have also developed an algorithm that detects filaments, traces their spine, and determines the chirality from the orientation of barbs with respect to the spine. Zharkova and Schetinin (2005) have made use of the artificial neural network technique for identifying filaments, wherein two hidden neurons and an output neuron learn to distinguish between the background and the filament. Fuller, Aboudarham, and Bentley (2005) have presented a filament-detection method, which also uses various image segmentation techniques for Hα spectroheliograms. Qu *et al.* (2005) have made use of a nonlinear, multiscale, filtering technique, the stabilised inverse diffusion equation, along with morphological operations to detect filaments and their disappearance.

We have developed a filament detection technique for full-disc Hα images that is primarily based on intensity thresholding. Images from the entire day are first pre-processed so that the algorithm can be uniformly applied to all of them. The actual filament detection algorithm is divided into two parts: extraction and identification. Locations of filaments are identified on the Hα image and stored in a binary image in the extraction part. While the identification part determines the total number of filaments, and attributes for each individual filament.

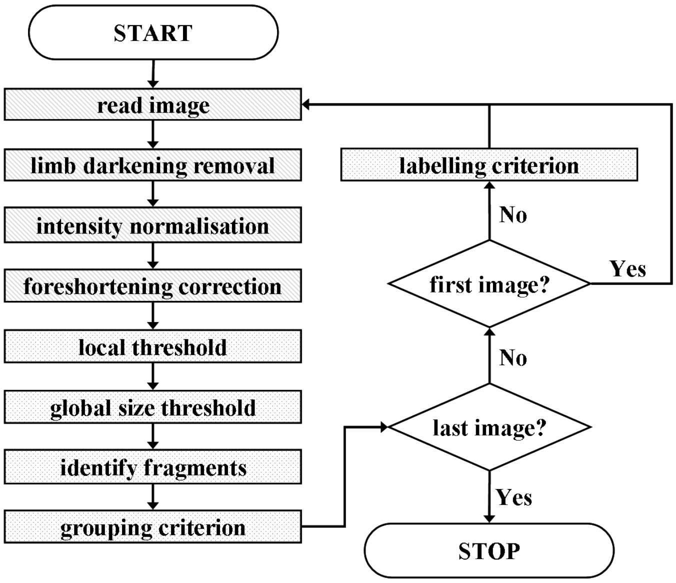

Figure 5.10 Flowchart of the automatic filament-detection algorithm. Image reading, removal of limb darkening, and foreshortening form the pre-processing steps, whereas, the local and global thresholding, identification of fragments, and the grouping criterion constitute the filament extraction steps.

5.3.1 Data Reduction

We have used full-disc time-lapse Hα images of ten different days, observed from Big Bear Solar Observatory (BBSO), Mauna Loa Solar Observatory (MLSO), Kanzelhöhe Solar Observatory (KSO), and USO to test the algorithm. The algorithm is summarised with the help of a flowchart in Figure 5.10. Prior to the application of the filament-identification algorithm, the images are flat-fielded and dark-corrected, and the following pre-processing steps are carried out. For the purpose of illustration of the algorithm and its results, we make use of observations of a filament from KSO taken on 2005 January 5, in this chapter.

Solar Disc Alignment

Solar images require registration to correct for errors in telescope tracking. In order to analyse the full-disc images in sequence, it is necessary to bring the solar disc in each of them at a fixed position, preferably at the centre of the image. To achieve this, we have developed an algorithm that detects the solar limb. Derivatives along several rows and columns are computed, and the inflection point is considered as a point on the edge of the disc, because of the steep intensity gradient between the bright solar disc and the dark sky. The centre and radius of each image are then determined, since three non-collinear points uniquely define a circle. The images are shifted in order to bring the solar disc to the centre. This method is much simpler compared to the manual registration of images.

Limb Darkening Removal

When the Sun is observed in Hα line, we observe deeper layers of solar atmosphere at normal incidence, *i.e.* near disc centre, while closer to the limb, shallower layers are observed. Since, formation of the Hα line depends on the depth at which we are observing, the limb appears darker that the disc centre when seen in Hα. This phenomenon, known as the *limb darkening*, is a major issue while defining a threshold for detection of filaments (Pierce and Slaughter, 1977; Neckel and Labs, 1994).

To correct for this effect, the average centre-to-limb variation (CLV) is determined for each image. Treating the solar image in rectangular polar coordinates, CLV was found in angular intervals of 0.5°. A fifth order polynomial was fitted to the average CLV, and a full-disc image was recreated using this polynomial function with the same radius and centre as the input image. The input image was then divided by this image to obtain an image without any limb darkening.

Normalisation

The overall intensity of the observed images can vary due to various reasons such as sky transparency and zenith angle of the Sun. It is necessary to bring them to a constant level of intensity, after which comparison between them can be handled in a convenient and uniform manner. Hence, we use the *normalisation* procedure, which brings intensities of all the images within the same range.

$$I_{norm} = \frac{I_{in}}{I_{quiet}} \tag{5.7}$$

where, I_{in} and I_{norm} are the input and output image intensities respectively, and I_{quiet} is the average intensity of the quiet Sun in a region 100×100 pixel^2 wide close to the disc centre, obtained after the removal of limb darkening. After this step, the images lie within about the same range of intensity, and the quiet Sun intensity is more or less equal to unity.

Foreshortening Correction

A feature present close to the limb appears smaller on the disc than its actual size on the Sun because of the spherical nature of the solar surface. This is known as *foreshortening*. This needs to be corrected if the filament sizes are to be determined accurately. The correction is given by (Shih and Kowalski, 2003):

$$r' = \sqrt{1 - \sqrt{1 - r^2}}, \tag{5.8}$$

where, r is the fractional radius in the original image and r' is the fractional radius in the corrected image. From Equation 5.8 we see that $r' < r$, however, the area surrounding r' is more than the area surrounding r. Thus, it is not sufficient to simply map intensity at a distance r to a distance r'. To preserve the area, the following transformation given by Enger *et al.* (1966) and Ambastha and Bhatnagar (1988) is used.

$$A_{corrected} = \frac{A_{apparent}}{0.2\,r + \sqrt{1 - r^2}} \tag{5.9}$$

Here, as before, r is the fractional solar radius. Thus, when the correction is applied, an area $A_{apparent}$ located at a distance r is rebinned to area $A_{corrected}$ and placed at a distance r'.

From Equation 5.9, we can see that as we approach the limb ($r \rightarrow 1$), $A_{corrected}$ goes as r^{-1}, and at $r = 1$, $A_{corrected}$ grows to five times $A_{apparent}$. In such a case, even after rebinning, there are a few pixels on the corrected solar disc which cannot be mapped onto. To address this issue, we have carried out the correction only out to $r = 0.9$. This is justifiable, since, no filament of our interest is located so close to the solar limb.

5.3.2 Filament Extraction

I would explain in brief the methods used by some other researchers before describing the algorithm that we have used for extracting the filaments in Hα images. These are mathematical morphological tools that are used to extract various shapes based on some a priori knowledge of the targets. The operations *erosion* and *dilation* are fundamental in morphological processing of images. They are defined in terms of the standard notations used in set theory. Let A be an image and E be a structuring element (SE), then the erosion and dilation, denoted respectively by $\ominus$ and $\oplus$ are defined by:

$$A \ominus E = \{z \,|\, (E)_z \subseteq A\} \tag{5.10}$$

$$A \oplus E = \{z \,|\, (\hat{E})_z \cap A \neq \emptyset\} \tag{5.11}$$

That is, erosion of A by E is the set of all points z such that when E is centred at z, it lies completely within A. While dilation of A by E is the set of all points z such that when $\hat{E}$, the reflection of E, is centred at z, at least one of its element lies inside A. As can be seen from the formula, erosion is a shrinking or thinning operation, as it places stronger constraint through the $\subseteq$ operation, whereas dilation is a growing or thickening operation, since only one element of the SE has to lie within A. The SE, E, is usually small in area compared to the image, A, and is chosen based on the target to be extracted (Gonzalez and Woods, 2002). The SE is generally symmetric, and its centre is positioned at every point of the image, hence, in such a case we would have $E = \hat{E}$.

Based on these two fundamental morphological operations, we have the operations of *opening* and *closing*, denoted respectively by $\circ$ and $\bullet$, defined for an image A and SE E by:

$$A \circ E = (A \ominus E) \oplus E \tag{5.12}$$

$$A \bullet E = (A \oplus E) \ominus E \tag{5.13}$$

Opening and closing thus simply involve a change in order while applying the basic operations of erosion and dilation. In general, closing fuses narrow gaps between closely spaced objects, while opening removes thin protrusions in an image.

To extract solar filaments from Hα images, Shih and Kowalski (2003) as well as Fuller, Aboudarham, and Bentley (2005) have made use of opening and closing. However, on using these methods, it was observed that the area of the filament was not preserved. A filament may exist in the form of a number of broken fragments, especially when it is in an activated state. The broken fragments were found to merge on application of morphological closing. To be able to detect activated or disappearing filaments, it is advisable to maintain the filament area as accurately as possible. Therefore, in our study, we have used the region growing method via a rigorous algorithm, where each contiguous group of pixels obeying a certain criterion is checked to decide if it is a filament fragment.

Intensity and Size Threshold

This process involves comparing the intensity of each pixel of the image with an *intensity threshold* to determine if the pixel belongs to the filament (1 or white) or to the background (0 or black), as described in Equation 5.15. We have used the variable local-thresholding method described in Gonzalez and Woods (2002) and Shih and Kowalski (2003) for this purpose. The first step is to calculate the median at every pixel in the image over a 19×19 neighbourhood centred on the pixel, denoted as $med_{19}(x, y)$. A lower cutoff value (I_{inf}) and a higher cutoff value (I_{sup}) are selected, which are respectively 10% and 90% of the total intensity range of the image. If the median value at a pixel is less than or equal to I_{inf}, the threshold is I_{inf}, and if it is greater than or equal to I_{sup}, the threshold is I_{sup} (Equation 5.14). If the pixel intensity lies in between I_{inf} and I_{sup}, the threshold is equal to the median value calculated in the previous step (Shih and Kowalski, 2003).

$$T_{xy} = \begin{cases} I_{inf} & \text{for} \quad med_{19}(x, y) \; < \; I_{inf} \\ med_{19}(x, y) & \text{for} \quad I_{inf} \; \leq \; med_{19}(x, y) \; \leq I_{sup} \\ I_{sup} & \text{for} \quad med_{19}(x, y) \; > \; I_{sup} \end{cases} \tag{5.14}$$

Once the threshold, T_{xy}, is calculated, the intensity at each pixel in the image, $f(x, y)$, is compared with it to obtain the image $g(x, y)$:

$$g(x, y) = \begin{cases} 1 & \text{for } f(x, y) \; > \; T_{xy} \\ 0 & \text{for } f(x, y) \; \leq \; T_{xy} \end{cases} \tag{5.15}$$

Here, $g(x, y)$ is a binary image in which very bright regions are marked as white, and very dark regions, which also include areas of the image outside the solar disc, are marked as black; while the rest of the image is marked black or white based on the threshold calculated in Equation 5.14.

However, the image also contains some features that when compared with the original image, are seen to be not filaments, but the intensity is similar to that of filaments, such as the granular pattern in chromosphere. We found that these regions are typically less than 12 pixels in size, and hence a size threshold is applied where contiguous white regions less than 12 pixels in size are turned to black.

This leaves us with a binary image in which all of the filaments are identified, but it may also include other features such as the dark sunspots. In order to remove them, we make use of the intensity of the greyscale image at the positions

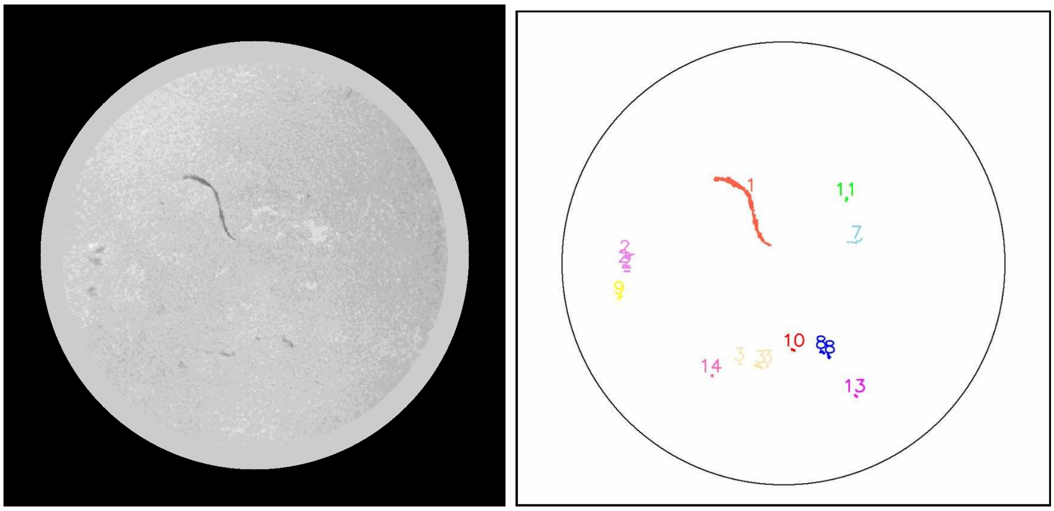

Figure 5.11 Left panel: An image from KSO on 2005 January 5 after applying the pre-processing steps. Right panel: The corresponding binary image after applying the intensity and size thresholds. The black circle marks the solar limb. Filaments are assigned the labels and colours in decreasing order of their total number of pixels.

of the regions identified in the previous step. Sunspots are usually darker than the filaments, thus we can get rid of them with a further global intensity threshold (Shih and Kowalski, 2003; Mathew *et al.*, 2007). We have selected this threshold to be 30% of the disc centre intensity of the normalised images.

Filament Identification

Single large filaments can be considered to be broken into several small fragments. The image obtained after thresholding also contains several such regions. We employ the *grouping criterion* to identify fragments belonging to a single filament. Here, the largest fragment is labelled 1 and is compared with all the other fragments to check if the two lie within a certain distance from each other. Any fragment thus identified lying close to fragment with label 1 is also labelled 1. Such a fragment is then compared with all the remaining fragments to check if it lies within the fixed distance from any of those. Once fragment 1 is compared with all the other fragments, the next largest fragment is labelled 2. This process is repeated for all the fragments present. The fixed distance was taken to be 40 pixels for images from

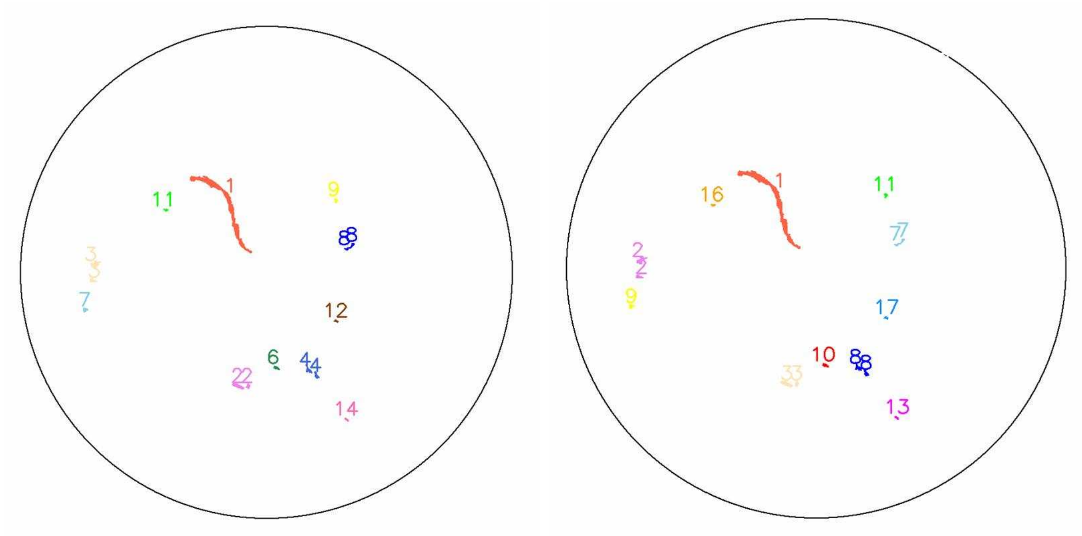

Figure 5.12 Left panel: The binary image for an image from KSO taken on 5 January 2005 subsequent to the one shown in the left panel of Figure 5.11. Before applying the labelling criterion the labels are incorrect as compared to the right panel of Figure 5.11. Right panel: The image with correct labels after applying the labelling criterion. Note that the newly identified fragments are assigned new labels.

USO on which the algorithm was tested for the first time, following the procedure adopted by Gao, Wang, and Zhou (2002) for BBSO images. The different image sizes of different observatories were corrected by taking into account the platescale (arcseconds per pixel) of the image.

At the end of this step, we get a binary image, as shown in the right panel of Figure 5.11, with all of the filaments identified as differently coloured regions. To increase the visibility, the background is turned into white and, in order to illustrate the capability of the algorithm the identified filaments are shown in different colours instead of black. The left panel in Figure 5.11 shows the pre-processed image used for filament extraction, which was observed on 5 January 2005 from KSO.

Filament Tracking

In order to track the filament across all of the images on a given day, it is necessary to retain the labels. For the next image in the sequence, the filament identification step remains the same, at the end of which appropriate fragments would be grouped into filaments, and identified with unique labels. However, fragments change their shape as well as size over time. As per the grouping criterion discussed above, the filaments are labelled based on the sizes of their largest fragments. Thus the labels for the next image may be different from those in the previous image. Therefore, we have used the *labelling criterion*, where filaments of the new image are compared with filaments of the previous image. If they are found to lie within a certain distance from each other, the filament label of the original image is assigned to the corresponding filament of the new image. Taking into account the new fragments appearing in images, or multiple fragments merging to form a single fragment, we find that a critical distance of 15 pixels works satisfactorily for images from USO to keep track of a given filament. For images from other observatories, we have applied this step by considering the corresponding platescale.

Figure 5.12 shows an example of the performance of the labelling criterion. The left panel shows an image from KSO taken on 5 January 2005, subsequent to the one shown in Figure 5.11. The labels assigned to filaments in the two images are not the same because of variations in the size of the fragments. The image after applying the labelling criterion is shown in the right panel. All the filaments seen in Figure 5.11 are assigned the same labels in Figure 5.12 (right), while newly identified filaments in this image are assigned new labels.

Algorithm Output

The algorithm ends after operating on all of the images. For every unique filament that is detected, a corresponding output file is written in ASCII format. The file gives the total area (in pixels), number of fragments, total length (in pixels), and also the median position of the filament (in pixels), for each image analysed. This file shows the overall evolution of a filament throughout the sequence of images.

It is possible to set a threshold for the area of the filaments, *i.e.* if the area increases or decreases by more than 25% of the average size of the filament over a day, then a warning message will be issued. Thus it is possible to keep track of activation of filaments.

In addition, information of all the filaments in an image is stored in two two-dimensional numerical arrays, and one can save such arrays for all the images. The first array contains coordinates of the pixels in all the fragments, while the second one groups the fragments into filaments, and contains sizes and lengths of the fragments. These can be later used to study the temporal evolution of the filaments identified. They can also be used to generate coloured figures for the filaments as shown in Figures 5.11 and 5.12.

Computing Time

The entire filament detection and tracking algorithm was developed using Interactive Data Language (IDL$^{\mathrm{TM}}$), version 6.3 on a regular desktop computer (CPU rate: 3 GHz; RAM: 2 GB) at USO. On average it required one minute of processing time for one image. We will be operating the HaDI at a cadence of around one image per minute. Thus the algorithm is well suited to be operated in real-time for giving a warning of a possible filament eruption.

5.3.3 Results of the Algorithm

In order to test and validate the algorithm, we have studied ten events of partial or complete filament disappearances over the past solar cycle 23. For this, we have taken the full-disc Hα observations from MLSO, BBSO, KSO, and USO. In order to test the algorithm rigorously, we aimed at identifying and tracking not only the disappearing filament for each day, but also all the other filaments present on the solar disc. Table 5.2 gives a summary of the performance of the algorithm for all the filament disappearance events analysed. The date for each event and observatory from which images for that day were used are shown in columns 1 and 2, respectively. Column 3 shows filaments that can be observed visually, and column 4 shows the number of filaments successfully detected and tracked by the algorithm for the entire duration of observations. Columns 5 and 6 similarly deal with sunspots, but detection of a sunspot by the algorithm is undesirable and hence is counted as a false identification. Lastly, column 7 gives the percentage of successful hits, *i.e.* fraction of the number of filaments that were successfully detected.

Date	Data	Observed filaments	Tracked filaments	Observed sunspots	False detections	Hits (%)
1999 Oct 17	MLSO	6	5	3	0	83
2000 Feb 09	BBSO	9	6	1	1	67
2001 Mar 15	MLSO	12	10	0	0	83
2001 Aug 01	BBSO	11	10	1	0	91
2001 Aug 14	MLSO	7	4	2	1	57
2002 Jun 06	MLSO	10	8	2	0	80
2002 Sep 05	MLSO	7	6	0	0	85
2004 Aug 27	BBSO	6	5	2	1	83
2005 Jan 05	KSO	4	4	0	0	100
2008 Apr 26	USO	3	3	0	0	100
Total		75	61	11	3	81

Table 5.2 Summary of the filament disappearance events analysed by the algorithm.

The selection of the events was made so as to cover the whole solar cycle. This would allow us to see the performance of the algorithm during the time when there are few filaments and almost no sunspots, as well as when there are several filaments and sunspots on the disc. The years 1999 and 2000 were marked by the ascending phase of the solar cycle 23, while the year 2001 and 2002 saw its peak during which the Sun had many filaments and active regions. The 2004 – 2008 period was marked by the descending phase of the solar cycle. We can see from the table that the algorithm could identify most of the filaments, and distinguish them from the sunspots. Even during the peak of solar activity, the active-region filaments surrounded by bright plages and dark sunspots were effectively detected and tracked by our code. Furthermore, we observed thin clouds in most of the

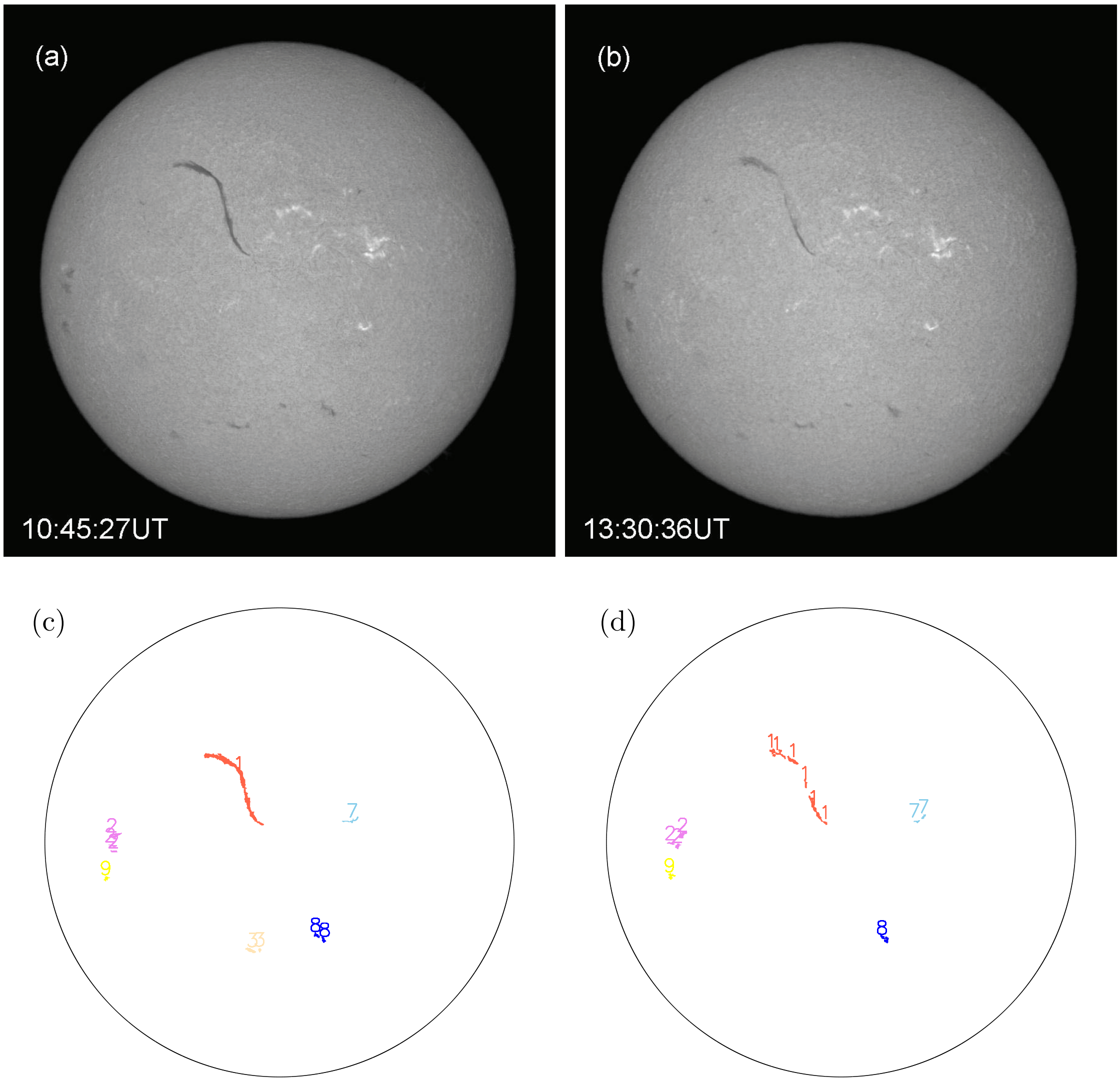

Figure 5.13 (a) and (b) Hα images from Kanzelhöhe Solar Observatory, for 2005 January 5 showing the rapid eruption of the filament. (c) and (d) The output from the algorithm showing labelled filaments at the respective times.

images for 2000 February 9, while images for 2004 August 27 showed an intensity gradient in the East-West direction, even after the pre-processing, which can be attributed to improper flat-fielding. Table 5.2 shows that the algorithm is quite successful in detecting filaments for both these dates. However, because the intensity is not uniform over the image, the method we use to remove the sunspots tends to go wrong resulting in false detection of sunspots in these images.

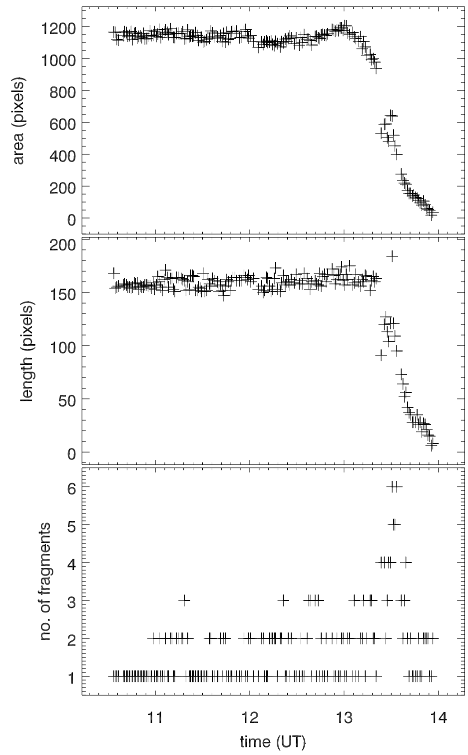

Figure 5.14 Total area (top panels), total length (middle panels), and number of fragments (bottom panels) of the filament observed on 5 January 2005 from KSO.

The top two panels in Figure 5.13 show the filaments on 2005 January 5 at different times, while the bottom two panels show the corresponding colour-coded binary images obtained from the algorithm. The long thick filament, labelled 1 and shown in red colour, erupted very rapidly in a time span of less than an hour. We can see its appearance as single continuous filament in Figure 5.13(c), and then broken into seven fragments in Figure 5.13(d). Figure 5.14 (left) shows the total area, total length and the number of fragments of the same filament. We can see here that the area and length of this filament remains almost constant for most of the time. It is only over the last 50 minutes that the filament decreases in area and length, and it subsequently disappears. From the plot we can also say that the disappearance began at 13:06 UT. The number of fragments of this particular filament does not change much for as long as the filament area is constant. However, as the filament starts to disappear, we can see it breaking up into several fragments. However, this number goes down as rapidly as it rises, and at the end there are only a few small fragments left behind (left bottom panel in Figure 5.14).

It should be noted that the algorithm was built keeping in mind our primary interest: the disappearance of on-disc filaments. It is observed that during the disappearance, parts of the filament lose their material. Some of the fragments totally disappear, while some others shrink in size. In this regard, we found that our algorithm fares better than the technique given in Shih and Kowalski (2003), since neither do we lose information on any of the fragments constituting a filament, nor do we fill the gaps between two neighbouring fragments.

This algorithm is capable of routinely cataloguing filaments including the eruptive ones, with their attributes such as location, length, area, and number of fragments. Upon analysing several more filaments, we could establish a criterion for eruptive filaments based on a sudden or gradual change in its observed attributes, hours prior to its complete eruption. Further, we intend to use this algorithm with the newly installed telescope, HaDI. We also plan to use this routine on a near real-time basis on the images recorded by HaDI in order to forewarn of an imminent filament eruption.

Recently Martin *et al.* (2008) presented a broad concept for the build-up to eruptive events which consists of a CME, an eruptive prominence, a cavity around the filament and a flare. This is primarily based on the hypothesis that CMEs are causally linked to the formation, evolution, and maintenance of filament channels and filaments. They suggest various stages in the build-up to eruption. Slow ascent of filaments prior to their eruption is often observed in many eruptive prominences that are associated with CMEs (Joshi and Srivastava, 2011a; and references therein). Our algorithm is capable of detecting, extracting, and tracking filaments, and has been shown to be successful in determining their various attributes. The algorithm will then be used to test the concept of how CMEs are linked to the evolution of filament channels, filaments and the associated magnetic fields.

Chapter 6

High Resolution Doppler Observations from Dutch Open Telescope

In the previous chapters of my thesis, I have focused on observations of the solar prominences at moderate resolution. However, as discussed in § 1.2, they exhibit a lot of interesting aspects of fine-scale features obtained from high resolution observations, which are not explored as widely as those seen in larger scales (Zirker, Engvold, and Martin, 1998; van Ballegooijen, 2004; Lin *et al.*, 2005). In this chapter, I would discuss one of these aspects pertaining to the sudden formation and disappearance of a filament barb, by making use of high resolution observations obtained from the Dutch Open Telescope.

Mackay *et al.* (2010) have divided the filament into three main parts, the spine, the two endpoints and the intermediate barbs. At present, there is no agreement regarding the magnetic structure of the barbs. The generally accepted view is that given by Martin (1998a), where a barb is rooted in parasitic or minor polarity, *i.e.*, the polarity opposite to the dominant photospheric polarity. However, observations also suggest that barbs terminate not in minor polarities, but in polarity inversion lines that divide magnetic elements of minor polarity and those of major polarity (Chae, Moon, and Park, 2005).

Aulanier and Demoulin (1998) proposed a theoretical model known as the 'dip model' of prominences (§ 1.2.2), where the barb too is supported by means of a dip in the magnetic field lines over minor polarity. On the other hand, Karpen *et al.* (2001) have showed that the magnetic dips are a redundant feature, as long as the fine structure of a prominence undergoes continuous evolution.

Furthermore, while Engvold (1998) regards barbs essential for the formation and existence of quiescent prominence, observations show that many active region filaments can be found without barbs. This raises a question on the role barbs play in the stability of filaments. While it is not possible to address all these questions using a single observational data-set, I have presented here the Doppler observations in Hα of a filament barb taken in high resolution.

Prominences are known to exhibit a wide variety of phenomena in small scales, and the fine structure of filaments has been a subject of study for a long time. Menzel and Wolbach (1960) were among the earliest ones to show that filaments display fine threads when seen in high resolution. Engvold (1976) reported that the sizes of the fine structures within a prominence can be as small as $0.5''$. He also observed bright *knots* present in several prominences. Observations from the high resolution ground-based Swedish Solar Telescope (SST) (Scharmer *et al.*, 2003) have been used by Lin *et al.* (2005) to show that the prominence threads could be $0.14''$ in size. Further, Lin *et al.* (2009); Lin (2010) have also observed oscillations in such thin filament threads.

Engvold (1981) observed prominences in the red and blue wings of the Ca II K line (3933 Å), and found elements in the prominence body ranging in size from less than $1''$ to a few arcseconds with a line-of-sight velocity amplitude from 2 to 10 km s^{-1}. Schmieder, Raadu, and Wiik (1991) have found that although the overall structure of filament remains constant over a period of 15 minutes, Doppler observations reveal that the velocities are constantly changing along filament threads. Zirker, Engvold, and Martin (1998) observed what they termed as *counter-streaming* in a filament, *i.e.*, simultaneous flows in opposite directions in closely-spaced threads of the filament. Such mass motions were seen by them to occur in both the spine as well as barbs, although the motions were more conspicuous in the spine. Recently, Zapior and Rudawy (2010) have attempted to determine the three-dimensional trajectories of the knots that are seen in filaments.

Barbs are known to lend stability to filaments. However, their role during the activated stages of a filament in not precisely known. In order to study this aspect of filaments, I have used high resolution observations from the Dutch Open Telescope (DOT). In the first part of this chapter, details of the telescope and the analysis techniques used will be discussed. I had taken observations at the DOT in May and August 2010. Analysis of a filament barb showing activation that was observed on 2010 August 20 will be presented in the later half of the chapter.

6.1 The Dutch Open Telescope

This telescope is situated on the island of La Palma, which is part of the Canary Islands in Spain. It sits on a 15 m high tower which is supported by means of four open steel-tube triangles. The open structure of the tower allows only lateral movement of the telescope floor, but no tilts, even in the face of severe gusts of wind (Rutten *et al.*, 2004). The canopy of the dome opens fully, producing good seeing throughout the day due to even a small wind.

The DOT has a primary mirror of 45 cm diameter having a focal length of 200 cm. At the prime focus, the image size is 18 mm, of which only 1.6 mm, equivalent to $3'$, is selected using a field stop. Thereafter a beam-splitter and multi-wavelength imaging system is used to observe an area approximately $100'' \times 100''$ in size in seven wavelengths of the visible solar spectrum, viz, Ca II H (3968 Å), G-band (4305 Å), blue continuum, Barium (4554 Å), Barium continuum, Hα (6563 Å), and red continuum. With seven cameras dedicated for each wavelength region, images are always recorded simultaneously in all the wavelengths. Dichroic splitters are used to direct the beams towards the cameras, and Lyot filters are used to select the desired wavelength. DOT also has a small co-axially mounted telescope that observes in the Hα line, for the purpose of tracking and guiding.

In this section, I would first describe an offline technique for image restoration, the speckle reconstruction that is carried out for DOT observations. I would also describe in detail the method to obtain line-of-sight (l-o-s) velocity maps from images in several positions along the Hα line.

6.1.1 Speckle Reconstruction

Any image taken using a ground-based telescope appears degraded because of seeing, *i.e.* the image function i is not the same as the measured object function o.

$$i = o \otimes s \tag{6.1}$$

where, s is the optical transfer function (OTF), and $\otimes$ stands for convolution of o with s. The OTF is determined by the fluctuations in the Earth's atmosphere that occur during the exposure time of the image. The purpose of any image reconstruction procedure is to obtain the diffraction limited image, which is the image with the maximum resolution obtainable using the given telescope aperture. Labeyrie (1970); Weigelt and Wirnitzer (1983) were the first ones to propose and use the method of speckle imaging to reconstruct images of stars. The Sun, being an extended object, is a special case. The speckle reconstruction was successfully applied to obtain solar images by von der Luehe (1993).

The name speckle arises from the tiny specks seen in a short-exposure image of a point object. Several such images are recorded in a burst mode, *i.e.* images with a very short exposure time recorded in a short interval of time. Here, it is assumed that during the time taken to record a single image, the Earth's atmosphere remains stable. Additionally, the total time for each burst has to be short enough so that features on the Sun can be assumed to remain static. By combining these short exposure images, and implementing a statistical model of the atmospheric turbulence, the OTF is calculated from which a diffraction limited image is obtained.

The above method, known as broad-band speckle reconstruction, has been implemented at the DOT by Sütterlin *et al.* (2001a). In this method, at least 100 images are recorded within a time interval of 30 s, each with an exposure time less than 14 ms. All frames within a single burst are aligned by cross-correlating them with the sharpest frame. The images are then divided into 1000 overlapping isoplanatic patches, *i.e.* sub-images over which the seeing is assumed to be constant. These sub-images are speckle-reconstructed independently and then stitched back to give the full speckle-reconstructed image.

However, this method is unsuitable if images are required at several line positions along a spectral line. This is because, for constructing Dopplergrams it is desirable that images in the two line positions are taken close together in time. With one burst at each line position requiring about 30 s, images in two line positions would be separated by a large amount in time. Instead, to achieve this objective, the method proposed by Keller and von der Luehe (1992), known as narrow-band speckle reconstruction is used. In this method, a continuum region is chosen close to the spectral line that has to be scanned. At the DOT, a total of 140 images are recorded in the continuum within a time interval of 30 s. The broad-band method as described above is used to reconstruct these continuum images. During the same time, 20 images are recorded in 7 line positions along the spectral line, thus scanning the line in the same time as the 140 continuum images. The OTF obtained for the continuum is then applied to the 7 sub-bursts, each containing 20 line position images, to obtain the reconstructed images along the spectral line (Sütterlin, Rutten, and Skomorovsky, 2001b). This method is very effective since it does not compromise on the reconstructed image quality, and allows us to scan an entire spectral line.

6.1.2 Line-of-sight velocity maps

High resolution observations taken in the chromospheric Hα line reveal a great deal of fine structure in filaments. However, motion of the filament along the l-o-s induces Doppler shift in the spectral line, rendering the filament invisible in the line centre. For this purpose images are taken at several positions along the Hα line by rotating the calcite stages of a tunable Lyot filter. From an image at the line centre with wavelength, λ_0, and 2 images each in the red and blue wings, separated by the same wavelength, $\Delta\lambda$, we have determined the line-shift, λ_{ls}, at each position, using the method described in Lin (2005).

The Hα line is fitted with a Gaussian function of the form:

$$I = I_0 \exp^{-\tau(\Delta\lambda)} \tag{6.2}$$

where, I_0 is the Hα continuum, and the line absorption is given by

$$\tau(\Delta\lambda) = \tau_0 \exp^{-\left(\frac{\Delta\lambda_{ls}+\Delta\lambda}{\Delta\lambda_D}\right)^2} \tag{6.3}$$

In the above equation, τ_0 is optical depth at line centre, and $\Delta\lambda_D$ is Doppler width of the profile. The line shift, $\Delta\lambda_{ls}$, is determined by taking images at $\lambda_0 - \Delta\lambda$, λ_0, and, $\lambda_0 + \Delta\lambda$. From Equation 6.3, the intensities of images at these three positions, denoted respectively by I_-, I_0, and I_+, are

$$I_- = I_0 \exp\left(-\tau_0\, e^{-\left(\frac{\Delta\lambda_{ls}-(\lambda_0-\lambda)}{\Delta\lambda_D}\right)^2}\right) \tag{6.4}$$

$$I_{lc} = I_0 \exp\left(-\tau_0\, e^{-\left(\frac{\Delta\lambda_{ls}}{\Delta\lambda_D}\right)^2}\right) \tag{6.5}$$

$$I_+ = I_0 \exp\left(-\tau_0\, e^{-\left(\frac{\Delta\lambda_{ls}+(\lambda_0-\lambda)}{\Delta\lambda_D}\right)^2}\right) \tag{6.6}$$

On combining the three equations above, τ_0 and $\Delta\lambda_D$ are eliminated (Lin,

2005) to give,

$$\Delta\lambda_{ls} = \frac{\Delta\lambda(1-A)}{2(1+A)} \tag{6.7}$$

where, A is defined as:

$$A = \frac{\log\left(\frac{\log I_0 - \log I_-}{\log I_0 - \log I_{lc}}\right)}{\log\left(\frac{\log I_0 - \log I_+}{\log I_0 - \log I_{lc}}\right)} \tag{6.8}$$

Once the line shift, $\Delta\lambda_{ls}$, is obtained, the l-o-s velocity is:

$$v_{los} = c\frac{\Delta\lambda_{ls}}{\lambda_0} = \frac{c}{\lambda_0}\frac{\Delta\lambda(1-A)}{2(1+A)} \tag{6.9}$$

6.2 Filament Activation on 2010 August 20

Observations were carried out at the Dutch Open Telescope in May and August 2010. From 19 to 27 August 2010 a filament in NOAA AR number 11100 was selected as a target for study, and evolution of its different parts was observed. Since parts of this filament lied outside the active region, it could be classified as an intermediate type. The filament underwent lot of changes in its shape during these days, before ultimately erupting on 2010 August 27 when it appeared just above the west limb of the Sun.

On 2010 August 20 the northern end of the filament developed a barb in around 10 minutes, as seen in Figure 6.1, and disappeared in 35 minutes. Such a rapid formation and disappearance of barb is not very well-known. This prompted us to study this event in detail. Images for this event were recorded in seven line positions of the Hα line, at λ_0 and at $\Delta\lambda = \pm 0.3$ Å, ± 0.6 Å, ± 0.9 Å. The observations of the barb presented here extend from 08:00 UT till 09:55 UT, with a cadence of 30 s. Since the seeing was good in this duration, speckle reconstruction of the images was carried out, which were used for the present analysis.

The small FOV of DOT meant that even minute errors in telescope tracking amplified to produce significant motion between images. To correct for this, an algorithm was developed which determined the correlation between a given image and its subsequent image by applying varying shifts to the next image. The shift which gave maximum correlation between the two images was applied to the subsequent image, and the process was repeated for all the images in all line positions. On running the images in the form of a time-lapse movie, it was possible to observe the changes in the structure of the filament and the barb.

We have also constructed the l-o-s velocity maps using the method as described earlier in the chapter. To make such a map, 3 images, one in line centre, and one each in the red and blue wings are required. Since, we have images in seven line positions, three sets of l-o-s velocity maps could be constructed. Of the three sets, since images at ± 0.3 Å are too close to the line centre image, the changes in intensity were not significant enough to observe the l-o-s velocity. Also, the images at ± 0.9 Å are too far away from the line centre image, thus only sufficiently high velocities could be observed using this set of images. Therefore, we present the results obtained from the l-o-s velocity maps constructed using images at line centre and at ± 0.6 Å.

From Equation 6.7, we find that the continuum intensity is also needed to determine the l-o-s velocity in Equation 6.9. The continuum intensity is determined by taking the average intensity of quiet chromosphere in all the seven line positions

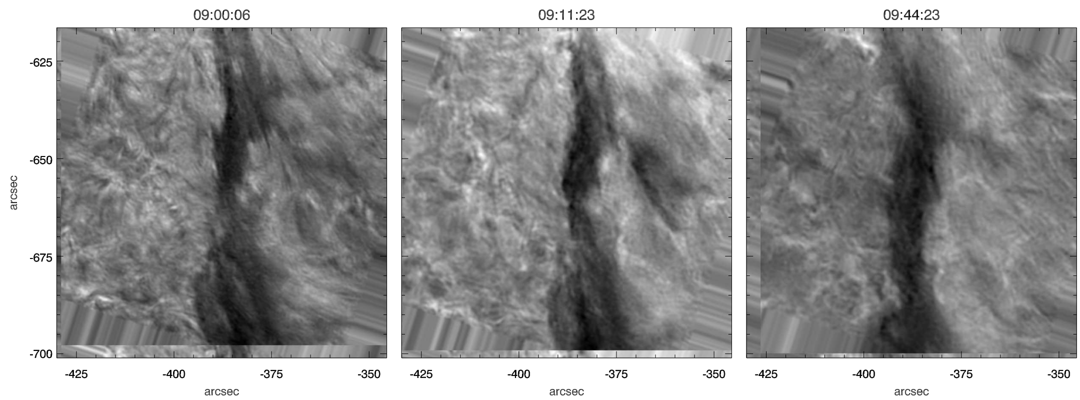

Figure 6.1 Hα line centre images of the filament on 2010 August 20. While the image at 09:00:06 UT, does not show a barb, it is seen to be fully formed at 09:11:23 UT when the observations were resumed. Later it is seen to disappear completely at 09:44:23 UT.

for all the times. On fitting a Gaussian to these seven points for a given time, we regenerate the Gaussian profile of the Hα line. We also know the full-width at half-maximum (FWHM) of the Hα line to be equal to 1.44 Å. Therefore, we take the Hα continuum to be twice the intensity at which the fitted Gaussian function has its width equal to half the FWHM, *i.e.*, 0.72 Å.

To study the filament, in addition to line centre images, and l-o-s velocity maps, we also observed changes in photospheric l-o-s magnetic field by using magnetograms from the Heliospheric Magnetic Imager (HMI) (Scherrer *et al.*, 2011) on board the Solar Dynamics Observatory (SDO) (Pesnell, Thompson, and Chamberlin, 2011). HMI obtains the magnetic field from filtergrams taken in various positions along the Fe I 6173 Å spectral line. For this, it is essential to exactly select the same region of interest (ROI) from the HMI images. Therefore, as an intermediate step we relied upon simultaneous full-disc Hα images from KSO. A feature, that could be seen even in moderate resolution, was identified in the DOT line centre image. Since, the platescale of DOT images is known accurately, it was possible to determine its size in arcsecs. In other words, the DOT FOV, and the location of the feature was known accurately in arcsecs. The same feature was identified in the KSO full-disc images. By taking into account the size of DOT FOV, an ROI was selected from the KSO FOV such that coordinates of the feature were the same as in the DOT FOV. To make sure that the right KSO ROI was selected, KSO FOV was overlapped with contours of DOT Hα line centre image. The coordinates of this ROI are from (-430,-701) to (-345,-616) in arcsec with respect to the disc centre. The ROI is marked on Hα image from DOT and HMI l-o-s magnetogram in Figure 6.2. These coordinates were then converted into heliographic coordinates, and the corresponding ROI from full-disc HMI images was extracted. Thus, we could overlay the HMI contours on top of DOT images to study simultaneous changes in l-o-s magnetic field. The filament under study had very small-scale photospheric magnetic fields surrounding it, hence, to build up the signal and reduce noise, we made use of an average of three consecutive HMI l-o-s magnetograms.

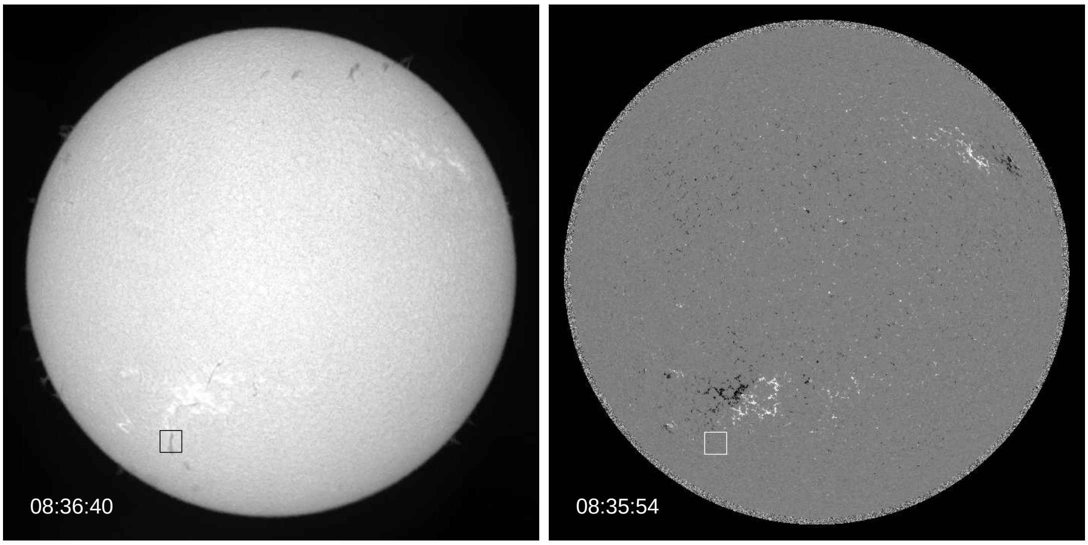

Figure 6.2 Full-disc Hα image from KSO (left) and l-o-s magnetogram from HMI/SDO (right) for 2010 Aug 20. The field-of-view of DOT is marked on both the images using a square.

6.2.1 Observations

I will first describe observations of the filament and the barb using all the sets of observations taken on 2010 August 20. Later I give the possible explanation for the observed evolution of the filament barb. The observations are shown in Figure 6.3 in the form of a mosaic of all the sets of observations at three different times. In this figure, images in Hα line centre, and at $\Delta\lambda = -0.6\,\text{Å}$ are shown to be taken at the same time. This is because the information obtained from the header of the file is for the complete burst at 7 line positions along the Hα line, and not for each position individually. In reality, images taken in the two line positions are separated by about 12 s.

DOT: Hα line centre

The observation of the filament started at 08:00 UT. The line centre images did not show significant changes till almost 09:00 UT. Between 09:00 and 09:11 UT, observations had to be suspended to carry out the routine task of getting dark and flat frames, and refocusing the telescope. On resuming observations at 09:11 UT, a barb had formed at the northern end of the DOT FOV as can be seen in Figure 6.3. Thus, we infer that the barb formed sometime within a short span of 11 minutes from 09:00 to 09:11 UT. This formation of barb could also be seen in the low resolution observations from full-disc KSO images. The barb remained more or less unchanged till about 09:26 UT, after which it started to disappear, and could no longer be seen in the line centre images at 09:45 UT.

DOT: l-o-s velocity maps

The right panels in Figure 6.3 show l-o-s velocity map produced using line centre image, and images at ± 0.6 Å. The colour bar shown adjacent to the images gives the l-o-s velocity component in units of km s^{-1}. From this, we observe that there is no l-o-s velocity seen till 08:30 UT. Later, till 08:58 UT, we could observe upflows in the filament spine with l-o-s velocity ~15 km s^{-1}. These upflows seemed to move towards the location where the barb, that appears later, connects with the spine, *i.e.* from south to north. We term such features having a l-o-s velocity component as moving velocity features (MVFs). Two MVFs were followed in different parts of the filament spine. One MVF observed from 08:30 to 08:40 UT in the lower half of the FOV moved with a transverse component of 18 km s^{-1}, whereas another MVF observed in the upper half of the FOV from 08:39 to 08:46 UT moved with a transverse component of 31 km s^{-1}. It is possible that there is no mass flow in the plane of sky in the filament spine, but adjacent parts of the spine show a l-o-s velocity component in response to some kind of wave passing through the spine, owing to which there appears a transverse component of velocity. To rule

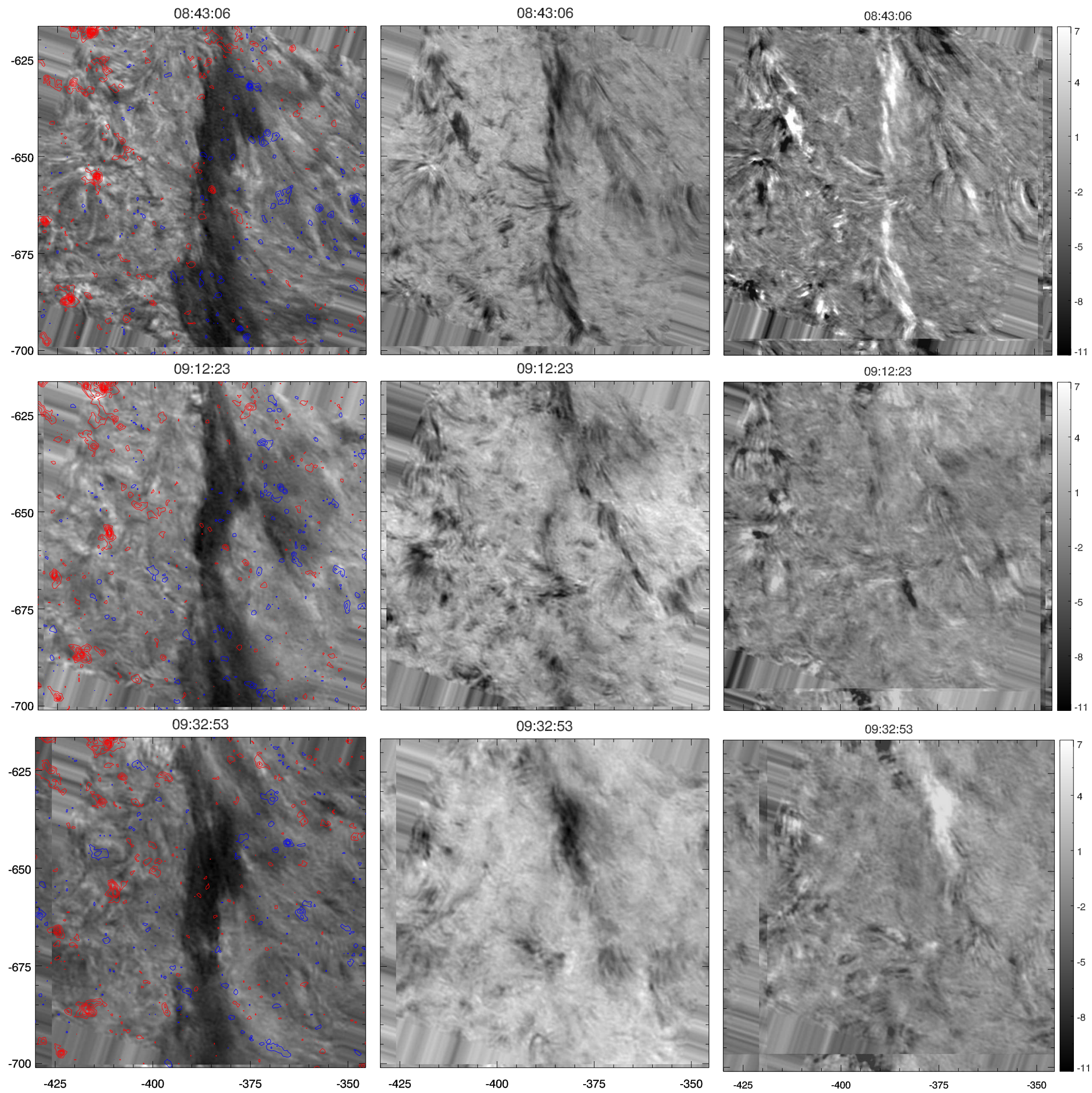

Figure 6.3 A mosaic of images used to study the filament barb on 2010 August 20. *Left*: Overlay of l-o-s magnetograms from HMI/SDO on Hα line centre images from DOT. Red indicates positive polarity, and blue indicates negative. *Middle*: Images in blue wing of Hα at $\Delta\lambda = -0.6\,\text{Å}$. *Right*: l-o-s velocity maps created from Hα line centre, and $\pm 0.6\,\text{Å}$ images. The time for each image is shown at the top. All the axis coordinates are in terms of arcsecs from the Sun centre.

out this possibility, time-lapse movies in Hα line centre were studied carefully, and moving blobs within the filament spine could be observed. Thus, it provides strong evidence of actual mass flowing in the spine in the form of the MVFs.

From 08:51 to 09:00 UT we can see red shift, *i.e.* downflow reaching up to 11 km s^{-1} at the point where the barb connects with the spine. We suggest that this is the mass flowing downward that forms the barb, which initially we can see only in the l-o-s velocity maps, but not in the line centre images. It is only from 09:24 UT onwards, *i.e.* just before the barb starts to disappear, that we see upflows in the barb. We find MVFs in the barb too, just like in spine. These features showed a transverse motion from the barb footpoint towards the spine. One of the MVFs tracked in the barb from 09:24 to 09:30 UT showed a transverse component of 38 km s^{-1}. These MVFs in the barb could be observed till 09:42 UT.

HMI l-o-s magnetograms

The filament was seen to lie along the magnetic neutral line with the negative field dominant on the east side of filament, and positive field dominant on the west side. The barb appears on the west side of the filament spine, and consequently there is little change in the magnetic field on the east side of the spine. The west side shows three concentrations of the dominant (positive) magnetic field at the location of the barb. We have selected an area of $38'' \times 66''$ covering the area of the barb and calculated the total positive and negative flux in this region. Figure 6.4 (left panel) shows the HMI region over which the DOT region is marked with a green square, while the region used to calculate magnetic fluxes is shown using a white rectangle. The positive and negative fluxes within the white rectangle are shown in the right panel.

From this figure, we observe that the positive flux is always more than the negative flux, which is expected since the former is the dominant polarity. From 08:00 UT till about 08:50 UT we find the positive flux increases, while the negative flux decreases, but only till 08:20 UT, then it remains constant up to 09:10 UT.

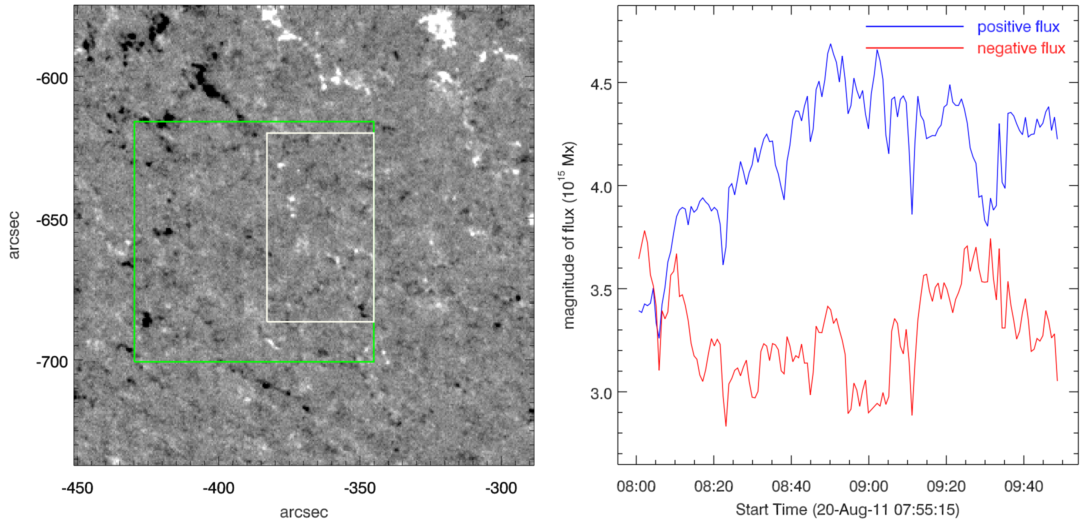

Figure 6.4 Left: A region of HMI l-o-s magnetogram with the DOT FOV marked with a green square. The white rectangle marks the region surrounding the barb location over which flux is calculated. Right: The positive (blue) and negative (red) flux in the region marked using white rectangle.

As the barb starts to appear at 09:00 UT, the positive flux starts to decrease till 09:35 UT. During approximately the same time, *i.e.* from 09:05 to 09:35 UT the negative flux increases. This suggests that although the barb site is populated with dominant polarity before its formation, once it appears, the strength of dominant polarity decreases, and that of the minor polarity increases.

6.2.2 Discussion and Conclusions

Based on the high resolution observations from DOT and HMI described above, we summarise in Table 6.1 the overall picture of formation and disappearance of barb, and the changes taking place in the filament before and after. We suggest that it was the mass flow from spine to the top of the barb that led to barb formation. This can be seen first from the MVFs moving towards the barb location, and later from downflows occurring at the point where the barb connects with the spine. The barb appeared on the west side of filament spine where positive polarity was

Time (UT)	Observational remarks
08:31 – 08:55	blue shifts in spine, $\sim$15 km s^{-1}
	(mass flows towards barb)
08:36 – 08:59	strong red shifts at top of barb, $\geq$15 km s^{-1}
	(mass flows leading to barb formation)
09:00 – 09:11	formation of barb in Hα line centre
09:00 – 09:35	decrease of positive flux around barb location
09:05 – 09:35	increase of negative flux around barb location
09:15 – 09:40	barb disappears in Hα line centre
09:23 – 09:40	strong blue shifts in barb, $\geq$15 km s^{-1}
	(mass flows towards spine)

Table 6.1 Summary of the temporal evolution of rapidly forming and disappearing barb and the changes in filament structure before and after.

dominant. From the flux calculated using HMI magnetograms, we observe that the barb formation was accompanied with decreasing positive flux, and increasing negative flux. Our observation presented here also supports Martin (1998a) who have reported that a barb ends in a minor polarity. However, we are not able to point out the physical process that may have led to the sudden disappearance of the barb.

The present high resolution observations in Hα line centre and Dopplergrams from DOT complemented with near-simultaneously recorded high resolution magnetograms from HMI/SDO provided us a unique opportunity to understand the rapid formation and disappearance of barb of an activated filament on 2010 August 20. Since the filament erupted later, on 2010 August 27, when it was on the western limb, it is essential to point out the importance of such studies of barb stability and their dynamic evolution.

Chapter 7

Conclusions and Future Work

In this thesis, I have addressed several issues pertaining to the morphological and dynamical aspects of solar prominences. The first chapter introduces the topic of my research, discusses the related studies conducted in the past, and also describes some of the unsolved questions. Here, I will summarise results from the rest of the chapters, and later briefly describe a few directions in which I would like to continue my work in future.

7.1 Summary

Chapter 2 In this chapter, I have highlighted some of the earlier studies of dynamics of solar eruptive events in particular CMEs and erupting prominences, and their limitations. All these studies were carried out using observations taken from a single spacecraft. Drawbacks of such measurements were listed, and the need for stereoscopic observations was brought out. The basics of stereoscopic reconstruction were given in brief in § 2. STEREO was the first spacecraft devoted to carry out stereoscopy. Some of the widely used stereoscopic techniques developed for STEREO observations and their results were described in brief in § 3. A few techniques developed before the launch of STEREO were also discussed. In § 4 the stereoscopic reconstruction technique based on triangulation developed by us for EUVI, COR1 and COR2 instruments on board the STEREO spacecraft was discussed in detail. The formulae for obtaining heliographic coordinates were derived by making use of the epipolar constraint to resolve the over-dependence of the system. Errors in the reconstruction techniques were derived, and limitations of different techniques were also pointed out. Lastly, in § 5, our technique was validated by comparing our results with those obtained from well-established IDL™ reconstruction routine, `scc_measure`.

Chapter 3 In the first part of this chapter, I have presented results from a stereoscopic study of two eruptive prominences observed on 2010 April 13 and 2010 August 1, using 304 Å images from EUVI instrument on board the twin STEREO spacecraft. Both the prominences showed a helical structure during their fast-eruptive stage. Like many other prominences these too displayed two distinct phases of eruption, the slow-rise phase and the fast-eruptive phase. A constant value of acceleration was observed for both the events, of about tens of $\mathrm{cm\,s^{-2}}$ in the slow-rise phase, and several $\mathrm{m\,s^{-2}}$ in the fast eruptive phase. The stereoscopic reconstruction revealed that the helical twist for the prominence on 2010 April 13 was in a clockwise direction, while for the prominence on 2010 August 1 it was in an anticlockwise direction. Both the prominences also showed an equatorward non-radial propagation direction. The acceleration in the legs of the prominences during their fast-eruptive stage was found to be commensurate with the sense of helical twist and the non-radial direction, *i.e.* the leg in which the two motions acted in the same direction showed a higher acceleration than the other leg in which the two motions were in mutually opposite directions. Thus, for the first time it is shown using three-dimensional reconstruction that prominences can experience different acceleration in its two legs, which can be explained as a resultant of these two different motions.

We also studied the eruptive prominence on 2008 December 12, which was part of a study carried out with our collaborators Olga Panasenco and Sara F. Martin. The prominence was seen to roll at the top, which was confirmed by the results obtained on reconstructing a feature in the EP observed in 304 Å images from EUVI. This behaviour of the prominence was attributed to the presence of a coronal hole located just north of the prominence. The associated CME also showed non-radial direction of propagation.

Chapter 4 The eruption of solar prominences and CMEs are so closely linked, that a kinematic study involving one but not the other would be incomplete. With this in mind, we undertook a study of six CME and the EPs associated with three of them. Such studies have been a focus previously too, however, almost all of them were carried out using projected measurements. We have used EUVI and coronagraphs, COR1 and COR2 on board the STEREO spacecraft to carry out the first three-dimensional study of acceleration of CMEs and EPs. From our reconstructed acceleration profiles, we find that the maximum CME acceleration occurs at a height of less than $2\,R_\odot$, whereas earlier, this height was estimated to be be in the range of $2-4\,R_\odot$ from projected measurements of acceleration. We thus now have a more accurate upper limit for the height at which most of the CME acceleration takes place.

The bimodal acceleration profile, reported by Chen and Krall (2003), was not observed in EP-associated CMEs, but in only those CMEs that were not associated with EPs. Two of the three prominences in the study showed a high and rising value of acceleration, of $\sim 50\,\mathrm{m\,s^{-2}}$ at a distance of almost $4\,R_\odot$ but the corresponding CME LE does not show the same behaviour. This has a strong implication on the mechanism of CME initiation. All these results are inferred from the six cases studied here. In order to make a more conclusive statement about this behaviour, it is necessary to analyse several more such events using the reconstruction technique, and carry out a statistical investigation of all the reconstructed and associated prominences.

The CME on 2007 December 31, showed acceleration of over $1500\,\mathrm{m\,s^{-2}}$, which is unusually high for a CME associated with a C-class flare, indicating that the energy released in a flare may not be correlated with the energy available to accelerate the CME. Although there are several studies carried out on this strongly accelerating CME, none has focused on this unusual aspect.

We wanted to make a study by employing the 3D reconstruction technique, for which the events observed by the STEREO spacecraft were the most suitable. Thus, inadvertently, we had to select the events occurring in the long and deep minimum of solar cycle 24. One also needs to investigate if the some of the results would be altered if the events belong to the maximum phase of the solar cycle, thereby improving our understanding of the dependence of CME dynamics on the phase of solar cycle.

Chapter 5 We have developed and installed the Hα Doppler Imager (HaDI) at USO premises. This telescope observes in the line centre and wings of the Hα line to observe activation of filaments, and measures the line-of-sight velocity of erupting ones. Some preliminary observations from this telescope are presented. However, a routine observational procedure has not been established at the telescope. This would include recording dark and flat frames two or three times a day. A routine would be developed to take observations at a given cadence at certain positions along the Hα line to obtain reliable Dopplergrams. These could be easily changed by the user depending on the nature of activity occurring on the Sun.

In this chapter, I have also described an automated filament detection algorithm that can detect and track filaments from Hα full-disc solar images from different ground-based observatories. The algorithm computes size, length and the number of fragments of a single filament, for all the images over a given observation day. This algorithm is suitable for real-time monitoring and cataloguing of filaments. In future, we would like to integrate this algorithm on the HaDI to enable a near real-time warning of filament eruption.

Chapter 6 This chapter discusses Hα Doppler observations in high resolution from the the Dutch Open Telescope at La Palma, Spain. The optical and mechanical design of the telescope is given in brief. I have explained the technique of speckle reconstruction, applied on images from DOT, using which effects of the seeing induced by Earth's atmosphere are corrected to provide a diffraction limited image. Later, the method of obtaining line-of-sight velocity maps from images at Hα line centre, and an image each in the red and blue wings of the Hα line, is explained in detail.

In the second part of the chapter, observations of an activated filament barb are discussed. The filament on 2010 August 20 developed a barb in a span of 11 minutes which disappeared in the next 30 minutes. We observe mass flows in the spine to the site where the barb appears later. This is the mass that led to the barb formation. We also observed the simultaneous changes in l-o-s magnetic field from HMI/SDO. The appearance of barb was accompanied by a decrease in the flux of the dominant polarity (positive) and increase in that of the minor polarity (negative). This observation supports the view by Martin (1998a) who have reported that a barb ends in a minor polarity. The results of this study provide and insight into the barb dynamics which are important to understand the overall stability of filaments.

7.2 Future Work

We have developed an algorithm for the detection and tracking of solar filaments. We would like to integrate this algorithm with the HaDI telescope built at USO. By observing several erupting filaments, we aim at arriving at a threshold value of the attributes provided by the algorithm. This would enable us to issue a forewarning of an erupting filament, and – if it is located close to the disc centre – of an Earth-directed CME as well. This is highly desirable for any observing programme dedicated to space weather prediction.

We would also like to make use of this algorithm in conjunction with the stereoscopic results obtained from STEREO spacecraft observations. While the filament detection algorithm would provide attributes observable from ground-based observatories, the three-dimensional reconstruction would provide the true height and dynamics of the filament very accurately. This would help us greatly in establishing a criterion for the eruption of a filament.

The observations from DOT are immensely helpful in revealing the changes occurring on fine-scale in a filament. By constructing line-of-sight velocity maps, we can observe changes occurring along the line-of-sight, and not just in the plane of sky. Simultaneous Doppler and magnetic field observations of a small field in high resolution and in several wavelengths is crucial for understanding the formation and conditions leading to eruption of filaments.

Bibliography

Alexander, D.: 2006, *Space Sci. Rev.* **123**, 81.

Alexander, D., Metcalf, T.R., Nitta, N.V.: 2002, *Geophys. Res. Lett.* **29**(10), 1403.

Ambastha, A., Bhatnagar, A.: 1988, *J. Astrophys. Astron.* **9**, 137.

Antiochos, S.K., Klimchuk, J.A.: 1991, *Astrophys. J.* **378**, 372.

Antiochos, S.K., Dahlburg, R.B., Klimchuk, J.A.: 1994, *Astrophys. J. Lett.* **420**, L41.

Antiochos, S.K., DeVore, C.R., Klimchuk, J.A.: 1999, *Astrophys. J.* **510**, 485.

Aschwanden, M.J., Newmark, J.S., Delaboudinière, J., Neupert, W.M., Klimchuk, J.A., Gary, G.A., Portier-Fozzani, F., Zucker, A.: 1999, *Astrophys. J.* **515**, 842.

Aschwanden, M.J., Alexander, D., Hurlburt, N., Newmark, J.S., Neupert, W.M., Klimchuk, J.A., Gary, G.A.: 2000, *Astrophys. J.* **531**, 1129.

Aschwanden, M.J., Wülser, J., Nitta, N.V., Lemen, J.R.: 2008a, *Astrophys. J.* **679**, 827.

Aschwanden, M.J., Nitta, N.V., Wuelser, J., Lemen, J.R.: 2008b, *Astrophys. J.* **680**, 1477.

Aulanier, G., Demoulin, P.: 1998, *Astron. Astrophys.* **329**, 1125.

Babcock, H.W., Babcock, H.D.: 1955, *Astrophys. J.* **121**, 349.

Bangert, P.D., Martin, S.F., Berger, M.A.: 2003, In: *AAS/Solar Physics Division Meeting #34, Bulletin of the American Astronomical Society* **35**, 815.

Bemporad, A.: 2009, *Astrophys. J.* **701**, 298.

Bernasconi, P.N., Rust, D.M., Hakim, D.: 2005, *Sol. Phys.* **228**, 97.

Bommier, V., Sahal-Brechot, S., Leroy, J.L.: 1981, *Astron. Astrophys.* **100**, 231.

Bonaccini, D., Smartt, R.N.: 1988, *Appl. Optics* **27**, 5095.

Browning, P.K., Priest, E.R.: 1986, *Sol. Phys.* **106**, 335.

Brueckner, G.E., Howard, R.A., Koomen, M.J., Korendyke, C.M., Michels, D.J., Moses, J.D., Socker, D.G., Dere, K.P., Lamy, P.L., Llebaria, A., Bout, M.V., Schwenn, R., Simnett, G.M., Bedford, D.K., Eyles, C.J.: 1995, *Sol. Phys.* **162**, 357.

Burton, C.H., Leistner, A.J., Rust, D.M.: 1987, *Appl. Optics* **26**, 2637.

Calabretta, M.R., Greisen, E.W.: 2002, *Astron. Astrophys.* **395**, 1077.

Cargill, P.J.: 2004, *Sol. Phys.* **221**, 135.

Chae, J., Moon, Y.J., Park, Y.D.: 2005, *Astrophys. J.* **626**, 574.

Chen, J.: 1989, *Astrophys. J.* **338**, 453.

Chen, J., Krall, J.: 2003, *J. Geophys. Res.* **108**, 1410.

Chen, J., Howard, R.A., Brueckner, G.E., Santoro, R., Krall, J., Paswaters, S.E., St. Cyr, O.C., Schwenn, R., Lamy, P., Simnett, G.M.: 1997, *Astrophys. J. Lett.* **490**, L191.

Chen, P.F., Shibata, K.: 2000, *Astrophys. J.* **545**, 524.

Chifor, C., Mason, H.E., Tripathi, D., Isobe, H., Asai, A.: 2006, *Astron. Astrophys.* **458**, 965.

Cremades, H., Bothmer, V.: 2004, *Astron. Astrophys.* **422**, 307.

Curto, J.J., Blanca, M., Martínez, E.: 2008, *Sol. Phys.* **250**, 411.

Debi Prasad, C., Mathew, S.K., Bhatnagar, A., Ambastha, A.: 1998, *Experimental Astronomy* **8**, 125.

Delaboudinière, J., Artzner, G.E., Brunaud, J., Gabriel, A.H., Hochedez, J.F., Millier, F., Song, X.Y., Au, B., Dere, K.P., Howard, R.A., Kreplin, R., Michels, D.J., Moses, J.D., Defise, J.M., Jamar, C., Rochus, P., Chauvineau, J.P., Marioge, J.P., Catura, R.C., Lemen, J.R., Shing, L., Stern, R.A., Gurman, J.B., Neupert, W.M., Maucherat, A., Clette, F., Cugnon, P., van Dessel, E.L.: 1995, *Sol. Phys.* **162**, 291.

Dere, K.P., Brueckner, G.E., Howard, R.A., Michels, D.J., Delaboudiniere, J.P.: 1999, *Astrophys. J.* **516**, 465.

Domingo, V., Fleck, B., Poland, A.I.: 1995, *Space Sci. Rev.* **72**, 81.

Dryer, M.: 1982, *Space Sci. Rev.* **33**, 233.

Eichstedt, J., Thompson, W.T., St. Cyr, O.C.: 2008, *Space Sci. Rev.* **136**, 605.

Enger, I., Podsiadlo, R.D., Jensen, D.C., Ward, F.: 1966, *Air Force Surveys in Geophysics* **178**.

Engvold, O.: 1976, *Sol. Phys.* **49**, 283.

Engvold, O.: 1981, *Sol. Phys.* **70**, 315.

Engvold, O.: 1998, In: D. F. Webb, B. Schmieder, & D. M. Rust (ed.) *IAU Colloq. 167: New Perspectives on Solar Prominences*, *Astronomical Society of the Pacific Conference Series* **150**, 23.

Feng, L., Inhester, B., Solanki, S.K., Wiegelmann, T., Podlipnik, B., Howard, R.A., Wuelser, J.: 2007, *Astrophys. J. Lett.* **671**, L205.

Feynman, J., Martin, S.F.: 1995, *J. Geophys. Res.* **100**, 3355.

Filippov, B.P., Den, O.G.: 2001, *J. Geophys. Res.* **106**, 25177.

Filippov, B.P., Gopalswamy, N., Lozhechkin, A.V.: 2001, *Sol. Phys.* **203**, 119.

Fisher, R., Garcia, C.: 1984, *Astrophys. J. Lett.* **282**, L35.

Fisher, R.R., Poland, A.I.: 1981, *Astrophys. J.* **246**, 1004.

Fong, B., Low, B.C., Fan, Y.: 2002, *Astrophys. J.* **571**, 987.

Forbes, T.G.: 2000, *J. Geophys. Res.* **105**, 23153.

Forbes, T.G., Isenberg, P.A.: 1991, *Astrophys. J.* **373**, 294.

Forbes, T.G., Linker, J.A., Chen, J., Cid, C., Kóta, J., Lee, M.A., Mann, G., Mikić, Z., Potgieter, M.S., Schmidt, J.M., Siscoe, G.L., Vainio, R., Antiochos, S.K., Riley, P.: 2006, *Space Sci. Rev.* **123**, 251.

Fuller, N., Aboudarham, J., Bentley, R.D.: 2005, *Sol. Phys.* **227**, 61.

Gaizauskas, V.: 1998, In: D. F. Webb, B. Schmieder, & D. M. Rust (ed.) *IAU Colloq. 167: New Perspectives on Solar Prominences*, *Astronomical Society of the Pacific Conference Series* **150**, 257.

Gao, J., Wang, H., Zhou, M.: 2002, *Sol. Phys.* **205**, 93.

Gilbert, H.R., Alexander, D., Liu, R.: 2007, *Sol. Phys.* **245**, 287.

Gilbert, H.R., Holzer, T.E., Low, B.C., Burkepile, J.T.: 2001, *Astrophys. J.* **549**, 1221.

Gissot, S.F., Hochedez, J., Chainais, P., Antoine, J.: 2008, *Sol. Phys.* **252**, 397.

Gonzalez, R.C., Woods, R.E.: 2002, *Digital Image Processing.*

Gopalswamy, N., Hanaoka, Y., Hudson, H.S.: 2000a, *Adv. Space Res.* **25**, 1851.

Gopalswamy, N., Lara, A., Lepping, R.P., Kaiser, M.L., Berdichevsky, D., St. Cyr, O.C.: 2000b, *Geophys. Res. Lett.* **27**, 145.

Gopalswamy, N., Lara, A., Yashiro, S., Kaiser, M.L., Howard, R.A.: 2001, *J. Geophys. Res.* **106**, 29207.

Gopalswamy, N., Shimojo, M., Lu, W., Yashiro, S., Shibasaki, K., Howard, R.A.: 2003, *Astrophys. J.* **586**, 562.

Gopalswamy, N., Yashiro, S., Liu, Y., Michalek, G., Vourlidas, A., Kaiser, M.L., Howard, R.A.: 2005, *J. Geophys. Res.* **110**, A09S15.

Gopalswamy, N., Mäkelä, P., Xie, H., Akiyama, S., Yashiro, S.: 2009, *J. Geophys. Res.* **114**, A00A22.

Gosain, S., Schmieder, B.: 2010, *Ann. Geophys.* **28**, 149.

Gosling, J.T., Hildner, E., MacQueen, R.M., Munro, R.H., Poland, A.I., Ross, C.L.: 1974, *J. Geophys. Res.* **79**, 4581.

Gosling, J.T., Hildner, E., MacQueen, R.M., Munro, R.H., Poland, A.I., Ross, C.L.: 1976, *Sol. Phys.* **48**, 389.

Greisen, E.W., Calabretta, M.R.: 2002, *Astron. Astrophys.* **395**, 1061.

Handy, B.N., Acton, L.W., Kankelborg, C.C., Wolfson, C.J., Akin, D.J., Bruner, M.E., Caravalho, R., Catura, R.C., Chevalier, R., Duncan, D.W., Edwards, C.G., Feinstein, C.N., Freeland, S.L., Friedlaender, F.M., Hoffmann, C.H., Hurlburt, N.E., Jurcevich, B.K., Katz, N.L., Kelly, G.A., Lemen, J.R., Levay, M., Lindgren, R.W., Mathur, D.P., Meyer, S.B., Morrison, S.J., Morrison, M.D., Nightingale, R.W., Pope, T.P., Rehse, R.A., Schrijver, C.J., Shine, R.A., Shing, L., Strong, K.T., Tarbell, T.D., Title, A.M., Torgerson, D.D., Golub, L., Bookbinder, J.A., Caldwell, D., Cheimets, P.N., Davis, W.N., Deluca, E.E., McMullen, R.A., Warren, H.P., Amato, D., Fisher, R., Maldonado, H., Parkinson, C.: 1999, *Sol. Phys.* **187**, 229.

Hanisch, R.J., Farris, A., Greisen, E.W., Pence, W.D., Schlesinger, B.M., Teuben, P.J., Thompson, R.W., Warnock, A. III: 2001, *Astron. Astrophys.* **376**, 359.

Hansen, R.T., Garcia, C.J., Hansen, S.F., Yasukawa, E.: 1974, *Pub. Astron. Soc. Pac.* **86**, 500.

Hapgood, M.A.: 1992, *Planet. Space Sci.* **40**, 711.

Hildner, E.: 1974, *Sol. Phys.* **35**, 123.

Howard, R.A., Michels, D.J., Sheeley, N.R. Jr., Koomen, M.J.: 1982, *Astrophys. J. Lett.* **263**, L101.

Howard, R.A., Moses, J.D., Vourlidas, A., Newmark, J.S., Socker, D.G., Plunkett, S.P., Korendyke, C.M., Cook, J.W., Hurley, A., Davila, J.M., Thompson, W.T., St Cyr, O.C., Mentzell, E., Mehalick, K., Lemen, J.R., Wuelser, J.P., Duncan, D.W., Tarbell, T.D., Wolfson, C.J., Moore, A., Harrison, R.A., Waltham, N.R., Lang, J., Davis, C.J., Eyles, C.J., Mapson-Menard, H., Simnett, G.M., Halain, J.P., Defise, J.M., Mazy, E., Rochus, P., Mercier, R., Ravet, M.F., Delmotte, F., Auchere, F., Delaboudiniere, J.P., Bothmer, V., Deutsch, W., Wang, D., Rich, N., Cooper, S., Stephens, V., Maahs, G., Baugh, R., McMullin, D., Carter, T.: 2008, *Space Sci. Rev.* **136**, 67.

Hundhausen, A.J.: 1993, *J. Geophys. Res.* **98**, 13177.

Illing, R.M.E., Hundhausen, A.J.: 1985, *J. Geophys. Res.* **90**, 275.

Illing, R.M.E., Hundhausen, A.J.: 1986, *J. Geophys. Res.* **91**, 10951.

Inhester, B.: 2006, *ArXiv Astrophysics e-prints*.

Isenberg, P.A., Forbes, T.G., Demoulin, P.: 1993, *Astrophys. J.* **417**, 368.

Jackson, B.V., Froehling, H.R.: 1995, *Astron. Astrophys.* **299**, 885.

Jenkins, F.A., White, H.E.: 2001, *Fundamentals of Optics*.

Joshi, A.D., Srivastava, N.: 2011a, *Astrophys. J.* **730**, 104.

Joshi, A.D., Srivastava, N.: 2011b, *Astrophys. J.* **739**, 8.

Joshi, A.D., Mathew, S.K., Srivastava, N., Martin, S.F., Gupta, S.K.: 2010, *Indian J. Radio Space Phys.* **39**, 315.

Joshi, V., Srivastava, N.: 2007, *Bull. Astron. Soc. India* **35**, 447.

Kaiser, M.L., Kucera, T.A., Davila, J.M., St. Cyr, O.C., Guhathakurta, M., Christian, E.: 2008, *Space Sci. Rev.* **136**, 5.

Karpen, J.T., Antiochos, S.K., Mohensee, M., Klimchuk, J.A., MacNeice, P.J.: 2001, *Astrophys. J. Lett.* **553**, L85.

Keller, C.U., von der Luehe, O.: 1992, *Astron. Astrophys.* **261**, 321.

Kentischer, T.J., Schmidt, W., Sigwarth, M., Uexkuell, M.V.: 1998, *Astron. Astrophys.* **340**, 569.

Kilpua, E.K.J., Liewer, P.C., Farrugia, C., Luhmann, J.G., Möstl, C., Li, Y., Liu, Y., Lynch, B.J., Russell, C.T., Vourlidas, A., Acuna, M.H., Galvin, A.B., Larson, D., Sauvaud, J.A.: 2009, *Sol. Phys.* **254**, 325.

Kippenhahn, R., Schlüter, A.: 1957, *Zeitschrift für Astrophysik* **43**, 36.

Klimchuk, J.A.: 1990, *Astrophys. J.* **354**, 745.

Klimchuk, J.A.: 2001, *Space Weather (Geophysical Monograph 125), ed. P. Song, H. Singer, G. Siscoe (Washington: Am. Geophys. Un.), 143 (2001)* **125**, 143.

Koomen, M.J., Detwiler, C.R., Brueckner, G.E., Cooper, H.W., Tousey, R.: 1975, *Appl. Optics* **14**, 743.

Krall, J., Chen, J., Santoro, R.: 2000, *Astrophys. J.* **539**, 964.

Kuperus, M., Raadu, M.A.: 1974, *Astron. Astrophys.* **31**, 189.

Labeyrie, A.: 1970, *Astron. Astrophys.* **6**, 85.

Leroy, J.L.: 1979, In: E. Jensen, P. Maltby, & F. Q. Orrall (ed.) *IAU Colloq. 44: Physics of Solar Prominences*, 56.

Liewer, P.C., de Jong, E.M., Hall, J.R., Howard, R.A., Thompson, W.T., Culhane, J.L., Bone, L., van Driel-Gesztelyi, L.: 2009, *Sol. Phys.* **256**, 57.

Lin, C., Gallagher, P.T., Raftery, C.L.: 2010, *Astron. Astrophys.* **516**, A44.

Lin, Y.: 2005, Magnetic Field Topology Inferred from Studies of Fine Threads in Solar Filaments. PhD thesis, University of Oslo.

Lin, Y.: 2010, *Space Sci. Rev.*, 112.

Lin, Y., Engvold, O., Rouppe van der Voort, L., Wiik, J.E., Berger, T.E.: 2005, *Sol. Phys.* **226**, 239.

Lin, Y., Soler, R., Engvold, O., Ballester, J.L., Langangen, Ø., Oliver, R., Rouppe van der Voort, L.H.M.: 2009, *Astrophys. J.* **704**, 870.

Litvinenko, Y.E.: 1999, *Astrophys. J.* **515**, 435.

Litvinenko, Y.E.: 2000, *Sol. Phys.* **196**, 369.

Low, B.C.: 1981, *Astrophys. J.* **251**, 352.

Low, B.C.: 1996, *Sol. Phys.* **167**, 217.

Low, B.C.: 2001, *J. Geophys. Res.* **106**, 25141.

Low, B.C., Munro, R.H., Fisher, R.R.: 1982, *Astrophys. J.* **254**, 335.

Mackay, D.H., Karpen, J.T., Ballester, J.L., Schmieder, B., Aulanier, G.: 2010, *Space Sci. Rev.* **151**, 333.

MacQueen, R.M., Fisher, R.R.: 1983, *Sol. Phys.* **89**, 89.

MacQueen, R.M., Eddy, J.A., Gosling, J.T., Hildner, E., Munro, R.H., Newkirk, G.A. Jr., Poland, A.I., Ross, C.L.: 1974, *Astrophys. J. Lett.* **187**, L85.

Malherbe, J.M., Priest, E.R.: 1983, *Astron. Astrophys.* **123**, 80.

Malherbe, J.M., Priest, E.R., Forbes, T.G., Heyvaerts, J.: 1983, *Astron. Astrophys.* **127**, 153.

Maričić, D., Vršnak, B., Stanger, A.L., Veronig, A.: 2004, *Sol. Phys.* **225**, 337.

Maričić, D., Vršnak, B., Stanger, A.L., Veronig, A.M., Temmer, M., Roša, D.: 2007, *Sol. Phys.* **241**, 99.

Martin, S.F.: 1973, *Sol. Phys.* **31**, 3.

Martin, S.F.: 1998a, *Sol. Phys.* **182**, 107.

Martin, S.F.: 1998b, In: D. F. Webb, B. Schmieder, & D. M. Rust (ed.) *IAU Colloq. 167: New Perspectives on Solar Prominences*, *Astronomical Society of the Pacific Conference Series* **150**, 419.

Martin, S.F.: 2003, *Adv. Space Res.* **32**, 1883.

Martin, S.F., McAllister, A.H.: 1995, In: *AAS/Solar Physics Division Meeting #26*, *Bulletin of the American Astronomical Society* **27**, 961.

Martin, S.F., Panasenco, O.: 2010, *Mem. Soc. Astron. Italy* **81**, 662.

Martin, S.F., Bilimoria, R., Tracadas, P.W.: 1994, In: R. J. Rutten & C. J. Schrijver (ed.) *Solar Surface Magnetism*, 303.

Martin, S.F., Livi, S.H.B., Wang, J.: 1985, *Australian J. of Phys.* **38**, 929.

Martin, S.F., Panasenco, O., Engvold, O., Lin, Y.: 2008, *Ann. Geophys.* **26**, 3061.

Mathew, S.K.: 1998, A study of Solar Magnetic and Velocity Fields. PhD thesis.

Mathew, S.K., Gupta, S.K.: 2010, *PRL Technical Report* **2010-97**.

Mathew, S.K., Bhatnagar, A., Prasad, C.D., Ambastha, A.: 1998, *Astron. Astrophys. Suppl.* **133**, 285.

Mathew, S.K., Martínez Pillet, V., Solanki, S.K., Krivova, N.A.: 2007, *Astron. Astrophys.* **465**, 291.

McIntosh, P.S., Krieger, A.S., Nolte, J.T., Vaiana, G.: 1976, *Sol. Phys.* **49**, 57.

Menzel, D.H., Wolbach, J.G.: 1960, *Sky Tel.* **20**, 330.

Mierla, M., Davila, J., Thompson, W., Inhester, B., Srivastava, N., Kramar, M., St. Cyr, O.C., Stenborg, G., Howard, R.A.: 2008, *Sol. Phys.* **252**, 385.

Mierla, M., Inhester, B., Marqué, C., Rodriguez, L., Gissot, S., Zhukov, A.N., Berghmans, D., Davila, J.: 2009, *Sol. Phys.* **259**, 123.

Mierla, M., Inhester, B., Antunes, A., Boursier, Y., Byrne, J.P., Colaninno, R., Davila, J., de Koning, C.A., Gallagher, P.T., Gissot, S., Howard, R.A., Howard, T.A., Kramar, M., Lamy, P., Liewer, P.C., Maloney, S., Marqué, C., McAteer, R.T.J., Moran, T., Rodriguez, L., Srivastava, N., St. Cyr, O.C., Stenborg, G., Temmer, M., Thernisien, A., Vourlidas, A., West, M.J., Wood, B.E., Zhukov, A.N.: 2010, *Ann. Geophys.* **28**, 203.

Moon, Y., Choe, G.S., Wang, H., Park, Y.D., Gopalswamy, N., Yang, G., Yashiro, S.: 2002, *Astrophys. J.* **581**, 694.

Moore, R.L.: 1988, *Astrophys. J.* **324**, 1132.

Moran, T.G., Davila, J.M.: 2004, *Science* **305**, 66.

Munro, R.H., Gosling, J.T., Hildner, E., MacQueen, R.M., Poland, A.I., Ross, C.L.: 1979, *Sol. Phys.* **61**, 201.

Nakajima, H., Nishio, M., Enome, S., Shibasaki, K., Takano, T., Hanaoka, Y., Torii, C., Sekiguchi, H., Bushimata, T., Kawashima, S., Shinohara, N., Irimajiri, Y., Koshiishi, H., Kosugi, T., Shiomi, Y., Sawa, M., Kai, K.: 1994, *IEEE Proceedings* **82**, 705.

Neckel, H., Labs, D.: 1994, *Sol. Phys.* **153**, 91.

Netterfield, R.P., Freund, C.H., Seckold, J.A., Walsh, C.J.: 1997, *Appl. Optics* **36**, 4556.

Neupert, W.M., Thompson, B.J., Gurman, J.B., Plunkett, S.P.: 2001, *J. Geophys. Res.* **106**, 25215.

Panasenco, O., Martin, S.F.: 2008, In: R. Howe, R. W. Komm, K. S. Balasubramaniam, & G. J. D. Petrie (ed.) *Subsurface and Atmospheric Influences on Solar Activity*, *Astronomical Society of the Pacific Conference Series* **383**, 243.

Panasenco, O., Martin, S., Joshi, A.D., Srivastava, N.: 2011, *J. Atmos. Sol. Terr. Phys.* **73**, 1129.

Pesnell, W.D., Thompson, B.J., Chamberlin, P.C.: 2011, *Sol. Phys.* **10.1007/s11207-011-9841-3**.

Pierce, A.K., Slaughter, C.D.: 1977, *Sol. Phys.* **51**, 25.

Pizzo, V.J., Biesecker, D.A.: 2004, *Geophys. Res. Lett.* **31**, L21802.

Plunkett, S.P., Thompson, B.J., St. Cyr, O.C., Howard, R.A.: 2001, *J. Atmos. Sol. Terr. Phys.* **63**, 389.

Preminger, D.G., Walton, S.R., Chapman, G.A.: 2001, *Sol. Phys.* **202**, 53.

Priest, E.R.: 1988, *Astrophys. J.* **328**, 848.

Priest, E.R., Smith, E.A.: 1979, *Sol. Phys.* **64**, 267.

Qu, M., Shih, F.Y., Jing, J., Wang, H.: 2003, *Sol. Phys.* **217**, 157.

Qu, M., Shih, F.Y., Jing, J., Wang, H.: 2005, *Sol. Phys.* **228**, 119.

Raadu, M.A., Malherbe, J.M., Schmieder, B., Mein, P.: 1987, *Sol. Phys.* **109**, 59.

Robbrecht, E., Berghmans, D.: 2004, *Astron. Astrophys.* **425**, 1097.

Rust, D.M.: 1985, *Australian Journal of Physics* **38**, 781.

Rust, D.M., Kumar, A.: 1994, *Sol. Phys.* **155**, 69.

Rust, D.M., Martin, S.F.: 1994, In: K. S. Balasubramaniam & G. W. Simon (ed.) *Solar Active Region Evolution: Comparing Models with Observations*, *Astronomical Society of the Pacific Conference Series* **68**, 337.

Rutten, R.J., Bettonvil, F.C.M., Hammerschlag, R.H., Jägers, A.P.L., Leenaarts, J., Snik, F., Sütterlin, P., Tziotziou, K., de Wijn, A.G.: 2004, In: A. V. Stepanov, E. E. Benevolenskaya, & A. G. Kosovichev (ed.) *Multi-Wavelength Investigations of Solar Activity*, *IAU Symposium* **223**, 597.

Scharmer, G.B., Bjelksjo, K., Korhonen, T.K., Lindberg, B., Petterson, B.: 2003, In: S. L. Keil & S. V. Avakyan (ed.) *Society of Photo-Optical Instrumentation Engineers (SPIE) Conference Series* **4853**, 341.

Scherrer, P.H., Schou, J., Bush, R.I., Kosovichev, A.G., Bogart, R.S., Hoeksema, J.T., Liu, Y., Duvall, J.T.L., Zhao, J., Title, A.M., Schrijver, C.J., Tarbell, T.D., Tomczyk, S.: 2011, *Sol. Phys.* **10.1007/s11207-011-9834-2**.

Schmahl, E.J., Foukal, P.V., Noyes, R.W., Reeves, E.M., Timothy, J.G., Vernazza, J.E., Withbroe, G.L., Huber, M.C.E.: 1974, *Sol. Phys.* **39**, 337.

Schmieder, B., Raadu, M.A., Wiik, J.E.: 1991, *Astron. Astrophys.* **252**, 353.

Schrijver, C.J., Elmore, C., Kliem, B., Török, T., Title, A.M.: 2008, *Astrophys. J.* **674**, 586.

Seaton, D.B., Mierla, M., Berghmans, D., Zhukov, A.N., Dolla, L.: 2011, *Astrophys. J. Lett.* **727**, L10.

Shanmugaraju, A., Moon, Y., Dryer, M., Umapathy, S.: 2003, *Sol. Phys.* **215**, 185.

Sheeley, N.R. Jr., Howard, R.A., Koomen, M.J., Michels, D.J., Poland, A.I.: 1980, *Astrophys. J. Lett.* **238**, L161.

Sheeley, N.R., Walters, J.H., Wang, Y., Howard, R.A.: 1999, *J. Geophys. Res.* **104**, 24739.

Shih, F.Y., Kowalski, A.J.: 2003, *Sol. Phys.* **218**, 99.

Srivastava, N., Ambastha, A.: 1998, *Astrophys. Spa. Sci.* **262**, 29.

Srivastava, N., Venkatakrishnan, P.: 2002, *Geophys. Res. Lett.* **29**(9), 1287.

Srivastava, N., Venkatakrishnan, P.: 2004, *J. Geophys. Res.* **109**, 10103.

Srivastava, N., Ambastha, A., Bhatnagar, A.: 1991, *Sol. Phys.* **133**, 339.

Srivastava, N., Schwenn, R., Inhester, B., Stenborg, G., Podlipnik, B.: 1999, *Space Sci. Rev.* **87**, 303.

Srivastava, N., Schwenn, R., Inhester, B., Martin, S.F., Hanaoka, Y.: 2000, *Astrophys. J.* **534**, 468.

Srivastava, N., Inhester, B., Mierla, M., Podlipnik, B.: 2009, *Sol. Phys.* **259**, 213.

Sterling, A.C., Moore, R.L.: 2004a, *Astrophys. J.* **602**, 1024.

Sterling, A.C., Moore, R.L.: 2004b, *Astrophys. J.* **613**, 1221.

Sterling, A.C., Moore, R.L.: 2005, *Astrophys. J.* **630**, 1148.

Sütterlin, P., Rutten, R.J., Skomorovsky, V.I.: 2001b, *Astron. Astrophys.* **378**, 251.

Sütterlin, P., Hammerschlag, R.H., Bettonvil, F.C.M., Rutten, R.J., Skomorovsky, V.I., Domyshev, G.N.: 2001a, In: M. Sigwarth (ed.) *Advanced Solar Polarimetry – Theory, Observation, and Instrumentation*, *Astronomical Society of the Pacific Conference Series* **236**, 431.

Tandberg-Hanssen, E.: 1974, *Geophy. and Astrophys. Monographs* **12**.

Tandberg-Hanssen, E. (ed.): 1995, *The Nature of Solar Prominences*, *Astrophysics and Space Science Library* **199**.

Temmer, M., Veronig, A.M., Kontar, E.P., Krucker, S., Vršnak, B.: 2010, *Astrophys. J.* **712**, 1410.

Thernisien, A., Howard, R.A., Vourlidas, A.: 2006, *Astrophys. J.* **652**, 763.

Thernisien, A., Vourlidas, A., Howard, R.A.: 2009, *Sol. Phys.* **256**, 111.

Thompson, W.T.: 2006, *Astron. Astrophys.* **449**, 791.

Thompson, W.T.: 2009, *Icarus* **200**, 351.

Thompson, W.T.: 2010, *Astron. Astrophys.* **515**, A59.

Thompson, W.T., Davila, J.M., Fisher, R.R., Orwig, L.E., Mentzell, J.E., Hetherington, S.E., Derro, R.J., Federline, R.E., Clark, D.C., Chen, P.T.C., Tveekrem, J.L., Martino, A.J., Novello, J., Wesenberg, R.P., StCyr, O.C., Reginald, N.L., Howard, R.A., Mehalick, K.I., Hersh, M.J., Newman, M.D., Thomas, D.L., Card, G.L., Elmore, D.F.: 2003, In: S. L. Keil & S. V. Avakyan (ed.) *Society of Photo-Optical Instrumentation Engineers (SPIE) Conference Series* **4853**, 1.

Török, T., Kliem, B.: 2005, *Astrophys. J. Lett.* **630**, L97.

Tripathi, D., Isobe, H., Mason, H.E.: 2006, *Astron. Astrophys.* **453**, 1111.

Tripathi, D., Gibson, S.E., Qiu, J., Fletcher, L., Liu, R., Gilbert, H., Mason, H.E.: 2009, *Astron. Astrophys.* **498**, 295.

Valniček, B.: 1964, *Bull. Astron. Institutes Czechoslovakia* **15**, 207.

van Ballegooijen, A.A.: 2004, *Astrophys. J.* **612**, 519.

van Ballegooijen, A.A., Martens, P.C.H.: 1989, *Astrophys. J.* **343**, 971.

Vernazza, J.E., Avrett, E.H., Loeser, R.: 1981, *Astrophys. J. Sup. Ser.* **45**, 635.

Vial, J.C., Salm-Platzer, J., Martres, M.J.: 1981, *Sol. Phys.* **70**, 325.

von der Luehe, O.: 1993, *Astron. Astrophys.* **268**, 374.

Vršnak, B.: 2001a, *Sol. Phys.* **202**, 173.

Vršnak, B.: 2001b, *J. Geophys. Res.* **106**, 25249.

Vršnak, B., Gopalswamy, N.: 2002, *J. Geophys. Res.* **107**, 1019.

Vršnak, B., Ruzdjak, V., Rompolt, B.: 1991, *Sol. Phys.* **136**, 151.

Vršnak, B., Ruždjak, V., Brajša, R., Džubur, A.: 1988, *Sol. Phys.* **116**, 45.

Vršnak, B., Žic, T., Falkenberg, T.V., Möstl, C., Vennerstrom, S., Vrbanec, D.: 2010, *Astron. Astrophys.* **512**, A43.

Waldmeier, M.: 1970, *Sol. Phys.* **15**, 167.

Wang, H., Chae, J., Gurman, J.B., Kucera, T.A.: 1998, *Sol. Phys.* **183**, 91.

Webb, D.F., Krieger, A.S., Rust, D.M.: 1976, *Sol. Phys.* **48**, 159.

Weigelt, G., Wirnitzer, B.: 1983, *Optics Letters* **8**, 389.

Wells, D.C., Greisen, E.W., Harten, R.H.: 1981, *Astron. Astrophys. Suppl.* **44**, 363.

Wolfson, R., Saran, S.: 1998, *Astrophys. J.* **499**, 496.

Wu, S.T.: 1982, *Space Sci. Rev.* **32**, 115.

Wülser, J., Lemen, J.R., Tarbell, T.D., Wolfson, C.J., Cannon, J.C., Carpenter, B.A., Duncan, D.W., Gradwohl, G.S., Meyer, S.B., Moore, A.S., Navarro, R.L., Pearson, J.D., Rossi, G.R., Springer, L.A., Howard, R.A., Moses, J.D., Newmark, J.S., Delaboudiniere, J., Artzner, G.E., Auchere, F., Bougnet, M., Bouyries, P., Bridou, F., Clotaire, J., Colas, G., Delmotte, F., Jerome, A., Lamare, M., Mercier, R., Mullot, M., Ravet, M., Song, X., Bothmer, V., Deutsch, W.: 2004, In: S. Fineschi & M. A. Gummin (ed.) *Society of Photo-Optical Instrumentation Engineers (SPIE) Conference Series* **5171**, 111.

Yashiro, S., Gopalswamy, N., Michalek, G., St. Cyr, O.C., Plunkett, S.P., Rich, N.B., Howard, R.A.: 2004, *J. Geophys. Res.* **109**, 7105.

Zapior, M., Rudawy, P.: 2010, *Sol. Phys.* **267**, 95.

Zhang, J., Dere, K.P.: 2006, *Astrophys. J.* **649**, 1100.

Zhang, J., Dere, K.P., Howard, R.A., Kundu, M.R., White, S.M.: 2001, *Astrophys. J.* **559**, 452.

Zhang, J., Dere, K.P., Howard, R.A., Vourlidas, A.: 2004, *Astrophys. J.* **604**, 420.

Zharkova, V.V., Schetinin, V.: 2005, *Sol. Phys.* **228**, 137.

Zharkova, V.V., Ipson, S.S., Zharkov, S.I., Benkhalil, A., Aboudarham, J., Bentley, R.D.: 2003, *Sol. Phys.* **214**, 89.

Zirin, H.: 1988, *Astrophysics of the Sun.*

Zirin, H., Severny, A.: 1961, *The Observatory* **81**, 155.

Zirker, J.B.: 1989, *Sol. Phys.* **119**, 341.

Zirker, J.B., Engvold, O., Martin, S.F.: 1998, *Nature* **396**, 440.

List of Publications

I. Research Papers in Scientific Journals:

1. *Acceleration of Coronal Mass Ejections from Three-Dimensional Reconstruction of STEREO Images*, **Anand D. Joshi** and Nandita Srivastava, 2011a, *Astrophys. J.*, **739**, 8.

2. *Rolling Motion in Erupting Prominences Observed by STEREO*, Olga Panasenco, Sara F. Martin, **Anand D. Joshi** and Nandita Srivastava, 2011, *J. Atmos. Sol. Terr. Phys.*, **73**, 1129.

3. *Kinematics of Two Eruptive Prominences Observed by EUVI/STEREO*, **Anand D. Joshi** and Nandita Srivastava, 2011b, *Astrophys. J.*, **730**, 104.

4. *Automated Detection of Filaments and Their Disappearance Using Full-Disc Hα Images*, **Anand D. Joshi**, Nandita Srivastava and Shibu K. Mathew, 2010, *Sol. Phys.*, **262**, 425.

II. Papers in Proceedings:

1. *Acceleration of CMEs Associated with Eruptive Prominences*, **Anand D. Joshi** and Nandita Srivastava, 2010, *Space Sci. Proc.*, eds. S. S. Hasan and R. J. Rutten, 485

2. *A Dual Beam Hα Doppler System to Acquire, Analyse and Anticipate Solar Eruptive Events directed towards Earth*, **Anand D. Joshi**, Shibu K. Mathew, Nandita Srivastava, Sara F. Martin and Sudhir K. Gupta, 2010, *Indian J. Radio Space Phys.*, **39**, 315